Development and Validation of a Combustion Model for a Fuel Cell Off-Gas Burner

W. Tristan Collins

Magdalene College
University of Cambridge

A dissertation submitted to the University of Cambridge
for the degree of Doctor of Philosophy

June 2008

Development and Validation of a Combustion Model for a Fuel Cell Off-Gas Burner

W. Tristan Collins

A low-emissions power generator comprising a solid oxide fuel cell coupled to a gas turbine has been developed by Rolls-Royce Fuel Cell Systems. As part of the cycle, a fraction of the unreacted fuel (the off-gas) and oxidizer streams is reacted in a burner, which is the main source of pollutant formation. In this thesis a computational model of the burner has been developed which captures the formation of NO_x and the oxidation of CO. This model gives accurate predictions at low computational cost, making it suitable for use as a design tool in future burner design optimization through parametric studies.

A key factor in increasing computational efficiency was the development of a reduced H_2/CO/N_2 kinetic mechanism; from a starting mechanism of 30 species to 10 and 116 reactions to 6. The results of laminar opposed-flow diffusion flames have been used to validate the reduced mechanism.

Several different turbulent combustion models have been evaluated by creating an interface between the reduced kinetic mechanism and the commercial CFD solver FLUENT. Comparison of model predictions with well-characterized turbulent syngas flames, which share a similar fuel composition to the experimental work conducted on the off-gas burner, shows acceptable agreement. These studies have demonstrated the sensitivity of modelling constants. Improved predictions were achieved by calibrating these constants and including radiative heat losses.

Following suitable modification to reflect the predominantly laminar flow present in the current burner design, the relevant modelling approaches were applied to the off-gas burner. Comparison was made to previous detailed measurements, showing that the important trends of NO_x and CO are captured in general. The model was extended to high pressure conditions, similar to those in the actual off-gas burner, with the emissions predictions within design limits.

The outcome of this work is a fast, accurate design tool for CFD which has capabilities to simulate beyond the laminar burner studied here. It may be applied to more general types of off-gas/syngas burners where turbulence-chemistry interaction is expected to be more significant.

Declaration

This dissertation is the result of my own work and includes nothing which is the outcome of work done in collaboration except where specifically indicated in the text. It has not been submitted for another qualification to this or any other university. The full length of this thesis is approximately 30 000 words and includes 53 figures.

W. Tristan Collins
September 15, 2008

Acknowledgements

Contents

List of Figures

List of Tables

Nomenclature

The page number indicates the first mention of each symbol/acronym. All units are SI unless stated otherwise.

Roman Symbols

Greek Symbols

Superscripts

Subscripts

Acronyms

Chapter 1

Introduction

Meeting the need for efficient and environmentally clean power generation has never been so important. The increasing cost of fossil fuels and more stringent regulations on emissions (particularly CO_2 and NO_x), together with increasing demand for electricity, make the provision of cost-effective solutions highly desirable. Solid oxide fuel cells are one such option currently being explored due to the wide range of fuel compositions possible and high efficiencies available [59]. The main benefit of solid oxide fuel cells is the direct conversion of chemical energy in the fuel to electricity. A prototype commercial system developed by Rolls-Royce Fuel Cell Systems Limited (RRFCS), consisting of a combined solid oxide fuel cell and gas turbine (SOFC hybrid) cycle, has the goal of high cycle efficiency whilst having negligible NO_x and CO emissions. A key component of the cycle, with a critical impact on pollutant formation, is a burner designed to heat the oxidizer stream entering the fuel cell by using a fraction of the unreacted fuel and oxidizer leaving the fuel cell.

Experimental investigation has shown that a 'micro-mixing' burner design has the potential of fulfilling this goal of producing minimal emissions in the SOFC hybrid cycle. This burner uses a novel method of introducing the fuel and oxidizer which involves lay-

ering a number of thin fuel and oxidizer streams. A computational model of the burner could give insight into the complex flow and chemistry interactions with a view to predicting NO_x formation and furthering the design optimization beyond the experimental limits of cost, available facilities and time.

This thesis gives an overview of the SOFC hybrid cycle, a computational study of the SOFC hybrid off-gas burner, and a description of modelling methods used and their validation.

1.1 Motivation

A ground-based power generator is being developed by RRFCS which combines a solid oxide fuel cell into a gas turbine cycle. This stationary unit aims to generate 1 MW of electricity whilst satisfying rigorous environmental limits on pollutant emissions. It is intended to be suitable for use as a locally distributed energy supply in densely populated areas, such as such as city-centres or hospitals, or in enclosed spaces where dangerous emissions are to be avoided [50]. The generator is expected to fit in a standard shipping container-sized unit for ease of transport.

The SOFC hybrid cycle is shown schematically in Figure 1.1. The fuel used is reformed natural gas, produced by reacting natural gas (CH_4, C_2H_6, or C_3H_8) with high temperature (≈ 1100 K) steam in the presence of a catalyst, forming H_2, CO and CO_2. As part of the cycle, the reformed natural gas is reacted in a fuel cell, with 15–25% remaining unreacted. The mixture of products and unreacted reformed natural gas is very lean, and at high temperature and pressure. This mixture is known as 'off-gas' or tail-gas, and shares a similar composition to 'syngas' (synthesis gas). It is then passed to a burner to complete the reaction and provide pre-heat to the cathode gas entering the fuel cell. A turbine, driving a compressor used to pressurize the incoming air, is
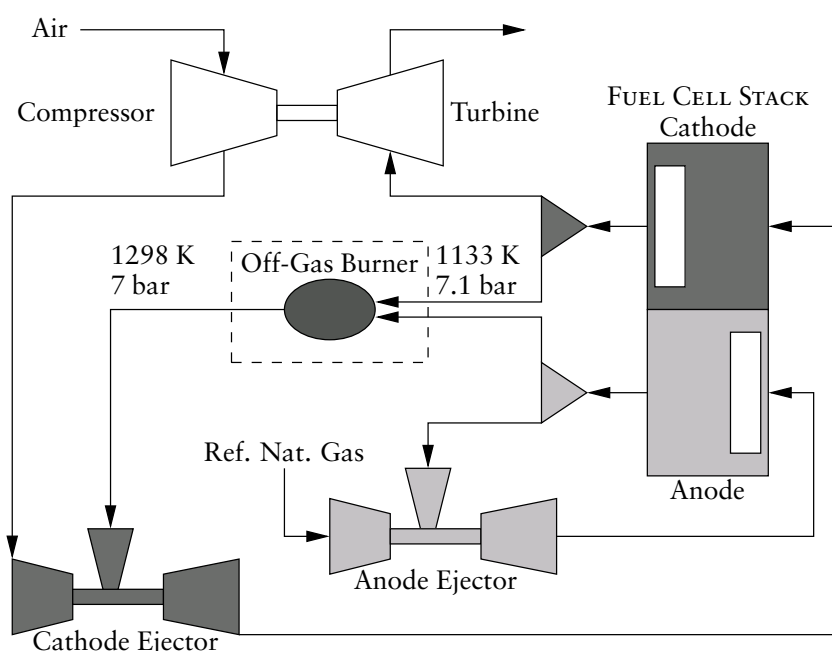
Figure 1.1: SOFC hybrid cycle schematic [50].

powered by a fraction of the reacted gas (oxidizer) from the fuel cell. The anode and cathode ejectors act as pumps for the cycle. Due to the nature of the SOFC hybrid cycle the conditions at the burner inlet are set by the fuel cell. This poses a number of challenges to burner design, which is governed by the following main requirements and constraints:

1. stable operation at design conditions,

2. negligible NO_x (< 5 ppm) and CO (< 50 ppm) production,

3. minimum pressure loss across the burner, and

4. zero total pressure difference between fuel and oxidizer.

These requirements are technical challenges, and some compete with each other; they present a design challenge as they are highly inter-related with respect to burner performance. For instance, NO_x formation is reduced by good mixing of the streams. However, a zero pressure differential between streams is not conducive to good mixing.

A pressure loss reduces the cycle efficiency.

1.2 Objectives

The overall objective of the project is to focus on one component of the cycle; to develop an understanding of the complex mixing processes involved in the operation of the burner, the chemical reactions taking place, and the interactions between the turbulence and the chemistry. A detailed computational model of the system could give information on the combustion processes and pollutant formation for comparison with the available atmospheric experimental data and give valuable information on operational conditions not easily replicated by laboratory experiments. The detailed model can be used to optimize the burner design by simulating more configurations and conditions than possible experimentally and economically.

The objectives of the present work are to develop, validate and apply a modelling approach for the off-gas burner to determine NO_x and CO emission levels. Following correct validation, the use of computational fluid dynamics (CFD) and simplified kinetics will yield an accurate and fast design tool which can be used for further burner design optimization. The computational results will provide a reference for experimental work, as well as for more advanced computational modelling developed in any future work. The focus is on reactions that take place under atmospheric conditions, for which the experimental data is currently available. The model can then be extended for use at the higher operating pressures of the burner.

1.3   Thesis Overview

The current chapter gives an outline of the project motivations and objectives. In Chapter 2 background information on syngas fuel and the slotted burner design is given. In Chapter 3 a review of the governing equations and closure methods for turbulent reacting flows used in this thesis is presented. Chapters 4–5 follow the logical steps for developing a turbulent combustion model for the off-gas burner. These are:

(i) Laminar chemistry validation. Details of the formation of a reduced kinetic mechanism and its validation for laminar diffusion flames are given in Chapter 4.

(ii) Comparison of turbulence-chemistry interaction models and turbulence closures for experimentally well characterized turbulent flames [4, 28]. In Chapter 5 the commercial CFD package FLUENT [39] is used with the reduced mechanism implemented.

In light of the findings of Grimwood [50] for the off-gas burner, indicating laminar flow in the near-field, Chapter 6 takes the relevant parts of the model (i.e. the chemical mechanism) and applies laminar finite-rate chemistry (ignoring turbulent fluctuations of temperature and species concentrations) to give an easily implemented design tool. This is applied to the off-gas burner at (i) atmospheric, (ii) high pressure and low temperature, (iii) high temperature and low pressure, and (iv) high temperature and pressure conditions in Chapter 6. Finally, the findings are summarized in Chapter 7 along with suggestions for future work.

Chapter 2

Background

In this chapter a background to the physical features of the SOFC hybrid off-gas burner, and their implications for modelling, is presented. Two key aspects of the system, the slotted burner configuration and the fuel composition, are discussed with reference to previous work. An overview of the modelling methodology used in later chapters is presented in the last section.

2.1   Effect of Temperature on Emissions

The main source of NO_x in combustion problems is the oxidation of atmospheric nitrogen present in the mixture via the Zel'dovich (thermal) mechanism (discussed later in Section 3.3). NO_x forms mainly in the post-flame gases (thermal NO_x) where high temperatures exist, although a small amount may be produced in the flame front (prompt NO_x). The oxidation of CO to CO_2 is a slow process even at high temperatures [66]. There is a design trade-off between: (i) high temperatures, and therefore high NO_x and low CO; and (ii) low temperatures, with low NO_x but the possibility of higher CO emissions.
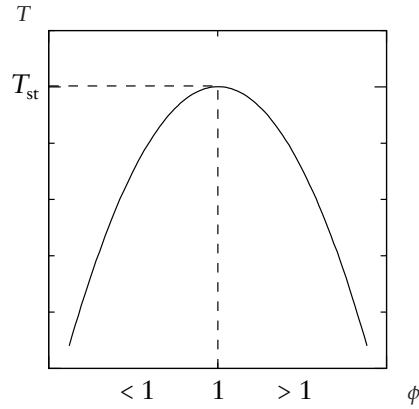
Figure 2.1: Variation of temperature, T, with equivalence ratio, ϕ [44].

Ideally, the fuel and oxidizer streams coming from the fuel cell (Figure 1.1) would be fully premixed before combustion takes place. Lean premixed reactants would burn at a lower temperature than an equivalent non-premixed flame [44]. This is because the reaction in a non-premixed flame takes place at the stoichiometric (equivalence ratio, ϕ, of unity) iso-surface, at the corresponding stoichiometric temperature, T_{st}, as shown schematically in Figure 2.1. In a lean premixed flame the temperature is lower than the stoichiometric temperature due to the presence of excess oxidizer that acts as a diluent and reduces the overall temperature as seen by the shape of the curve in Figure 2.1. A similar drop in temperature also occurs for rich mixtures ($\phi > 1$) where there is insufficient oxidizer to burn all the fuel present thus reducing the energy released. Clearly, premixing is the preferred choice to control temperatures. However, this is not possible in the SOFC hybrid cycle because of the onset of auto-ignition at the high pressures and temperatures involved.

In a very lean, dilute, non-premixed situation, such as in the SOFC hybrid cycle, the temperature difference between T_{st} and the adiabatic flame temperature can be considerable due to the large proportion of diluent. The temperatures at the flame front can be reduced by dilution of the post-flame gases with unreacted, cooler gas. As NO_x

production is highly temperature dependent it is beneficial to ensure that the maximum temperature is kept as low as possible and the high temperature region is kept small. By ensuring sufficient mixing of the fuel and oxidizer streams, the NO_x production can be reduced.

There are four main timescales in the off-gas burner: (i) mixing, τ_{mix}; (ii) NO_x formation, τ_{NO}; (iii) CO oxidation, τ_{CO}; and (iv) H_2 oxidation, τ_{H_2}. At the representative temperatures present in the off-gas burner, the chemical timescales can be arranged in order of magnitude as $\tau_{NO} > \tau_{CO} > \tau_{H_2}$. The mixing timescale can be controlled via the burner design and operational parameters such as bulk velocity. As τ_{NO} is larger than the other processes, the NO_x formation processes may be decoupled from the fast H_2 reactions resulting in a simplification of NO_x kinetics, as will be discussed in Section 3.3. The CO timescale is sensitive to local mixture composition and temperature, both of which are influenced by τ_{mix}, resulting in a design trade-off as discussed above. The problem is how to produce sufficient mixing to decrease τ_{mix} and reduce NO_x emissions whilst ensuring CO has enough time in the high temperature regions to fully oxidize. These mixing issues are discussed below.

2.2 Slotted Burners

In conventional burners a pressure difference between the fuel and oxidizer streams is used to promote mixing. For example, the use of swirl helps in producing a short flame, improves the homogenization of the mixture and the stability of the flame [40]. This helps to control the combustion process and minimize pollutant formation, such as NO_x, as the temperature is kept lower. However, in the SOFC hybrid cycle no such pressure difference exists as both oxidizer and fuel emerge from the same fuel cell. The option of introducing a pressure loss across the burner is unavailable due to design con-
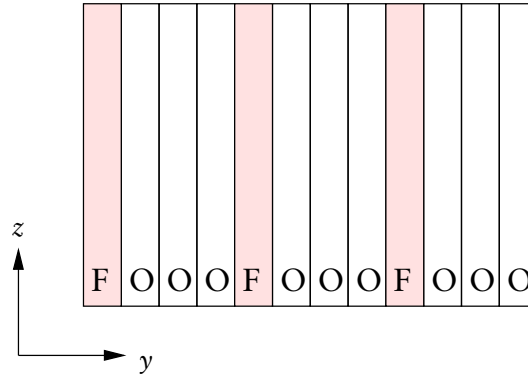
Figure 2.2: Schematic showing a possible configuration of the 'layering' of fuel (F) and oxidizer (O) streams.

straints. A novel design of burner is required to achieve sufficient mixing whilst keeping the pressure loss to a minimum. Previous investigation and experiments at atmospheric conditions have indicated that a 'micro-mixing' burner can satisfy the requirements of the off-gas burner by generating many local shear layers [50].

The micro-mixing burner comprises a series of thin (of the order of 1 mm and aspect ratio 66), layered fuel and oxidizer streams, as shown schematically in Figure 2.2. Within each layer, or 'slot', corrugations angle the flow so that adjacent streams can have differing flow directions in the x–z plane, shown in Figure 2.3. The currently available angles, shown as θ in Figure 2.3, are 0°, 15° and 30°. Each 'unit' comprises a fuel stream adjacent to a number of oxidizer streams. Such a unit, shown schematically in Figure 2.4, is combined together with other units to form the complete 'slotted' burner. The overall make-up of the burner can be altered radically by combining different ratios of fuel to oxidizer streams within each unit, varying the flow angle and using a different number of units. A complete burner is shown in Figure 2.5 with a single unit highlighted.

The slotted burner design results in a number of individual diffusion flames, as shown in Figure 2.6a. The flow through the slots is likely to be laminar: at atmospheric op-
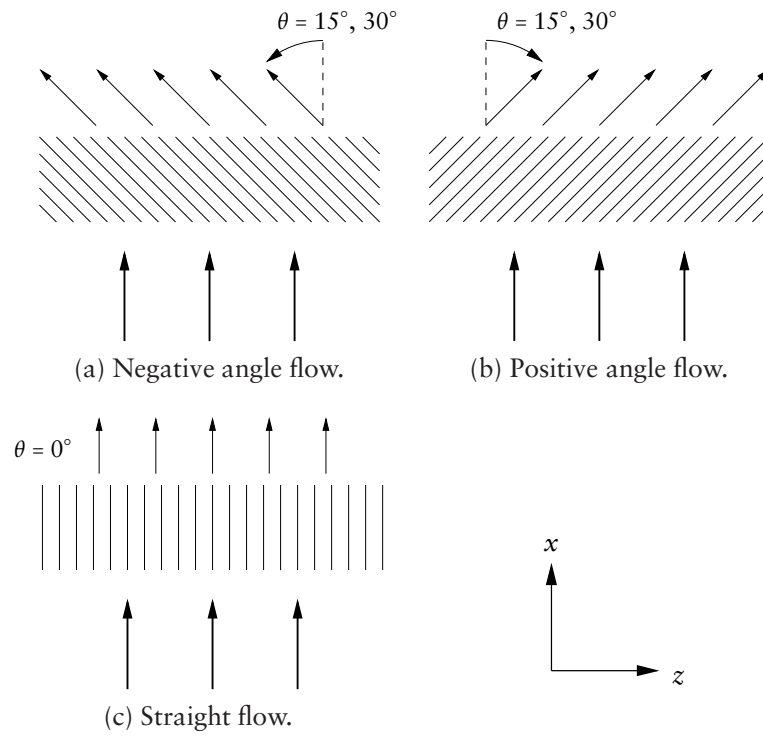
Figure 2.3: Schematics showing varying flow angles possible within each fuel or oxidizer layer due to corrugations placed within each slot.
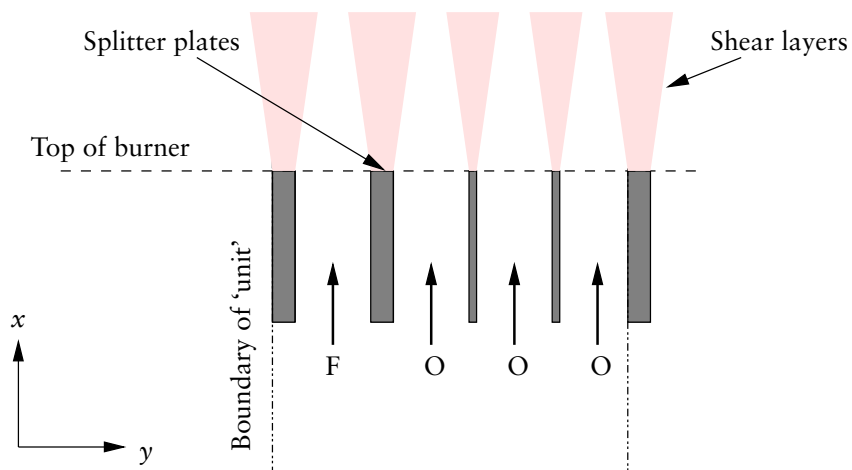
Figure 2.4: Schematic showing a possible individual 'unit' of fuel (F) and oxidizer (O) streams and expected shear layer regions.
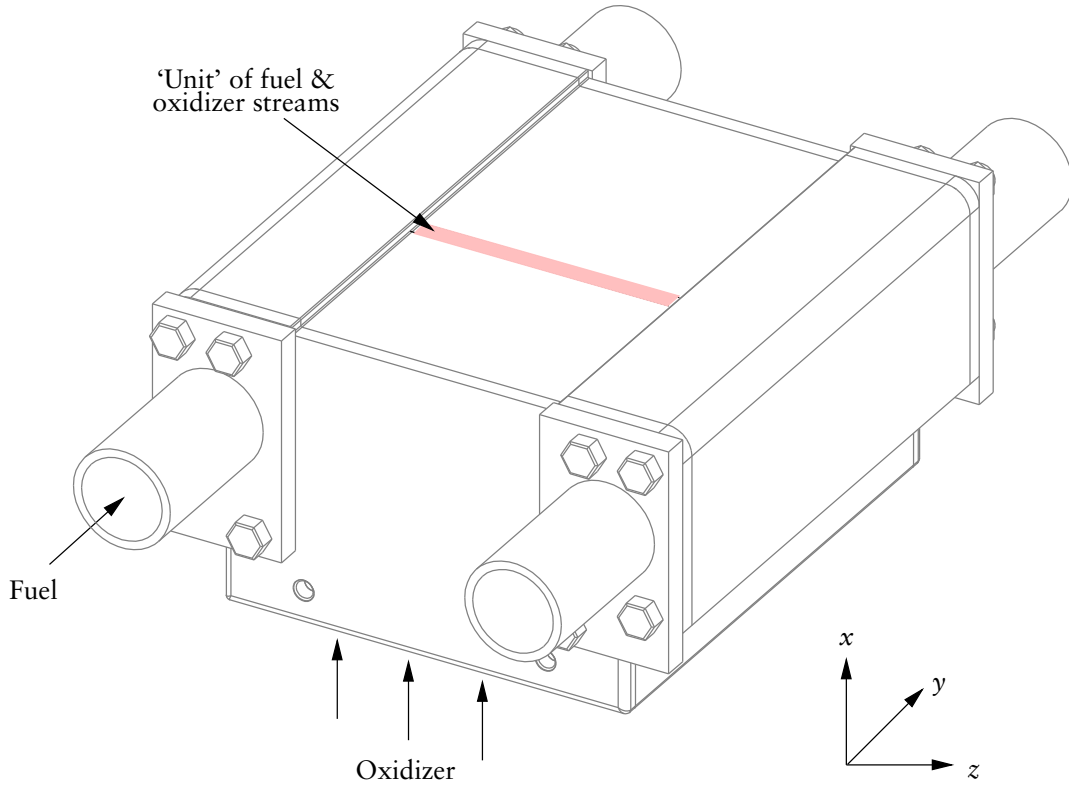
Figure 2.5: Drawing of the complete burner. An individual unit, shown schematically in Figure 2.4, is highlighted. Also shown is the method of manifolding the fuel and oxidizer [50].

erating conditions the Reynolds number, based on the hydraulic diameter of a slot, Re, is ≈ 500 which is less than the transition value of Re = 1400 for stationary parallel plates [50, 82]. Likewise, the conditions present in the actual SOFC hybrid cycle give Re ≈ 1070, again less than the transition value [50]. It is intended that the large number of thin streams and varying flow angles will increase the mixing due to the number of shear layers generated downstream of the splitter plates, indicated in Figure 2.4. A method of generating shear would be by varying the axial velocity between the fuel and oxidizing streams, but this is not desirable due to the pressure loss incurred. Instead, it is thought that shear layers formed via a difference in flow angle will generate turbulence, and hence promote mixing, whilst helping with flame stabilization and reducing NO_x

(a) Side view

(b) End view

Figure 2.6: Photographs of the off-gas burner in operation during atmospheric experimental tests [50]. The gas sampling probe and thermocouple can be seen.

emissions [1, 50]. This increased mixing would be advantageous in reducing peak temperature 'hot spots' and regions of high temperature gradients where NO_x is expected to form, as discussed above in Section 2.1. In addition, the conversion of CO_2 back to CO further downstream would be prevented as the reaction would be quenched due to the decrease in temperature.

2.2.1 Previous Work

The availability of experimental studies on arrays of slotted flows is limited. The number of numerical studies of these configurations is also limited. However, there are a number of studies on single or triple slot flows. A discussion of some pertinent studies is given below.

Al-Shaikhly et al. [1] investigated NO_x emissions using shear layer turbulent diffusion flames. They found this method resulted in 'ultralow' levels of NO_x for propane/natural gas/air flames at atmospheric conditions, comparable to equivalent premixed sys-

tems [1]. Another advantage found was increased flame stability. Baker et al. [2] studied laminar 'micro-slot' diffusion propane/air flames under atmospheric conditions. Single rectangular slots of width < 1 mm were used to investigate flame heights by comparison with a theoretical model. They found that the flames were not necessarily diffusion-controlled and that buoyancy had a non-negligible effect in certain regions [2]. However, this suggests that accurate representation of diffusive transport in any numerical model is important. This has implications for the modelling procedures used in Chapter 3.

Nicoli et al. [86] studied a three-plan system of alternating oxygen and hydrogen jets at low Reynolds numbers, viewed as a two-dimensional version of a coaxial injector. Direct Numerical Simulations (DNS) were performed using simplified global finite-rate chemistry. The combustion in the mixing layers formed was found to dampen the shear layer instabilities usually found in cold flow systems. In the present work simpler flow modelling will be used along with more detailed kinetics. This will provide a faster, but still accurate, design tool for burner optimization.

The experimental work on the off-gas burner was predominantly conducted at atmospheric pressures due to the experimental difficulties of working at high pressures [50]. A set of boundary conditions at atmospheric pressure were investigated. These are given in Appendix C.1. The boundary conditions were divided into atmospheric temperature inlets (denoted ATP) and high temperature inlets (denoted HT). These boundary conditions are used in numerical simulations of the off-gas burner, and comparisons with experiment are made for NO_x and CO results, as discussed in Chapter 6.

2.3   Off-Gas

Accurate representation of the kinetics, via an appropriate mechanism, is paramount in capturing the underlying physics of a $H_2/CO/N_2$ flame. The off-gas burner reacts a

dilute, lean mixture of hydrogen, carbon monoxide and nitrogen (referred to as off-gas or syngas) with oxygen at high temperature and pressure. For atmospheric conditions this can be represented as

$$a\text{H}_2 + b\text{CO} + c\text{N}_2 + \frac{\nu}{\phi}(\text{O}_2 + \alpha\text{N}_2) \longrightarrow$$
$$d\text{H}_2\text{O} + e\text{CO}_2 + f\text{N}_2 + \nu\left(\frac{1}{\phi} - 1\right)(\text{O}_2 + \alpha\text{N}_2),$$
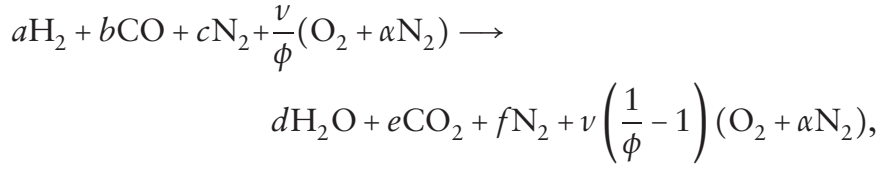
which is discussed further in Appendix C.2. A full reaction mechanism for H_2/CO flames may contain over 50 reactions depending on the kinetic detail included [23]. In general, the greater the number of reaction steps, the greater the number of species appearing in the mechanism. A simplified mechanism for illustrative purposes is given by [113];

$$\text{CO} + \text{OH} \rightleftharpoons \text{CO}_2 + \text{H}, \tag{CO1}$$

$$\text{H} + \text{O}_2 \rightleftharpoons \text{OH} + \text{O}, \tag{CO2}$$

$$\text{O} + \text{H}_2 \rightleftharpoons \text{OH} + \text{O}, \tag{CO3}$$

$$\text{OH} + \text{H}_2 \rightleftharpoons \text{H}_2\text{O} + \text{H}. \tag{CO4}$$

In the flame front the hydrogen reacts very quickly with the oxygen, due to its fast chemistry and high diffusion coefficient, producing H and OH radicals that proceed in chain-propagating reactions involving, amongst other species, carbon monoxide. Carbon monoxide reacts more slowly than the hydrogen and generally reacts with OH radicals to be oxidized to carbon dioxide, Reaction (CO1). The CO oxidation step, Reaction (CO1), is also a chain-propagating step producing H atoms that go on to react with O_2, forming OH and O, in Reaction (CO2), a chain-branching reaction. This supplies the radicals for the CO oxidation step, the reaction of H_2, Reactions (CO3) and (CO4),

and the reaction with the nitrogen present. The presence of CO reduces the speed of the overall reaction. When nitrogen chemistry is added, the number of reactions and species can greatly increase. The development and validation of an appropriate reduced mechanism is discussed in Chapter 4.

2.3.1 Previous Work

There has been renewed interest in syngas as a fuel for gas turbines operating at high pressures [17, 18, 30, 36, 59, 69, 85, 110, 117]. Much of this work is focused on developing detailed kinetic mechanisms over a wide range of conditions. Reduced mechanisms for H_2/CO flames have been developed based on reduced mechanisms for methane flames [23, 24, 102]. However, many of the recent updates to H_2/CO kinetics [30, 56, 106] are not included in these mechanisms. In addition, nitrogen chemistry is often excluded from the reduced mechanisms and requires post-processing, as discussed in Section 3.3.

Previous work has shown that NO_x formation is highly influenced by physical and chemical phenomena such as mixing processes and interlinked chemical reactions [113]. Information on the mechanisms of NO_x formation is difficult to obtain experimentally so an accurate computational model giving such information would be highly advantageous. Much work has been carried out on the post-processing of thermal NO_x from a combustion and flow solution. A selection of publications that used a computational post-processing method for NO_x and the related assumptions are discussed below.

Lee et al. [67] compared their computational model to experimental data for a simple coaxial-flow jet flame of a CH_4 and air mixture, concentrating on NO_x emissions. They conducted parametric tests varying the fuel flow-rate and equivalence ratio of the CH_4-air mixture. The experiment featured a high velocity gradient across the fuel

and air streams. The numerical model calculated the NO_x reaction rate using CHEM-KIN [57]. They found thermal NO_x increasing with equivalence ratio of the fuel stream until $\phi = 1.5$, then as the system tends to being a non-premixed flame the NO_x production decreases. The thermal NO_x formation was highly dependent on both the temperature and the size of the temperature region above 1850 K. It is in this region where there is likely to be a high concentration of OH radicals which react with nitrogen to form NO_x.

Jiménez et al. [54] modelled lean C_4H_{10}-air flames and tested the NO_x production modelling assumptions of equilibrium and steady-state hypothesis. These assumptions permit post-processing of NO_x from local N_2 and O_2 concentrations, and temperatures. Numerical simulations were conducted using CHEMKIN for the elementary reaction production terms and multi-component molecular transport coefficients. They find that the steady-state and partial equilibrium assumptions are inaccurate when compared to DNS results (under-predicting the production rate by 75%) and conclude that the partial equilibrium assumption for O and O_2 is not a good one. They suggest that accurate NO_x prediction requires explicit computation of the concentration of O atoms, but computation using full NO_x chemistry is not required. However, as comparison was made to DNS with a very small computational domain, only very early post-flame NO production was captured. They also evaluated other modelling approaches such as the Steady Laminar Flamelet Model (SLFM) and Conditional Moment Closure (CMC). They find that NO production is best modelled using the CMC approach. However, the computational requirements for CMC are large when compared to simpler approaches such as the SLFM.

İlbas et al. [52] compared a numerical simulation of a non-premixed H_2 diffusion flame in a co-axial burner to experiment. The overall equivalence ratio was set to unity. They used the commercial CFD code FLUENT to obtain a flow and reaction solution,

then used a NO_x post-processor to predict emissions from the burner. The reaction rate was calculated using both Arrhenius rates and the Eddy-Dissipation Model (EDM). A single-step reaction mechanism for hydrogen was used. They found good agreement between the computational model and experiment for most cases, and that thermal NO_x is the most important NO_x mechanism in hydrogen combustion. Diluting the products using air staging of 25% reduced the average temperature and NO_x concentration.

An extension of the post-processing method used by İlbas et al. was investigated by Frassoldati et al. [40] for swirling confined flames. They used FLUENT to solve for the temperature and flow field, and post-process for NO_x. Their approach was to lump together computational cells with similar NO_x formation characteristics, such as temperature and availability of O_2. These 'macrocells' are assumed to be a network of ideal reactors and are simulated using very detailed reaction kinetics. They found good correlation with experimental results once model constants were adjusted. Their results for NO_x obtained with this ideal-reactor method were found to be better than those obtained using partial-equilibrium and steady-state assumptions, and were very close to experiment.

A comparison of NO_x predictions using three different combustion models and the partial-equilibrium (of O and OH) post-processing approach was made by Jiang and Campbell [53]. They found the temperature profiles were fairly well captured by the EDM and that the use of extended Zel'dovich mechanism for NO_x production had negligible effects on NO_x levels compared to the standard mechanism. Their study suggested that post-processing can give a valuable insight into NO_x formation so long as the velocity and temperature fields are adequately predicted.

The studies mentioned above suggest that combining an accurate H_2/CO kinetic mechanism with either (i) full nitrogen chemistry or (ii) a NO_x post-processing step can provide useful information on NO_x and CO emissions trends. There is an emphasis

on the importance of explicitly calculating certain intermediate species in any computational model, as discussed in Section 3.3. In addition, the correct temperature field prediction is of paramount importance to NO_x predictions. However, the use of detailed kinetics (with or without nitrogen chemistry) implies that a large number of species, and hence scalars, need to be included in any computational model. This is a disadvantage as it increases the computational requirements to run each simulation. The methods used in this thesis for reducing these computational requirements, yet retaining physical accuracy, are discussed next.

2.4 Methodology

To be able to perform parametric studies on the off-gas burner it is advantageous to reduce the computation time and memory requirements of the simulations. These reductions can made in three areas: (i) simplified kinetics, (ii) simplified model closures, and (iii) geometric simplifications. In this thesis, all three are adopted to give a fast, accurate design tool. A reduced kinetic mechanism is developed in Chapter 4 and validated for laminar H_2/CO/N_2 diffusion flames. This mechanism is then tested against two well-characterized turbulent syngas flames (a bluff-body stabilized and jet flame) in Chapter 5, providing a more stringent test of the predictive capabilities of the mechanism and the underlying closure models described in Chapter 3. The test flames, discussed in Chapter 5, feature areas of high shear where mixing via turbulent transport is predominant. In Chapter 6 the modelling strategy is applied to the off-gas burner. This model is extended to high pressure conditions, and also to the high temperature and pressure conditions found in the actual off-gas burner.

Chapter 3

Modelling Approach

The study of turbulent reacting flows starts with the basic equations of fluid flow; the Navier-Stokes equations [64, 96]. These equations are Reynolds-averaged for constant density flows, and known as Reynolds-averaged Navier-Stokes (RANS) equations. The extension to non-constant density flows, the Favre-averaged form of these equations, is presented below, along with a discussion of the closure methods used for turbulence and chemistry.

3.1   Turbulence Closure

In reacting flows large changes in density occur due to the heat release of the reaction. In turbulent flows additional terms appear due to the correlation of scalar and density fluctuations. Favre averaging is used to reduce the number of unknown correlations [7]. Following Kuo [64] and Poinsot and Veynante [96] the Favre-averaged forms of the balance equations are used in this study [39]. The Favre-averaged (or density-weighted) form of a general scalar ϕ is defined as $\tilde{\phi} = \overline{\rho\phi}/\bar{\rho}$, where ρ is the density and the over-bar indicates a Reynolds-averaged quantity. The instantaneous value of a general scalar

is decomposed into the Favre-averaged value and its fluctuation by $\phi = \tilde{\phi} + \phi''$. The equation for mass continuity is given by

$$\frac{\partial \bar{\rho}}{\partial t} + \frac{\partial}{\partial x_i}(\bar{\rho}\tilde{u}_i) = 0, \tag{3.1}$$

where u_i is the velocity component in the i direction. The balance equation for momentum is given by

$$\frac{\partial}{\partial t}(\bar{\rho}\tilde{u}_i) + \frac{\partial}{\partial x_j}(\bar{\rho}\tilde{u}_i\tilde{u}_j) = -\frac{\partial \bar{p}}{\partial x_i} + \frac{\partial \bar{\tau}_{ij}}{\partial x_j} - \frac{\partial}{\partial x_j}\left(\bar{\rho}\widetilde{u_i'' u_j''}\right), \tag{3.2}$$

where $\bar{p}$ is the average pressure. In Equation (3.2) the two terms on the left hand side (LHS) represent the local rate of change and convection of momentum, respectively. The terms on the right hand side (RHS) represent the pressure gradient, molecular transport due to viscous shear stress and the Reynolds stress tensor, respectively. The viscous stress tensor, $\bar{\tau}_{ij}$, is given by

$$\bar{\tau}_{ij} = \mu \left[2\tilde{S}_{ij} - \frac{2}{3}\frac{\partial \tilde{u}_k}{\partial x_k}\delta_{ij} \right], \tag{3.3}$$

where μ is the molecular viscosity calculated using kinetic theory (Appendix A.1) [11], δ_{ij} is the Kronecker delta ($\delta_{ij} = 1$ for $i = j$ and $\delta_{ij} = 0$ for $i \neq j$), and the strain tensor, $\tilde{S}_{ij}$, is given by

$$\tilde{S}_{ij} = \frac{1}{2}\left(\frac{\partial \tilde{u}_i}{\partial x_j} + \frac{\partial \tilde{u}_j}{\partial x_i} \right). \tag{3.4}$$

The final term of Equation (3.2), $\bar{\rho}\widetilde{u_i'' u_j''}$, is known as the Reynolds stress tensor. The aim of turbulence modelling is to provide closure for this term whilst retaining the relevant physics. There are a number of models in widespread use. The most common approach

involves the Boussinesq hypothesis which assumes the Reynolds stress is proportional to the mean rate of strain [96],

$$-\bar{\rho}\widetilde{u_i''u_j''} + \frac{2}{3}\bar{\rho}\tilde{k}\delta_{ij} = \mu_t(2\tilde{S}_{ij}) - \frac{2}{3}\mu_t\frac{\partial\tilde{u}_k}{\partial x_k}\delta_{ij}, \tag{3.5}$$

where $\tilde{k}$ is the turbulent kinetic energy, given by $\tilde{k} = \frac{1}{2}\widetilde{u_i''u_i''}$. Equation (3.5) is analogous to Equation (3.3) with the introduction of the turbulent viscosity, μ_t [96, 97]. Implicit within the Boussinesq hypothesis is the assumption of isotropic turbulence, which is the case at small scales, but not at large scales where average quantities are defined [89]. The second term on the LHS of Equation (3.5) is usually absorbed in the pressure term of Equation (3.2) as $(\partial/\partial x_i)(\bar{p} + 2\bar{\rho}\tilde{k}/3)$. This approach replaces the unknown Reynolds stresses with an unknown turbulent viscosity which itself requires modelling.

Another approach involves solving the six components of the Reynolds stresses directly, with appropriate modelling of the unclosed terms in these equations. This does not involve the assumption of isotropy, thus giving improved predictions in complex flows such as asymmetric channels and curved flows. However, this approach results in an increase in the computational effort required.

In summary, to provide closure to Equation (3.2) either the turbulent viscosity needs to be evaluated or the individual Reynolds stresses need to be solved for. Both these approaches will be tested and compared in Chapter 5. The first approach involves two equations for the turbulent kinetic energy, $\tilde{k}$, and its dissipation rate, $\tilde{\varepsilon}$, which will be discussed next.

3.1.1   Standard k-ε Closure

The standard k-ε model is the most widely used turbulence closure [97]. The form of the isotropic turbulent viscosity equation used is estimated as

$$\mu_t = \bar{\rho} C_\mu \frac{\tilde{k}^2}{\tilde{\varepsilon}}, \tag{3.6}$$

where $\tilde{\varepsilon}$ is the dissipation rate of turbulent kinetic energy, $\tilde{k}$. In this model, the value of C_μ is taken as a constant value of 0.09, based on experimental and DNS data of the inertial sub-layers of channel and boundary layer flows [105]. The appearance of $\tilde{k}$ and $\tilde{\varepsilon}$ requires a model equation for each.

The standard equation for the turbulent kinetic energy is [97]

$$\frac{\partial}{\partial t}(\bar{\rho}\tilde{k}) + \frac{\partial}{\partial x_i}(\bar{\rho}\tilde{k}\tilde{u}_i) = \frac{\partial}{\partial x_i}\left[\left(\mu + \frac{\mu_t}{\sigma_k}\right)\frac{\partial \tilde{k}}{\partial x_i}\right] + P_k - \bar{\rho}\tilde{\varepsilon}, \tag{3.7}$$

where σ_k is the turbulent Prandtl number for kinetic energy. The terms of the LHS represent the local rate of change and convection, respectively. The first term on the RHS represents the turbulent transport of $\tilde{k}$. The second and third terms are its source and sink. The second term, the generation of kinetic energy, is modelled to be consistent with the Boussinesq hypothesis;

$$P_k \equiv -\bar{\rho}\widetilde{u_i'' u_j''}\frac{\partial \tilde{u}_j}{\partial x_i} = \mu_t S^2, \tag{3.8}$$

where S is the characteristic mean strain rate (the modulus of the mean rate of strain tensor), given as

$$S \equiv \sqrt{2\tilde{S}_{ij}\tilde{S}_{ij}}. \tag{3.9}$$

The standard equation for the dissipation rate, $\tilde{\varepsilon}$, is [97]

$$\frac{\partial}{\partial t}(\bar{\rho}\tilde{\varepsilon}) + \frac{\partial}{\partial x_i}(\bar{\rho}\tilde{\varepsilon}\tilde{u}_i) = \frac{\partial}{\partial x_i}\left[\left(\mu + \frac{\mu_t}{\sigma_\varepsilon}\right)\frac{\partial\tilde{\varepsilon}}{\partial x_i}\right] + C_{\varepsilon 1}\frac{\tilde{\varepsilon}}{\tilde{k}}P_k - C_{\varepsilon 2}\bar{\rho}\frac{\tilde{\varepsilon}^2}{\tilde{k}}, \tag{3.10}$$

where $C_{\varepsilon 1}$ and $C_{\varepsilon 2}$ are model constants, and σ_ε is the turbulent Prandtl number for dissipation. The standard values of the four constants used are $\sigma_k = 1.0$, $\sigma_\varepsilon = 1.3$, $C_{\varepsilon 1} = 1.44$ and $C_{\varepsilon 2} = 1.92$. The standard k-ε model has its limitations for certain flow types. The model constants can require careful tuning to give acceptable predictions for even simple flows such as the axisymmetric round-jet [97]. Numerous modifications to the standard k-ε model have been developed with a view to improving the predictions [79, 98, 107]. A modification to the $\tilde{\varepsilon}$ equation has been suggested to correct the round-jet anomaly, referred to as Pope's round-jet correction [98]. In general, it is not advantageous to tune constants as it reduces the generality of the model. A formulation of the $\tilde{\varepsilon}$ equation, developed to overcome this limitation, is known as the Realizable k-ε model [105] and is discussed next.

3.1.2 Realizable *k-ε* Closure

A deficiency in the standard k-ε closure is that the normal Reynolds stresses, $\bar{\rho}\widetilde{u_i''u_i''}$, can be negative. This can be caused in regions of high shear or large mean strain rates and can result in non-physical flow predictions. The Realizable k-ε model addresses this through the use of new forms of the dissipation equation and the turbulent viscosity formulation [104, 105, 120]. The *realizability* appears via a varying value of turbulent viscosity constant, C_μ. This feature ensures that in regions of large mean strain rates the values of the normal Reynolds stresses remain positive. This is not always the case for the standard k-ε closure, as can be seen by putting $i = j$ in Equation (3.5) and substituting

Equation (3.6). For the normal stresses in incompressible flow, this gives

$$\overline{u_i''}^2 = \frac{2}{3}\tilde{k} - 2C_\mu \frac{\tilde{k}^2}{\tilde{\varepsilon}} \frac{\partial \tilde{u}_i}{\partial x_i}. \tag{3.11}$$

The right hand side of Equation (3.11) becomes negative, and hence *non-realizable*, when

$$\frac{\tilde{k}}{\tilde{\varepsilon}} \frac{\partial \tilde{u}_i}{\partial x_i} > \frac{1}{3C_\mu} \approx 3.7, \quad \text{(if } C_\mu = 0.09\text{)}. \tag{3.12}$$

In addition, when the mean strain rate is large, the Schwarz inequality ($\overline{u_i'' u_j''}^2 \leq \overline{u_i''^2} \, \overline{u_j''^2}$, no summation over i and j) can be violated [103, 105]. The main advantage of the realizable k-ε closure is that it more accurately predicts the spreading of a round jet; a known problem with the standard k-ε closure [98]. However, the realizable k-ε closure is slightly more computationally intensive.

The turbulent kinetic energy, $\tilde{k}$, is found using Equation (3.7) as in the standard k-ε closure. A model for $\tilde{\varepsilon}$ is developed by forming a model equation for the dynamic equation of the mean-square vorticity fluctuation $\overline{\omega_i \omega_i}$, where $\omega_i = \epsilon_{ijk} \partial u_k' / \partial x_j$ is the vorticity of the fluctuating flow and ϵ_{ijk} is the alternation symbol. Using this equation, the model dissipation rate equation is found using the relation $\tilde{\varepsilon} = \nu \overline{\omega_i \omega_i}$, which is valid at large Reynolds numbers. The equation generated in this way is closer to the exact form of the $\tilde{\varepsilon}$ equation and simpler than the standard form. The modelled $\tilde{\varepsilon}$ equation is given as [104]

$$\frac{\partial}{\partial t}(\bar{\rho}\tilde{\varepsilon}) + \frac{\partial}{\partial x_i}(\bar{\rho}\tilde{\varepsilon}\tilde{u}_i) = \frac{\partial}{\partial x_i}\left[\left(\mu + \frac{\mu_t}{\sigma_\varepsilon}\right)\frac{\partial \tilde{\varepsilon}}{\partial x_i}\right] + \bar{\rho}\tilde{\varepsilon}C_1 S - \bar{\rho}C_2 \frac{\tilde{\varepsilon}^2}{\tilde{k} + \sqrt{\nu\tilde{\varepsilon}}} \tag{3.13}$$

where C_1 and C_2 are model constants. A summary of the model constants is given in

Table 3.1: Realizable k-ε turbulence closure constants [105].

σ_k	σ_ε	C_1	C_2	C_μ	A_0
1.0	1.2	Eq. (3.14)	1.9	Eq. (3.15)	4.04

Table 3.1. It is important to note that the main difference between Equations (3.13) and (3.10) is that the right hand side of Equation (3.13) does not contain any Reynolds stresses (through P_k) in the second (production) term. An expression for C_1 is found from the experimental data of homogeneous shear and boundary layer flow;

$$C_1 = \max\left[0.43, \frac{\hat{S}}{\hat{S}+5}\right], \tag{3.14}$$

where $\hat{S} = S\tilde{k}/\tilde{\varepsilon}$ and S is given by Equation (3.9). The value of C_2 is determined from experiments of large Reynolds number decaying grid-generated turbulence. The value of σ_ε is estimated using the log-law in a boundary layer flow [105].

The form of the isotropic eddy viscosity equation used in the standard k-ε closure is given by Equation (3.6), where C_μ is a fixed value of 0.09. However, homogeneous shear flow experiments have indicated $C_\mu \approx 0.05$ [105]. This variability of C_μ is captured in the realizable k-ε closure by

$$C_\mu = \left(A_0 + A_s U^* \frac{\tilde{k}}{\tilde{\varepsilon}}\right)^{-1}, \tag{3.15}$$

where

$$U^* \equiv \sqrt{\tilde{S}_{ij}\tilde{S}_{ij} + \tilde{\Omega}_{ij}\tilde{\Omega}_{ij}}, \tag{3.16}$$

and $\tilde{\Omega}_{ij}$ is the mean rate of rotation, $\tilde{\Omega}_{ij} = \frac{1}{2}(\partial\tilde{u}_i/\partial x_j - \partial\tilde{u}_j/\partial x_i)$. The parameter A_s is

calculated from

$$A_s = \sqrt{6} \cos \phi, \tag{3.17}$$

where

$$\phi = \frac{1}{3} \cos^{-1}(\sqrt{6}W), \tag{3.18}$$

$$W = 2^{3/2} \frac{\tilde{S}_{ij} \tilde{S}_{jk} \tilde{S}_{ki}}{S^3}. \tag{3.19}$$

The value of A_0 in Equation (3.15) is calibrated against simple flows, such as a homogeneous shear flow or boundary layer flow. For boundary layer flows, typical values are $C_\mu = 0.09$ and $A_0 = 4.04$ [105]. The realizable k-ε closure has been shown to perform well against the standard and RNG [97] k-ε closures for a confined jet in a cylindrical duct [120]. However, the realizable k-ε closure still requires the assumption of isotropy. An alternative which avoids the assumption of isotropy is to solve for each component of the Reynolds stresses directly.

3.1.3 Reynolds Stress Closure

As an alternative to using the Boussinesq hypothesis (introducing an isotropic turbulent viscosity) the individual Reynolds stresses are solved for directly [65]. This requires a significant increase in the number of transport equations that need to be solved; five in two-dimensional flows, seven in three-dimensions. As such, the Reynolds Stress (RS) closure is not widely used in industrial applications. However, it has the advantage of better performance than the isotropic turbulence closures (e.g. the standard k-ε closure) over a wide range of flows, particularly those featuring a high degree of anisotropy, such as turbulent jets.

The transport equations for the Reynolds stresses are given as

$$\frac{\partial}{\partial t}\left(\bar{\rho}\widetilde{u_i'' u_j''}\right) + C_{ij} = \frac{\partial}{\partial x_k}\left[\left(\mu + \frac{\mu_t}{\sigma_k}\right)\frac{\partial}{\partial x_k}\left(\widetilde{u_i'' u_j''}\right)\right] - P_{ij} + \Pi_{ij} - \frac{2}{3}\bar{\rho}\tilde{\varepsilon}\delta_{ij}. \tag{3.20}$$

The convection term, C_{ij}, is

$$C_{ij} = \frac{\partial}{\partial x_k}\left(\bar{\rho}\tilde{u}_k\widetilde{u_i'' u_j''}\right), \tag{3.21}$$

and the production term, P_{ij}, is

$$P_{ij} = -\bar{\rho}\left(\widetilde{u_i'' u_k''}\frac{\partial \tilde{u}_j}{\partial x_k} + \widetilde{u_j'' u_k''}\frac{\partial \tilde{u}_i}{\partial x_k}\right). \tag{3.22}$$

The first term in the RHS, the diffusion, uses the same turbulent diffusion gradient approach used in standard scalar transport. The turbulent Prandtl number in Equation (3.20) is $\sigma_k = 0.82$. The pressure-strain term, Π_{ij}, which controls the return to isotropy, is commonly modelled as

$$\Pi_{ij} = -C_1\bar{\rho}\frac{\tilde{\varepsilon}}{\tilde{k}}\left(\widetilde{u_i'' u_j''} - \frac{2}{3}\tilde{k}\delta_{ij}\right) - C_2\left[P_{ij} - C_{ij} - \frac{1}{3}\left(P_{kk} - C_{kk}\right)\delta_{ij}\right], \tag{3.23}$$

where $C_1 = 1.8$ and $C_2 = 0.6$. The last term on the RHS of Equation (3.23) is the viscous dissipation. Many models for Π_{ij} exist [97]. This linear form, Equation (3.23), is one of the simplest [97]. The $\tilde{\varepsilon}$ equation used is the same as in the standard k-ε closure, Equation (3.10).

3.2 Turbulence-Chemistry Interaction

Chemical reaction occurs when fuel and oxidizer meet at the molecular level at a temperature above activation. Modelling this reaction requires knowledge of the local mixture composition from either a species transport or conserved scalar approach. The species evolution and associated heat release are strongly coupled to the equations for continuity and momentum through the density. The Favre-averaged species balance equation for a generic species mass fraction, $\tilde{Y}_\alpha$, is given by

$$\frac{\partial}{\partial t}(\bar{\rho}\tilde{Y}_\alpha) + \frac{\partial}{\partial x_i}(\bar{\rho}\tilde{u}_i\tilde{Y}_\alpha) = -\frac{\partial}{\partial x_i}\mathcal{J}_{\alpha,i} + \bar{R}_\alpha. \tag{3.24}$$

The terms on the LHS represent the local rate of change and convection of species α. The terms on the RHS represent the diffusive flux, $\mathcal{J}_{\alpha,i}$, and the mean volumetric rate of production, $\bar{R}_\alpha$, of species α, respectively. Using the classical gradient assumption [89, 96],

$$\bar{\rho}\widetilde{u_i''Y_\alpha''} = -\frac{\mu_t}{\text{Sc}_t}\frac{\partial \tilde{Y}_\alpha}{\partial x_i}, \tag{3.25}$$

the diffusive flux is given by

$$\mathcal{J}_{\alpha,i} = -\bar{\rho}\left(D_\alpha^M + \frac{\nu_t}{\text{Sc}_t}\right)\frac{\partial \tilde{Y}_\alpha}{\partial x_i} - \frac{D_\alpha^T}{\tilde{T}}\frac{\partial \tilde{T}}{\partial x_i}, \tag{3.26}$$

where ν_t is the kinematic turbulent viscosity, Sc_t is the turbulent Schmidt number and $\tilde{T}$ is the temperature. D_α^M and D_α^T are the molecular and thermal diffusion coefficients of species α, respectively, calculated using kinetic theory (Appendix A.1) [32]. Thus, full multi-component transport properties are used. The first term on the RHS of Equation (3.26) represents the sum of turbulent and molecular diffusive fluxes. The second

term on the RHS of Equation (3.26) is the diffusion due to temperature gradients, known as the Soret effect. Both the laminar diffusion and Soret effect are often neglected due to their small contribution compared to that of turbulent diffusion [96]. However, they are retained in the present study due to the presence of H_2 (for which the molecular and thermal diffusivity is high) in the fuel stream [4, 95].

The Favre-averaged energy balance equation in its sensible enthalpy form [64, 96] is given by

$$\frac{\partial}{\partial t}(\bar{\rho}\tilde{h}_s) + \frac{\partial}{\partial x_i}(\bar{\rho}\tilde{u}_i\tilde{h}_s) = \frac{\partial}{\partial x_i}\left[\mathcal{K}\frac{\partial\tilde{T}}{\partial x_i} - \bar{\rho}\sum_{\alpha=1}^{n_s}\tilde{h}_{s,\alpha}\mathcal{J}_{\alpha,i}\right] - \sum_{\alpha=1}^{n_s}\frac{\Delta h_{f,\alpha}^0}{W_\alpha}\bar{R}_\alpha - \bar{\mathcal{Q}}, \tag{3.27}$$

where the gradient assumption has been used. The first three terms on the RHS represent the enthalpy flux due to conduction, species diffusion and chemical reaction. The last term on the RHS, $\bar{\mathcal{Q}}$ represents the radiative heat loss (see Section 3.4). The pressure work terms (negligible at low Mach numbers), the transient pressure (needed only primarily in reciprocating systems) and the viscous heating terms (negligible at low speeds) have been neglected [96]. In Equation (3.27) $\tilde{h}_{s,\alpha}$ is the sensible enthalpy of species α, $\Delta h_{f,\alpha}^0$ is the mass enthalpy of formation of species α and $\tilde{h}_s$ is the mixture sensible enthalpy given by

$$\tilde{h}_s = \sum_{\alpha=1}^{n_s}\tilde{Y}_\alpha h_{s,\alpha}, \quad \text{where} \quad h_{s,\alpha} = \int_{T_0}^{\tilde{T}} c_{p,\alpha}\,\mathrm{d}T. \tag{3.28}$$

The enthalpy flux due to conduction includes both laminar and turbulent contributions as

$$\mathcal{K} = \lambda + \frac{c_p\mu_t}{\mathrm{Pr}_t}, \tag{3.29}$$

where λ is the thermal conductivity calculated using kinetic theory (Appendix A.1) [11], c_p is the specific heat capacity of the mixture, μ_t is the dynamic turbulent viscosity and Pr_t is the turbulent Prandtl number. The mixture-averaged properties are calculated using Wilke's formula with Bird's correction for viscosity, and Mathur's combination averaging formula for thermal conductivity [11, 77, 118]. The mixture specific heat capacity is given by

$$c_p = \sum_{\alpha=1}^{n_s} c_{p,\alpha} \tilde{Y}_\alpha, \tag{3.30}$$

where $c_{p,\alpha}$ is the specific heat capacity of species α, given by a temperature-dependent piecewise-polynomial using Equation (A.1) [58]. The enthalpy flux due to species diffusion is calculated using Equation (3.26) which includes enthalpy flux due to species gradients, known as the Dufour effect. This term is usually neglected due its small contribution compared to turbulent diffusion [96]. However, where light species (compared to N_2 and O_2) such as H_2 are present, this effect can become important [95]. As such, it is retained in the present study. The final term in Equation (3.27) is the enthalpy flux due to chemical reaction through the mean rate of production, $\bar{R}_\alpha$, and the molecular weight, W_α, of species α.

The final term in the species equation and the penultimate term in the energy balance equation (Equations (3.24) and (3.27), respectively) still require closure. The challenge for turbulent combustion is to provide suitable closure methods for the mean volumetric rate of production, $\bar{R}_\alpha$. Such methods are discussed next.

3.2.1   Finite-Rate Kinetics

The general equation for the rth reaction involving the species α as reactants or products is written as

$$\sum_{\alpha=1}^{n_s} v'_{\alpha,r} \mathrm{M}_\alpha \underset{k_{b,r}}{\overset{k_{f,r}}{\rightleftharpoons}} \sum_{\alpha=1}^{n_s} v''_{\alpha,r} \mathrm{M}_\alpha, \tag{3.31}$$

where M_α is the chemical symbol of species α, $v'_{\alpha,r}$ and $v''_{\alpha,r}$ are the stoichiometric coefficients for the reactant and product α in reaction r, respectively, and $k_{f,r}$ and $k_{b,r}$ are the forward and backward reaction rate constants, respectively [66]. The molar rate of production of species α in reaction r is given by the law of mass action;

$$\dot{\omega}_{\alpha,r} = v_{\alpha,r} \Gamma \left[k_{f,r} \prod_{\beta=1}^{n_s} \left[X_\beta \right]^{v'_{\beta,r}} - k_{b,r} \prod_{\beta=1}^{n_s} \left[X_\beta \right]^{v''_{\beta,r}} \right], \tag{3.32}$$

where $[X_\alpha]$ is the molar concentration of species α and the difference in stoichiometric coefficients, $v_{\alpha,r}$, is given by

$$v_{\alpha,r} = v''_{\alpha,r} - v'_{\alpha,r}. \tag{3.33}$$

The effect of third-bodies on the reaction rate is included by

$$\Gamma = \sum_{\beta=1}^{n_s} \gamma_{\beta,r} \left[X_\beta \right], \tag{3.34}$$

where $\gamma_{\beta,r}$ is the third-body efficiency of species β in reaction r. If no third-body takes part in the reaction $\gamma_{\beta,r} = 1$ [58]. The rate constant for the forward reaction is modelled

using the modified Arrhenius form as

$$k_{f,r} = A_r T^{\beta_r} \exp\left(\frac{-E_r}{R_u T}\right), \tag{3.35}$$

where A_r is the pre-exponential factor, β_r is the temperature exponent, E_r is the activation energy and R_u is the universal gas constant. The backward rate constant is determined from the equilibrium constant using

$$k_{b,r} = \frac{k_{f,r}}{K_{c,r}}, \tag{3.36}$$

where $K_{c,r}$, the equilibrium constant in concentration units, is

$$K_{c,r} = \exp\left(\frac{\Delta S_r^0}{R_u} - \frac{\Delta H_r^0}{R_u T}\right) \cdot \left(\frac{p_{\text{atm}}}{R_u T}\right)^{\sum_\alpha \nu_{\alpha,r}}. \tag{3.37}$$

The enthalpy and entropy change during reaction r (ΔH_r^0 and ΔS_r^0, respectively) are obtained from polynomial fits [58]. The term within the exponential term is the change in Gibbs free energy. The pressure dependence of the reaction rate constants is accounted for using the Troe's fall-off formula [58, 66]. The Arrhenius rate parameters (A_r, β_r and E_r) for each reaction are tabulated for chemical mechanisms [58].

The total mass rate of production of species α is the sum of Equation (3.32) over each reaction r;

$$R_\alpha = W_\alpha \sum_{r=1}^{n_r} \dot{\omega}_{\alpha,r}. \tag{3.38}$$

If turbulent fluctuations of T are ignored, as could be the case in very low turbulence flames, then R_α can be used directly in Equations (3.24) and (3.27) in place of $\bar{R}_\alpha$. However, due to T appearing in the exponential term of Equation (3.35), even small fluctua-

tions of T can give large differences in reaction rate, thus $\bar{\omega} \neq \omega\left(\bar{p}, \bar{Y}_\alpha, \bar{T} \dots\right)$ [66]. This can be seen by expanding the reaction rate constant (Equation (3.35), with $B_r = A_r T^{\beta_r}$) with $T = \tilde{T} + T''$, assuming T'' is small and neglecting higher order terms [14, 66, 89];

$$
\begin{aligned}
k_{f,r} &= B_r \exp\left(\frac{-E_r}{R_u(\tilde{T} + T'')}\right) \\
&= B_r \exp\left(\frac{-E_r}{R_u \tilde{T}}\right)\left[1 + \left(\frac{E_r}{R_u \tilde{T}}\right)\frac{T''}{\tilde{T}} + \frac{1}{2}\left(\frac{E_r}{R_u \tilde{T}^2}\right)^2 \frac{T''T''}{\tilde{T}^2}\right].
\end{aligned}
\tag{3.39}
$$

Upon averaging, Equation (3.39) becomes

$$
\bar{k}_{f,r} = B_r \exp\left(\frac{-E_r}{R_u \tilde{T}}\right)\left[1 + \frac{1}{2}\left(\frac{E_r}{R_u \tilde{T}}\right)^2 \frac{\overline{T''T''}}{\tilde{T}^2}\right].
\tag{3.40}
$$

It becomes clear that the mean reaction rate depends on both the average and fluctuating temperature. For $\bar{k}_{f,r}$ to depend only on the mean temperature

$$
\frac{R_u \tilde{T}}{E_r} \gg \frac{\sqrt{\overline{T''T''}}}{\tilde{T}},
\tag{3.41}
$$

which only holds for very small fluctuations of temperature [66]. Consequently, a modelling approach that captures the effect of turbulent fluctuations and provides a mean rate of production is required.

3.2.2 Eddy Dissipation Concept

The Eddy Dissipation Concept (EDC) views a turbulent flame as a large number of Kolmogorov-size perfectly stirred reactors. The model is based on the turbulence energy cascade relating the fine-structures to the large scales represented by turbulence closures [74]. In a turbulent flow eddies of differing sizes exist. Energy is transported

in these eddies with the large eddies containing the majority of the kinetic energy. This kinetic energy is transferred from large eddies to eddies of smaller size. When the energy is transferred to eddies of sufficiently small scale, the energy is consumed by viscous dissipation [89]. This transfer process is known as the eddy cascade hypothesis. The size range of eddies is divided into differing subranges called (going from large to small) the large scale, integral scale, inertial subrange and viscous subrange [97]. A number of length, time and velocity scales can be defined at each level [97]. The smallest eddies, existing in the viscous subrange, are influenced by the viscosity of the fluid. A length scale known as the Kolmogorov scale, η, can be defined as [89]

$$\eta = \left(\frac{\nu^3}{\varepsilon}\right)^{1/4}, \tag{3.42}$$

which represents the characteristic size of the smallest eddy. A Kolmogorov time scale can also be defined as

$$t_\eta = \left(\frac{\nu}{\varepsilon}\right)^{1/2}, \tag{3.43}$$

which represents the turnover time for eddies of size η. The integral scales contain eddies with the most energy and are determined by the boundary conditions of the flow geometry. Similar time and length scales can be defined for the integral scale eddies;

$$\ell = \frac{k^{3/2}}{\varepsilon}, \tag{3.44}$$

$$t_\ell = \frac{k}{\varepsilon}. \tag{3.45}$$

The EDC was first proposed by Magnussen and Hjertager [74] and extended by

Magnussen [73] and co-workers [48, 75]. It is important to note that the EDC is distinct from the Eddy Dissipation Model (EDM) [74] despite being based on similar principles. Detailed finite-rate chemistry can be included with the EDC [48], whereas the EDM assumes combustion is mixing controlled, implying infinitely fast chemistry. The EDC gives an expression for the mean reaction rate for species as

$$\bar{R}_\alpha = \bar{\omega}_\alpha \bar{\rho} = \frac{\bar{\rho} \gamma^{*2}}{\tau^* \left(1 - \gamma^{*3}\right)} \left(Y_\alpha^* - \tilde{Y}_\alpha\right). \tag{3.46}$$

This assumes that chemical reactions occur in regions where the turbulence energy dissipation is intense. In moderately turbulent flows, these regions only occupy a small fraction of the flow, called *fine-structures*, indicated by the superscript $*$. Full details of this model are given in Gran [46] and Ertesvåg and Magnussen [38]. The terms appearing in Equation (3.46) and its formulation is described briefly below. A more detailed derivation is given in Appendix A.2.

The cascade model views the turbulence energy cascade as a stepwise model for energy transfer from large to small scales [97]. The large scales are related to the fine-structures where molecular mixing takes place by this stepwise mode and are generally modelled by turbulence closures such as the k-ε model. The turbulence energy cascade model takes the Favre-averaged turbulent kinetic energy, $\tilde{k}$, and an associated time or length scale (related to the dissipation, $\tilde{\varepsilon}$) from turbulence closure transport equations and returns the mean rate of molecular mixing. The EDC assumes the mean reaction rate to be a linear function of the mean molecular mixing rate. This dependence is shown explicitly by Bilger [8] in the fast-chemistry limit.

The EDC assumes that the local state of the fluid is expressed in terms of three parameters [38]; (i) the fine-structure state, ψ^*; (ii) the surrounding state, ψ°; and (iii) the fraction of fine-structures in the fluid, γ^*. The fraction of the flow occupied by the fine-

structures is given by

$$\gamma^* = \left(\frac{3C_\beta}{4C_\alpha{}^2}\right)^{1/4} \left(\frac{\nu^*\tilde{\varepsilon}}{\tilde{k}^2}\right)^{1/4}, \tag{3.47}$$

where ν^* is the kinematic viscosity of the fluid in the fine scales, and $C_\alpha = 0.134$ and $C_\beta = 0.50$ are model constants [38]. γ^* can be interpreted as the ratio of the fine-structure mass to the the total mass. Equation (3.47) can be written in terms of the Kolmogorov (η) and Taylor (λ) length scales;

$$\gamma^* = \left(100\frac{3C_\beta}{4C_\alpha{}^2}\right)^{1/4} \left(\frac{\eta}{\lambda}\right). \tag{3.48}$$

The volume fraction of the flow occupied by these fine-structures is modelled as γ^{*2} [38]. The time scale of the fine-scale mixing, τ^*, is modelled to be proportional to the Kolmogorov time scale as

$$\tau^* = \frac{1}{\dot{m}^*} = \left(\frac{C_\beta}{3}\right)^{1/2}\tau_\eta, \tag{3.49}$$

where $\dot{m}^*$ is the mass transfer between the fine-structures and the surroundings. The mean reaction rate, $\bar{\omega}_\alpha$, is assumed to be a linear function of the mean molecular mixing rate;

$$\bar{\omega}_\alpha = \frac{\gamma^{*2}}{\tau^*}(Y_\alpha^\circ - Y_\alpha^*), \tag{3.50}$$

where Y_α° is the species mass fraction in the surrounding fluid and Y_α^* is the species mass fraction in the fine-structure. Eliminating Y_α° in Equation (3.50) by using the state

equation

$$\tilde{Y}_\alpha = \gamma^{*3} Y_\alpha^* + \left(1 - \gamma^{*3}\right) Y_\alpha^\circ, \tag{3.51}$$

results in

$$\bar{\omega}_\alpha = \frac{\gamma^{*2}}{\tau^*} \left(\frac{\tilde{Y}_\alpha - \gamma^{*3} Y_\alpha^*}{1 - \gamma^{*3}} - Y_\alpha^* \right), \tag{3.52}$$

which, upon re-arrangement, gives Equation (3.46). To reduce numerical difficulties, the term $(\tilde{Y}_\alpha - Y_\alpha^*)$ is modified to allow relaxation of the solved mass fraction, $\tilde{Y}_\alpha$, to the fine-scale mass fraction, Y_α^* [45]. Thus, the mean reaction rate is expressed in terms of the variables that are calculated in a standard CFD simulation.

However, Equation (3.46) still includes one unknown term; Y_α^*, the fine-structure state. This is solved by treating the fine-structures as constant-pressure reactors, which also exchange mass with the surroundings via turbulent mixing. For this situation,

$$\frac{\mathrm{d} Y_\alpha^*}{\mathrm{d} t} = \omega_\alpha^* + \dot{m}^* \left(Y_\alpha^\circ - Y_\alpha^* \right), \tag{3.53}$$

where $\dot{m}^*$ is the mixing rate [83]. The choice of $\dot{m}^*$ and Δt determines the reactor type; for example if one takes $\dot{m}^*$ as the inverse of the residence time τ^*, then a perfectly stirred reactor (PSR) situation results. For a stationary PSR with τ^* as the residence time, Equation (3.53) gives;

$$\frac{Y_\alpha^* - Y_\alpha^\circ}{\tau^*} = \omega_\alpha^*, \tag{3.54}$$

where Y_α° is the mass fraction in the surrounding fluid from the previous iteration. A set of n_s coupled non-linear algebraic equations each featuring ω_α^* (depending only on Y_α

and T) are formed, with ω_α^* given by the solution of Equation (3.32). This additional calculation step is carried out at every iteration. To reduce computational time the ISAT algorithm (see Section 3.5.2) is used [100].

The EDC includes differential diffusion effects both in laminar and turbulent contexts. The non-unity turbulent Lewis number, Le_t, is obtained by specifying differing values of Schmidt and Prandtl numbers appearing in the averaged transport equations for energy and species.

3.2.3 Steady Laminar Flamelet Model

The Steady Laminar Flamelet Model (SLFM) views a turbulent flame as an ensemble of stretched laminar flamelets [90]. An outcome of this assumption is the separation of the flow solution into two problems: mixing and kinetics. Full derivations of the flamelet equations and the transport equations for mean mixture fraction, $\tilde{Z}$, and its variance, $\widetilde{Z''^2}$, are given in [90, 95]. To reduce the complexity a number of assumptions are made in the formulation [95]. For a non-reacting scalar such as the mixture fraction the transport equation can be written as [89]

$$\frac{\partial}{\partial t}(\bar{\rho}\tilde{Z}) + \frac{\partial}{\partial x_i}(\bar{\rho}\tilde{u}_i\tilde{Z}) = \frac{\partial}{\partial x_i}\left[\frac{\mu_t}{\sigma_{Z1}}\frac{\partial \tilde{Z}}{\partial x_i}\right], \tag{3.55}$$

where the gradient hypothesis has been used for the diffusion term on the RHS and the value of the turbulent Schmidt number is $\sigma_{Z1} = 0.85$ [39]. In the present work, the elemental (or Bilger) mixture fraction is used throughout [9]. For fuels containing C, H and O this is calculated by

$$Z = \frac{\frac{2(Y_C - Y_{C,2})}{W_C} + \frac{(Y_H - Y_{H,2})}{2W_H} - \frac{(Y_O - Y_{O,2})}{W_O}}{\frac{2(Y_{C,1} - Y_{C,2})}{W_C} + \frac{(Y_{H,1} - Y_{H,2})}{2W_H} - \frac{(Y_{O,1} - Y_{O,2})}{W_O}}, \tag{3.56}$$

where the subscripts 1 and 2 indicate elements originating in the fuel and oxidizer streams, respectively. Bilger's formulation preserves the stoichiometric value of mixture fraction, Z_{st}, when full multi-component transport (differential diffusion) effects are included [4]. The mixture fraction varies between 1 in the fuel stream to 0 in the oxidizer. The mixture fraction variance, $\widetilde{Z''^2}$, is given by [55, 96]

$$\frac{\partial}{\partial t}\left(\bar{\rho}\widetilde{Z''^2}\right) + \frac{\partial}{\partial x_i}\left(\bar{\rho}\tilde{u}_i\widetilde{Z''^2}\right) = \frac{\partial}{\partial x_i}\left[\frac{\mu_t}{\sigma_{Z1}}\frac{\partial \widetilde{Z''^2}}{\partial x_i}\right] + 2\frac{\mu_t}{\sigma_{Z2}}\left(\frac{\partial \tilde{Z}}{\partial x_i}\right)^2 - \bar{\rho}\tilde{\chi}, \tag{3.57}$$

where $\sigma_{Z2} = 0.7$ [39]. The Favre-averaged scalar dissipation rate, $\tilde{\chi}$, is given by

$$\tilde{\chi} = C_\chi \frac{\tilde{\varepsilon}}{\tilde{k}} \widetilde{Z''^2}, \tag{3.58}$$

with the time scale ratio taken as $C_\chi = 2$ [89]. The rate of mixing due to the turbulent transport is much higher than the mixing due to molecular transport. As such, molecular transport properties are neglected. The molecular diffusion coefficients for each species are assumed to equal to the thermal diffusion, implying a Lewis number, Le, of unity;

$$\text{Le}_\alpha = \frac{\lambda}{\rho c_p D_\alpha^M} = \frac{D^T}{D_\alpha^M} = 1. \tag{3.59}$$

This results in a large simplification of the model equations. Extension of the SLFM to include non-unity Lewis numbers, thus the effects of preferential diffusion, have also been considered in the past [95]. For this work the simpler and more commonly adopted formulation is used.

The steady counterflow flamelet equations are solved for all the species of interest and the temperature to provide information on the reaction rate [58, 71]. A modified transport subroutine is used to implement the unity Lewis number in OPPDIF [71]. The

flamelet solution is then parameterized using the mixture fraction, Z, and its dissipation rate, χ. This gives $\phi_i = \phi_i(Z, \chi)$ where ϕ_i is the mass fraction, Y_α, or temperature, T. The scalar dissipation rate, χ, represents the local mixing rate and is defined as

$$\chi = 2D \frac{\partial Z}{\partial x_i} \frac{\partial Z}{\partial x_i}, \tag{3.60}$$

where D is the diffusivity of Z, taken as the thermal diffusivity; $D = D^T$ [89]. The Favre-averaged species mass fraction and temperature (and hence density) are then obtained using

$$\tilde{\phi} = \iint \phi(Z, \chi) \tilde{P}(Z, \chi) \, dZ \, d\chi, \tag{3.61}$$

where $\tilde{P}$ is a probability density function (PDF). If one takes $\tilde{Z}$ and $\tilde{\chi}$ to be statistically independent for the sake of simplicity ($\tilde{\chi} = \chi$, strictly valid only at downstream locations; $x/d \gtrsim 40$ [37]), then the joint-PDF becomes $\tilde{P}(Z, \chi) = \tilde{P}(Z) \tilde{P}(\chi)$. The PDF of the mixture fraction is approximated using the β function. For computational simplicity $\tilde{P}(\chi)$ is taken to be a delta function, i.e. $\tilde{P}(\chi) = \delta(\chi - \tilde{\chi}_{\mathrm{st}})$ where $\tilde{\chi}_{\mathrm{st}}$ is the scalar dissipation at the stoichiometric mixture fraction, ignoring the fluctuations of χ [8, 89]. However, these fluctuations are known [94] to be important when there are local extinction and re-ignition events present in the flame. Since the flames considered in this work are not thought to include these events, a simple model such as given above is believed to be sufficient.

3.2.4 Other Closure Methods

The presented reaction rate closure models (EDC and SLFM) are only a small sample of the available models. Their selection in this study was primarily based on their ability

to combine finite-rate kinetics and comparatively modest computational requirements. Other approaches are also in widespread use. A discussion of these approaches follows.

The joint Probability Density Function (jPDF) model [89, 99] is an approach which involves a transport equation for the joint PDF of velocities and reactive scalars. An advantage of the jPDF model is that the chemical source term can be treated exactly, without further modelling [89]. Unclosed terms, such as molecular mixing, require appropriate models [97]. The jPDF is solved using the Monte-Carlo technique due to the high dimensionality of the PDF transport equation. This treats the flow as a large number of particles, each with its own composition, velocity and position. The greater the number of particles, the higher the accuracy. However, to achieve suitable accuracy for turbulent combustion a large number of particles (and, thus, computation effort) is required. The ISAT algorithm (Section 3.5.2) can be used to reduce the computational effort [70]. The jPDF model has been applied to wide range of flows with good results [70, 89].

Conditional Moment Closure (CMC) is an approach for turbulent combustion where reactive scalars are conditioned on the mixture fraction in non-premixed flames [63]. A conditionally averaged transport equation of this scalar can then be formed. Unclosed terms, such as the Favre conditional velocity, still appear and require modelling. The chemical source term is calculated using conditional averages, as mass fraction and temperature fluctuations are expected to be related to mixture fraction fluctuations [14]. The CMC approach is still an ongoing area of study. Recent studies have shown good results for non-premixed flames [60, 61].

Large-Eddy Simulation (LES) is an approach where filtering is used to separate the large (where the majority of the energy is contained) and small scale turbulent motions [97]. The large unsteady three-dimensional motions are solved directly, whereas the smaller motions are modelled. As the computational effort is less than DNS, LES

is now being used successfully in research and industry [94, 109]. A tabulated mixture fraction-based approach to chemistry is often used, similar to the SLFM [89]. However, the computational requirements are still greater than traditional RANS simulations.

3.3 NO_x Formation

NO_x prediction has been the focus of much work for a number of years due to regulatory and social pressures. The chemistry involved is well understood [31, 81]. However, its application to turbulent combustion is still an evolving area [53, 60]. Total NO_x values are usually taken as the sum of NO, NO_2 and N_2O values, representing the three main routes of formation. The three distinct routes are: (i) the thermal (Zel'dovich) mechanism, (ii) the prompt (Fenimore) mechanism, and (iii) the N_2O-intermediate mechanism [113]. These three routes individually become prevalent under different conditions. For example, in flames with hydrocarbon fuels the thermal and prompt routes contribute due to the presence of CH and HCN radicals [42, 112]. However, in non-hydrocarbon fuels containing combinations of H_2 and CO (such as syngas) only the thermal route is active, with the prompt and N_2O contributing only insignificant amounts [42]. High pressures increase the rate of formation of N_2O, while high temperatures (> 1500 K) increase the rate of conversion of N_2O back to NO [12]. In this work high temperatures and pressures are considered, and the fuel does not include any hydrocarbon component. As such, the prompt and N_2O routes are not thought to be important.

The focus in this study is on the thermal NO, described through the following three

Table 3.2: Reaction mechanism rate coefficients [m³/mol·s] for NO_x in the form $k_f = A_r T^{\beta_r} \exp(-T_{act}/T)$ [51].

	Forward Rate			Backward Rate		
	A_r	β_r	T_{act}	A_r	β_r	T_{act}
Z1	1.8×10^{11}	0	38 370	3.8×10^{10}	0	425
Z2	1.8×10^{7}	1	4680	3.8×10^{6}	1	20 820
Z3	7.1×10^{10}	0	450	1.7×10^{11}	0	24 560

reactions [12];

$$N_2 + O \rightleftharpoons NO + N, \tag{Z1}$$

$$O_2 + N \rightleftharpoons NO + O, \tag{Z2}$$

$$N + OH \rightleftharpoons NO + H. \tag{Z3}$$

Reaction (Z1) has a large activation temperature (38 370 K [51]) as a large amount of energy is required to break the strong N_2 triple bond. A consequence of this is that the formation of NO increases rapidly with temperature. In general, thermal NO is considered negligible below 1800 K [113]. In addition, as the availability of O atoms is important for Reaction (Z1), NO levels generally peak on the lean (oxidizer) side of the flame. However, temperature is the dominant controlling factor. The rate coefficients for Reactions (Z1)–(Z3) are given in Table 3.2.

The formation of NO_2 is known [111] to become important under lean operating conditions and high pressures. The main NO_2 formation route is via

$$NO + HO_2 \rightleftharpoons NO_2 + OH, \tag{N1}$$

which is active at temperatures below 1500 K [12] where the NO_2 removal, via [66]

$$NO_2 + H \rightleftharpoons NO + OH \tag{N2}$$

or

$$NO_2 + O \rightleftharpoons NO + O_2, \tag{N3}$$

is quenched due to the lack of H and O radicals. At higher temperatures the conversion of NO_2 to NO is rapid.

Calculation of NO_x levels are generally conducted via two approaches: (i) direct calculation via full or reduced kinetics, or (ii) via simplifying steady-state and/or partial equilibrium assumptions. The first approach uses detailed kinetic mechanisms, such as GRI-Mech 2.11 [13] and GRI-Mech 3.0 [108] developed for methane combustion, to explicitly calculate all the chemistry involved in NO_x formation. The latter approach assumes that the energy changes from NO formation are so small that it can be thermally decoupled from the main combustion process [112]. This allows NO levels to be post-processed from known temperature and radical fields. The normal procedure assumes that N atoms are in steady-state.

To calculate the rate of formation of NO_x using the post-processing method the mechanism needs to be simplified using a number of assumptions. Firstly, as the NO_x formation processes are slow compared to the fast reactions of H_2 ($\tau_{NO} \gg \tau_{H_2}$), the two processes can be decoupled [113]. The N radicals react so quickly once they are formed that their concentrations do not continue to rise but reach steady-state concentration [44]. This steady-state approximation for the species N allow the rate of formation equation of N to be set equal to zero; $d[N]/dt = 0$. With this assumption the

rate of formation of NO is given by

$$\frac{\mathrm{d[NO]}}{\mathrm{d}t} = 2k_{f,Z1}[N_2][O]\frac{\left(1 - \frac{k_{b,Z1}k_{b,Z2}[NO]^2}{k_{f,Z1}[N_2]k_{f,Z2}[O_2]}\right)}{\left(1 + \frac{k_{b,Z1}[NO]}{k_{f,Z2}[O_2]+k_{f,Z3}[OH]}\right)}, \tag{3.62}$$

where the rate constants are given in Table 3.2 [51, 81]. This equation can be solved for given values for temperature and the species concentrations. However, if O and OH radicals are not solved for, two further assumptions can be made. In high temperature systems it can be assumed that O_2 and O are in partial equilibrium; that the forward and reverse reaction rates of the elementary reaction are equal [116]. The forward and reverse reaction rate coefficients in $O_2 \rightleftharpoons 2\,O$ are much faster than the slow NO formation. The partial equilibrium concentration of O is given by [114]

$$[O] = 36.64T^{1/2}[O_2]^{1/2}e^{-27\,123/T}. \qquad [\mathrm{mol/m^3}] \tag{3.63}$$

If OH is also assumed to be in partial equilibrium, its concentration can be calculated using [115]

$$[OH] = 2.129 \times 10^2 T^{-0.57}e^{-4595/T}[O]^{1/2}[H_2O]^{1/2}. \qquad [\mathrm{mol/m^3}] \tag{3.64}$$

Substituting Equations (3.63) and (3.64) into Equation (3.62) gives the NO formation rate in terms of $[N_2]$, $[H_2O]$, $[O_2]$ and T. These simplifications are frequently adopted when infinitely fast chemistry is assumed, such as with the Eddy Dissipation Model [53].

If turbulent fluctuations are ignored, as in laminar flames, then the source term in the $\tilde{Y}_{NO}$ transport equation, $\bar{R}_{NO}$, is calculated using

$$\bar{R}_{NO} \equiv R_{NO} = W_{NO}\frac{\mathrm{d[NO]}}{\mathrm{d}t}. \tag{3.65}$$

The species transport equation can then be solved as a post-processing step. However, as NO_x formation is highly dependent on T, turbulent fluctuations need to be considered in turbulent flames. This can be achieved by using an assumed-shape PDF to calculate the mean source term;

$$\bar{R}_{NO} = \int_0^1 R_{NO} \tilde{P}(\mathcal{T}) \, d\mathcal{T}, \tag{3.66}$$

where $\mathcal{T}$ is the normalized temperature varying between the minimum and maximum temperatures in the flame. A beta-PDF shape is assumed, calculated using

$$\tilde{P}(\mathcal{T}) = \mathcal{T}^{\alpha-1}(1-\mathcal{T})^{\beta-1} \frac{\Gamma(\alpha+\beta)}{\Gamma(\alpha)\Gamma(\beta)} \tag{3.67}$$

where Γ is the gamma function, and α and β are given by $\alpha = \tilde{\mathcal{T}}\gamma$ and $\beta = (1-\tilde{\mathcal{T}})\gamma$, where $\gamma = \tilde{\mathcal{T}}(1-\tilde{\mathcal{T}})/\tilde{\sigma}^2 - 1$. The variance of $\mathcal{T}$, $\tilde{\sigma}^2$, is given by [53]

$$\tilde{\sigma}^2 = \frac{\mu_t \tilde{k} C_g}{\bar{\rho} \tilde{\varepsilon} C_d} \left[\left(\frac{\partial \tilde{\mathcal{T}}}{\partial x} \right)^2 + \left(\frac{\partial \tilde{\mathcal{T}}}{\partial y} \right)^2 + \left(\frac{\partial \tilde{\mathcal{T}}}{\partial z} \right)^2 \right], \tag{3.68}$$

with the model constants taken as $C_g = 2.86$ and $C_d = 2.0$. This is simply an approximated transport equation for temperature variance with production set equal to dissipation. The additional term in the transport equation for variance, $2\overline{\mathcal{T}''\dot{\omega}_{\mathcal{T}}''}$, is usually neglected in Equation (3.68). The implications of this are being studied as they may have a significant general contribution.

3.4 Radiation Model

As described in Section 3.3, NO_x predictions are highly dependent on local flame temperatures. Assuming adiabatic flame conditions generally leads to an over-prediction

of flame temperatures and hence NO_x. The adiabatic assumption can give acceptable results in highly dilute H_2 flames. However, in most hydrocarbon flames thermal radiation reduces the local temperatures sufficiently to alter NO_x predictions [5]. For H_2/CO flames the main radiating species (H_2O and CO_2) are present in the combustion products. In addition, the CO existing in the fuel stream can contribute to the heat loss by radiation. This implies that radiation could have an impact on temperature and NO_x predictions.

Detailed computational models exist for the description of radiation within reacting flows [25]. However, these models are computationally expensive. A highly simplified treatment of radiative heat loss has been developed with the focus on turbulence-chemistry interaction[a]. This involves the assumption that the flames are optically thin; each radiating point source has an unimpeded isotropic view of the cold surroundings [5]. The radiative heat loss rate in Equation (3.27) is calculated using a Boltzmann relation;

$$\bar{\mathcal{Q}} = 4\sigma_{SB}\left(\tilde{T}^4 - T_b^4\right)\sum_\alpha p_\alpha a_{P,\alpha} \quad \text{for } \alpha = H_2O, CO_2, CO, \tag{3.69}$$

where p_α and $a_{P,\alpha}$ are the partial pressure and Planck mean absorption coefficient, respectively, for species α and T_b is the background temperature. σ_{SB} is the Stefan-Boltzmann constant. Equation (3.69) is solved for α radiating species, which in this work is assumed to be CO, CO_2 and H_2O only. The values of $a_{P,\alpha}$ are calculated from polynomial curve-fits [5] using

$$a_{P,\alpha} = c_0 + c_1\hat{T} + c_2\hat{T}^2 + c_3\hat{T}^3 + c_4\hat{T}^4 + c_5\hat{T}^5 \quad \text{for } H_2O \ \& \ CO_2, \tag{3.70}$$

---

[a]The TNF workshop; http://public.ca.sandia.gov/TNF

Table 3.3: Curve-fits for Planck mean absorption coefficients used in the radiation model, valid only between $300 < T < 2500$ K. Data taken from Barlow et al. [5].

	H_2O	CO_2	CO	
			$300 \leq T \leq 750$ K	$750 \leq T \leq 2500$ K
c_0	−0.23093	18.741	4.7869	10.09
c_1	1.12390	−121.310	−0.06953	−0.01183
c_2	9.41530	273.500	2.95775e-4	4.7753e-6
c_3	−2.99880	−194.050	−4.25732e-7	−5.87209e-10
c_4	0.51382	56.310	2.02894e-10	−2.5334e-14
c_5	−1.86840e-5	−5.8169	—	—

where $\hat{T} = 1000/\tilde{T}$, and

$$a_{\mathrm{P,CO}} = c_0 + \tilde{T}(c_1 + \tilde{T}(c_2 + \tilde{T}(c_3 + c_4\tilde{T}))) \qquad \text{for CO.} \qquad (3.71)$$

Values of the curve-fit coefficients c_0–c_5 are given in Table 3.3.

3.5   Numerical Details

The Favre-averaged equations presented in this chapter are solved using the commercial CFD code FLUENT [39]. This code is used in both industry and academia, and has been shown to give good predictions for a wide range of turbulent reacting flows; Kim and Mastorakos [61], Lee and Mastorakos [68], Liu and Pope [70], Masri et al. [76], Pitsch [93], and Coelho and Peters [26].

3.5.1 Discretization

A pressure-based segregated solver [39] is used to calculate the mass, momentum, energy, mixture fraction, its variance, and species equations. A second-order central difference scheme is used for diffusion terms. A second-order upwind scheme is used for convective terms. A staggered grid is used for momentum as this prevents occurrence of undesirable 'checkerboard' patterns in velocity and pressure [87]. The SIMPLE algorithm [88] is used to couple velocity and pressure [87]. Given appropriate boundary conditions and a suitable initial field, the variables are solved iteratively until convergence is achieved. Second-order interpolation provides increased accuracy over first-order or linear interpolation. This increase in accuracy is important when an accurate temperature field is needed, as is the case when pollutants such as NO_x are of interest.

3.5.2 ISAT Algorithm

The ISAT algorithm (*in situ* adaptive tabulation) is a computational technique that can decrease the magnitude of computer time needed to solve reacting flows by three orders of magnitude [100]. The technique is primarily used with the PDF turbulent combustion model [15, 16] but it has been used with other approaches such as finite-rate chemistry and the EDC [39]. The general procedure is described briefly below.

At any point in a reactive flow the state of the mixture can be characterized by the species mass fractions, Y_i, the enthalpy, h_s, and the pressure, p. Assuming that p differs by a very small fraction from a fixed reference pressure p_0, i.e. atmospheric, allows the state to be determined, given p_0, by

$$\Phi = \{\phi_i \mid i = 1, \dots, n_s + 1\} = \{\tilde{Y}_1, \tilde{Y}_2, \dots, \tilde{Y}_{n_s}, \tilde{h}_s\}, \tag{3.72}$$

where n_s is the number of species. The state vector, Φ, contains components that are not linearly independent; the mass fractions must sum to unity, and there may be additional dependencies based on element or enthalpy conservation. If there are n_l linear dependencies , the degrees of freedom of the thermochemistry is given by [100]

$$D = n_s + 1 - n_l. \tag{3.73}$$

The greater the number of species, the greater the degrees of freedom and computational effort required. A composition vector, ϕ, can be defined as a linearly independent subset of Φ;

$$\phi = \{\phi_i \mid i = 1, \dots, D\}. \tag{3.74}$$

Given p_0 and knowledge of the linear dependencies in the system the thermochemical state of the system is determined by ϕ.

In the ISAT algorithm, a subset of all the realizable points of ϕ is defined as the accessed region. This accessed region, containing all compositions ϕ that occur in the flow, is much smaller than the realizable region. The ISAT algorithm reduces the overall calculation time of a simulation by using a tabulation procedure where only the accessed region of ϕ need be calculated and stored. The size and shape of the accessed region depends heavily on many aspects of the flow (such as boundary conditions, kinetics, transport processes) and is unknown prior to the calculation. This means that the tabulation is not conducted as a pre-processing step, but is built-up over the course of the calculation; referred to as *in situ* tabulation.

The ISAT algorithm begins with an empty table. Consider a simplified reaction equa-

tion integrated over Δt;

$$\phi^1 = \phi^0 + \int_0^{\Delta t} S \, dt, \qquad (3.75)$$

where S is the chemical source term, and ϕ^0 is the initial composition [100]. This is integrated using a stiff ODE solver in the usual manner; referred to as a Direct Integration (DI). The solution, ϕ^1, is known as the reaction mapping and maps the initial condition $\phi(t^0) = \phi^0$ to the reacted value $\phi(t^0 + \Delta t) = \phi^1$. The reaction mapping ϕ^1 is stored in the table, along with its mapping gradient matrix A, at the location defined by ϕ^0, and the calculation proceeds to the next iteration. The next reaction mapping is calculated by defining a query composition vector; ϕ_q^0. The table (of one entry) is queried by linearly interpolating the new mapping, ϕ_q^1, using

$$\phi_q^1 = \phi^1 + A(\phi_q^0 - \phi^0), \qquad (3.76)$$

with $A = \frac{\partial \phi^1}{\partial \phi^0}$.

The new mapping is checked to see if it is located within an ellipsoid of accuracy (EOA); the hyper-ellipsoid of space around the composition vector ϕ^0 where the linear approximation to the mapping is accurate to a specified tolerance, ϵ_{tol}. If it is, then the linear approximation given by Equation (3.76) is sufficiently accurate and the mapping is returned. This procedure is known as a retrieve, and is less computationally intensive than a DI. If ϕ_q^1 is outside the EOA, a DI is performed to determine the mapping ϕ_{DI}^1. The mapping error is determined using

$$\epsilon_{\text{map}} = \left| B(\phi_{\text{DI}}^1 - \phi_q^1) \right|, \qquad (3.77)$$

where B is a scaling matrix; a diagonal matrix including normalized species mole fractions (normalized by an estimate of the maximum mole fraction range of all species included in the problem) and the normalized enthalpy (normalized by an estimate of the maximum enthalpy range in the problem) [100]. If $\epsilon_{map} < \epsilon_{tol}$ then ϕ_q^1 given by interpolation is sufficiently accurate and the EOA is grown so that ϕ_q^0 is included. If $\epsilon_{map} > \epsilon_{tol}$ then a new table entry is added. These two stages of error checking achieves the Adaptive Tabulation of ISAT.

These procedures (queries, retrieves, grows and adds) are repeated over the course of the calculation. At the start of the calculation, there are many more adds and grows which are time-consuming. As the calculation progresses, and the table gets larger, there are many more retrieves where are less time-consuming; hence the calculation accelerates.

3.5.3   Chemical Kinetic Modelling

Chemical kinetic modelling is conducted using the CHEMKIN suite of applications [57, 58]. Equilibrium calculations are conducted using the perfectly stirred reactor (PSR) program [43]. Opposed-flow laminar diffusion flames are simulated using OPPDIF [71]. In OPPDIF, the equations presented earlier in this chapter are solved in their one-dimensional, laminar form; ignoring turbulent fluctuations. Detailed thermal and mass diffusion effects are included.

3.6   Summary

In this chapter details have been given of the governing equations used for the simulations in the following chapters. The differing reaction rate models (specifically the EDC and SLFM) are, at first look, vastly different in approach. However, when the

combination of the EDC and ISAT is considered then a similarity appears. Both use a form of tabulation to perform look-ups and determine the reaction rate. With the SLFM the table is *pre*-processed, whereas with the EDC it is formed *concurrently* with the flow solution. Both reaction rate models incorporate finite-rate chemistry effects, unlike the EDM. The following chapters discuss the development and validation of a reduced chemical mechanism for use with the EDC and SLFM, which is then tested in turbulent flames.

Chapter 4

Kinetic Mechanism

In this chapter the development of a reduced $H_2/CO/N_2$ kinetic mechanism is presented. The reduced mechanism includes only those species which take an active role in the reaction, thus reducing the total number of scalars that need to be solved. As discussed in Section 2.3, accurate representation of the kinetics, via an appropriate mechanism, is paramount in capturing the underlying physics of a $H_2/CO/N_2$ flame. As such, the reduced mechanism is validated against comprehensive mechanisms using laminar opposed-flow diffusion flames.

The aim is to determine to what degree a reduced $H_2/CO/N_2$ mechanism can reasonably approximate a full mechanism when applied to an opposed-flow laminar diffusion flame. Specifically, the interest is to assess the ability of reduced mechanisms to capture both NO_x formation and CO consumption in a non-premixed flame of reformate gases at (i) atmospheric temperature and pressure (ATP), and (ii) high temperature and pressure conditions (HTP). This will indicate the applicability of the mechanism for industrial burners, such as the SOFC hybrid off-gas burner.

4.1 Background

A variety of industrial processes, such as solid oxide fuel cells, now make use of synthetic gas or reformate gases with the aim of improving efficiency or reducing CO_2 emissions. These synthetic gases contain high levels of CO and H_2. Computational models to predict NO_x and CO levels in syngas mixtures at atmospheric and high pressure conditions are not yet available. Computationally efficient chemical mechanisms are integral to the development of such models.

Much work has been conducted on the reduction of CH_4 mechanisms by applying steady-state assumptions [10, 78, 91, 108]. There is a renewed interest in H_2/CO mechanisms to supplement the widely-used GRI mechanism for natural gas [18, 36, 92, 110]. There is, however, only limited work on reduced H_2/CO mechanisms. Rogg and Williams used a four-step reduced mechanism derived for methane [91] and applied it to wet CO laminar premixed flames [102]. By removing the methane consumption reaction a 3-step mechanism was formed:

$$CO + H_2O \rightleftharpoons CO_2 + H_2, \tag{RW-I}$$

$$2\,H + M \rightleftharpoons H_2 + M, \tag{RW-II}$$

$$O_2 + 3\,H_2 \rightleftharpoons 2\,H + 2\,H_2O. \tag{RW-III}$$

This set of semi-global reactions was also used for modelling turbulent non-premixed jet flames using the PDF method [23].

In H_2/CO mixtures the oxidation process is controlled by a smaller set of species and reactions than in hydrocarbon flames. Hence, any mechanism reduction made may be highly sensitive to individual reactions and species but the reduction in number of species is limited. Detailed kinetic information is necessary to retain the oxidation character-

istics in simulations which use the reduced mechanism. Nitrogen chemistry introduces a large number of intermediate species. However, the number of reactions and species can be considerably reduced by limiting the intermediate steps considered.

In this chapter, we expand on the work of Chen [22], Chen et al. [24], Rogg and Williams [102] and Drake and Blint [35] on the reduction of H_2/CO oxidation mechanisms to include NO_x formation. High temperatures, pressures and different fuel and oxidizer compositions compared to the previous studies are considered. The reduced mechanism developed is tested against axisymmetric counterflow laminar diffusion flame solutions using both the starting mechanism and the widely-used GRI-Mech 3.0 mechanism. Comparison is also made with the experimental results of Drake and Blint [34].

4.2 Numerics

Perfectly stirred reactor and laminar flame simulations are carried out using the CHEM-KIN suite of applications [58]. The reaction rates for each species are calculated using a modified subroutine [57]. The flame configuration studied is an axisymmetric counterflow, adiabatic, laminar diffusion flame, which is simulated using OPPDIF [71]. Second-order central differencing for diffusive terms and first-order upwind differencing for convective terms are used. The fluid is assumed to be an ideal gas. The viscosity and thermal conductivity of each species are calculated using kinetic theory [11]. The mixture-averaged properties are calculated using Wilke's formula with Bird's correction for viscosity, and Mathur's combination averaging formula for thermal conductivity [11, 77, 118]. Mass and thermal diffusion coefficients are calculated using kinetic theory. The multi-component mass and thermal diffusion properties are calculated using the Dixon-Lewis method [32]. Both the Dufour and Soret effects are included, as are

the effects of non-unity Lewis number. Specific heats are calculated from temperature dependent polynomials. Details of these physical properties are given in Chapter 3 and Appendix A.1.

4.3   Mechanism Selection

As a starting point for reduction a comprehensive H_2/CO mechanism, including recent updates to both H_2 and CO kinetics, is chosen based on its performance over ranges of temperatures, pressures and flame configurations [30]. This mechanism uses more up-to-date rate data than used in the previous works [23, 102], including recent reviews of H_2/CO/O_2 kinetics [30, 119]. This mechanism has been optimized and validated against reliable H_2/CO combustion data, including shock-tube ignition delays, laminar flame speeds and extinction strain rates [30, 106]. The starting mechanism compares favourably to GRI-Mech 2.11 and 3.0 for H_2/CO flames [30]. As the starting mechanism contains no nitrogen chemistry the relevant reactions are added from the GRI-Mech 2.11 [13]. Details of the starting mechanism including the nitrogen chemistry used in this study are given in Appendix B.1. The older version of GRI-Mech is preferred for NO_x chemistry on the basis of its predictions for lean and near-stoichiometric flames [5, 84, 101].

4.4   Reduction Procedure

The Computer Assisted Reduction Mechanism (CARM) Code [19–21] is used to produce a reduced mechanism from a detailed starting mechanism. Based on the results of zero-dimensional perfectly stirred reactor (PSR) calculations at conditions of interest, quasi-steady-state assumptions are made to reduce the number of species [20]. PSR

calculations are conducted for a range of conditions of interest. The results of these calculations (including species concentration, sensitivity and rate-of-production) are used by CARM to determine the relative importance of the elementary reactions. A skeletal mechanism is developed first by removing unimportant elementary steps and species using normalized first-order sensitivity coefficients, production and destruction rates. An appropriate cut-off level is set for this process. Next, the species which are likely to be in quasi-steady-state are identified. The level of reduction is determined by setting the total number of species desired. The quasi-steady-state species are then eliminated and a set of independent elementary reactions is formed using detailed algebraic procedures, yielding the reduced mechanism [19].

4.5   Test Cases

In this study, four syngas compositions are chosen to match those typically found in industrial settings, as shown in Table 4.1. Case A corresponds to the experimental and computational work of Drake and Blint [34]. Case B corresponds to the off-gas burner operating at atmospheric conditions [50]. The value of calculated flame stretch is used to relate the modelled flames to those present in the off-gas burner. The conditions for Case C are chosen to match the actual conditions in the off-gas burner at high temperature and pressure [50]. Case D corresponds to the experimental and computational work of Barlow et al. [4].

4.6   Results and Discussion

The following three sets of reductions are made using CARM for lean H_2/CO flames:

    1. a 3-step H_2/CO mechanism (see Section 4.1), excluding nitrogen chemistry, fol-

Table 4.1: Boundary conditions used for the four test cases investigated. X_α is the mole fraction of species α, T is the temperature, $\dot{m}$ is the mass flow rate per unit area, p is the pressure, a_{nom} is the nominal flame stretch, and Z_{st} is the stoichiometric mixture fraction.

		Case			
		A	B	C	D
Fuel Stream	X_{H_2}	0.3	0.38	0.11	0.3
	X_{CO}	0.4	0.25	0.16	0.4
	X_{N_2}	0.3	0.37	—	0.3
	X_{H_2O}	—	—	0.32	—
	X_{CO_2}	—	—	0.41	—
	T [K]	395	300	1111	292
	$\dot{m}$ [kg/m$^2 \cdot$s]	0.655	0.051	0.0761	0.506
Oxidizer Stream	X_{O_2}	0.21	0.21	0.12	0.206
	X_{N_2}	0.79	0.79	0.65	0.783
	X_{H_2O}	—	—	0.11	0.011
	X_{CO_2}	—	—	0.11	—
	X_{Ar}	—	—	0.01	—
	T [K]	298	300	1126	290
	$\dot{m}$ [kg/m$^2 \cdot$s]	1.239	0.121	0.1021	0.724
	p [bar]	1.013	1.013	7.0	1.013
	a_{nom}[a] [s^{-1}]	70.0	34.5	177.8	—
	Z_{st}[b]	0.295	0.393	0.5	0.295

[a] The nominal flame stretch is calculated using $a_{nom} = (v_{fuel} + v_{oxid})/l$, where v_i is the fuel or oxidizer stream velocity and l is the nozzle separation (domain length).

[b] The stoichiometric Bilger mixture fraction [9].

lowing the procedure detailed in [91, 102];

2. a 6-step mechanism including NO formation chemistry for both atmospheric (ATP) and high temperature and pressure (HTP) conditions using simulated reformate mixtures similar to those present in the off-gas burner; and

3. a 7-step mechanism including NO_2 for lean, low temperature chemistry at both ATP and HTP conditions using simulated reformate mixtures.

Comparison of the reduced mechanisms to the starting mechanism and the GRI-Mech 3.0 methane mechanism are given in the form of species and temperature profiles.

4.6.1   3-step H_2/CO-Air Diffusion Flame

The starting mechanism is reduced from 38 steps to three using CARM [21]. This results in the same set of reactions (RW-I to RW-III) as presented by Rogg and Williams [102], given in Section 4.1. The difference occurs in the calculation of the global reaction rates where more up-to-date rate data is used than in the previous works [23, 102]. This includes recent reviews of H_2/CO/O_2 kinetics [30, 119]. The 13 species present in the starting mechanism are reduced to 6 (as N_2 and Ar are assumed to take no part in the reaction) by assuming that five species (O, OH, HO_2, HCO and H_2O_2) are in steady-state. Reaction (RW-III) represents the chain initiation and oxygen consumption step. Reaction (RW-II) represents the hydrogen recombination step, and Reaction (RW-I) represents the CO combustion step. Nitrogen chemistry is not included in this mechanism.

An OPPDIF calculation is conducted using the conditions for Case B. Figure 4.1 shows a comparison of the reduced three-step mechanism to the starting [30] and GRI-Mech 3.0 [108] mechanisms for temperature, T, and species mole fractions, X_α, against mixture fraction, Z, calculated using the Bilger approach [9]. The three-step mechanism is seen to be in good agreement to the starting mechanism. The only deviation is for H
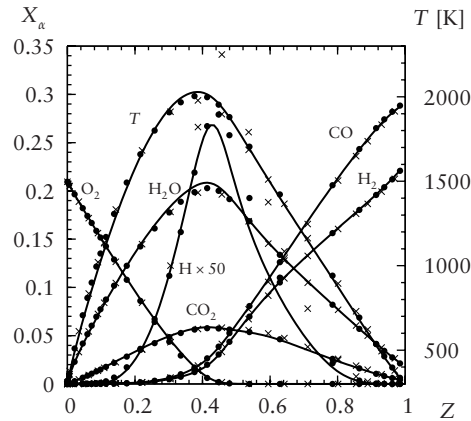
Figure 4.1: Comparison of OPPDIF predictions for Case B using full and reduced mechanisms for H_2/CO: — 3-step mechanism, • starting mechanism [30] and × GRI-Mech 3.0 mechanism [108].

which is slightly under-predicted by the reduced mechanism in the rich region; $0.4 < Z$ since Z_{st} = 0.393. The GRI-Mech 3.0 mechanism over-predicts the peak H value by about 20%. However, overall the three mechanisms are in good agreement.

4.6.2   6-step $H_2/CO/N_2$-Air Diffusion Flame at ATP

In this case the starting mechanism (with nitrogen chemistry) is reduced with a focus on the prediction of NO levels. At the flame conditions expected in atmospheric burners, the contribution to the overall NO_x level by NO_2 and N_2O is expected to be small due to the short residence times. Therefore it is reasonable to focus on the calculation of NO concentrations. During the reduction process the selection of quasi-steady-state species is made to ensure species relevant to NO formation are included in the reduced set. Previous work on NO_x in diffusion flames has identified the importance of explicitly calculating the O level [34].

The resulting 6-step mechanism produced by CARM is:

$$H + O_2 \rightleftharpoons O + OH, \tag{I}$$

$$H_2 + O \rightleftharpoons H + OH, \tag{II}$$

$$H_2 + OH \rightleftharpoons H + H_2O, \tag{III}$$

$$2H + M \rightleftharpoons H_2 + M, \tag{IV}$$

$$O + CO \rightleftharpoons CO_2, \tag{V}$$

$$2H + 2NO \rightleftharpoons N_2 + O + H_2O. \tag{VI}$$

The 30 species in the starting mechanism are reduced to 10. All species but H_2, O_2, CO, CO_2, H_2O, O, H, OH, N_2 and NO are assumed to be in quasi-steady-state. The majority of species removed are from the nitrogen chemistry included from GRI-Mech 2.11. The net reaction rates for the 6-step mechanism are given in Appendix B.2.

The 6-step mechanism is used with OPPDIF for Cases A, B and D. For Case A the reduced mechanism predicts a peak flame temperature of 2029 K compared to the experimental value of 2040 K [34]. The peak flame temperatures using the starting and GRI-Mech 3.0 mechanisms are 2031 K and 2000 K, respectively. The 6-step reduced mechanism provides acceptable agreement to experiment in this limited comparison. Further comparison is not made due to large experimental uncertainties in species profiles present.

Results using the conditions for Case B are given in Figure 4.2. Figure 4.2a shows a comparison of the reduced 6-step mechanism to the starting and GRI-Mech 3.0 mechanisms for temperature, T, and species mole fraction, X_α, profiles against the mixture fraction, Z. The 6-step reduced mechanism gives very good agreement with the starting mechanism for all major species. A similar agreement is seen between the GRI-Mech 3.0
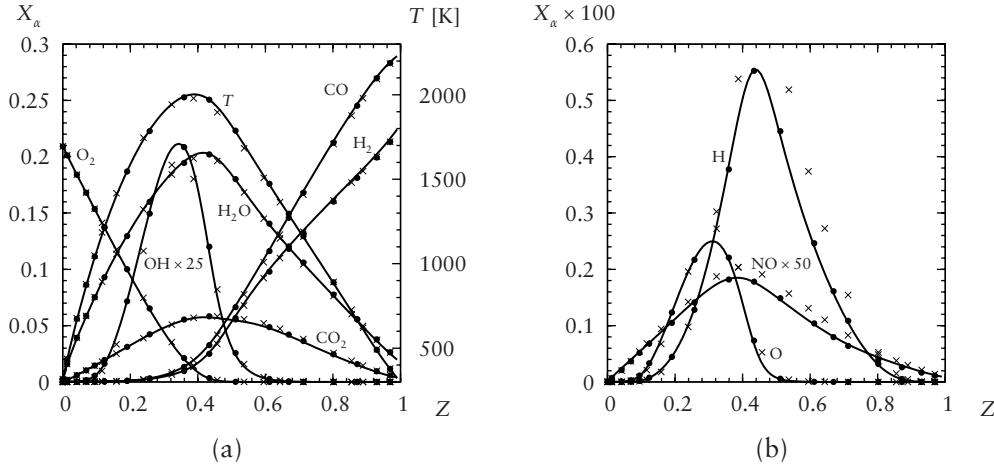
Figure 4.2: Comparison of OPPDIF predictions for Case B using full and reduced mechanisms for $H_2/CO/N_2$: —— 6-step mechanism, • starting mechanism [30] and × GRI-Mech 3.0 mechanism [108].

mechanism and the reduced mechanism. Only a slight difference in peak temperature is seen: the GRI-Mech 3.0 mechanism predicts a slightly lower value than the starting mechanism and the 6-step reduced mechanism, by about 18 K in both cases.

Figure 4.2b shows the variation of minor species with Z. The starting mechanism gives an overall lower value for H and O than obtained using the GRI-Mech 3.0 mechanism. The peak values from GRI-Mech 3.0 are also shifted slightly to the rich side when compared to those from the starting mechanism. However, the reduced mechanism gives good agreement with the starting mechanism in both cases. The calculated values for NO show a similar trend, with the values for GRI-Mech 3.0 being slightly higher than the starting mechanism. This is consistent with previously published findings [84, 101]. The reduced mechanism slightly over-predicts (< 1%) the peak NO mole fraction.

The maximum flame temperature, T_{max}, from OPPDIF calculations using the conditions of Case D over a range of stoichiometric scalar dissipation rates, χ_{st}, are given in
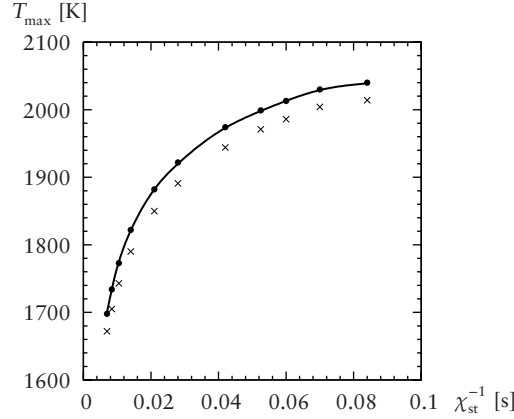
Figure 4.3: Maximum flame temperature, $T_{\max}$, against the inverse of the scalar dissipation rate at stoichiometric conditions, χ_{st}, for Case D: —— 6-step mechanism, • starting mechanism [30] and × GRI-Mech 3.0 mechanism [108].

Figure 4.3. The stoichiometric scalar dissipation rate is calculated using [89]

$$\chi_{st} = \chi\left(Z_{st}\right) = \frac{2a_{nom}}{\pi} \exp\left(-2\left[\mathrm{erfc}^{-1}\left(2Z_{st}\right)\right]^2\right), \tag{4.1}$$

where Z_{st} is the stoichiometric mixture fraction. The inverse stoichiometric scalar dissipation rate values plotted correspond to a nominal flame stretch range of 25–300 s^{-1}. The reduced 6-step mechanism gives excellent agreement to the starting mechanism. GRI-Mech 3.0 gives slightly lower values of maximum flame temperature but by less than 2% across the range.

Good overall agreement is found between the 6-step, 13 species mechanism and the original 116 reactions, 30 species mechanism. Therefore, its use in stretched diffusion flame calculations appears to be justified. In addition, the CPU time required for a converged solution is greatly reduced (×0.25) with the 6-step mechanism compared to GRI-Mech 3.0, consistent with the ratio of scalars involved; 53 scalars in GRI-Mech 3.0.

4.6.3   6-step H$_2$/CO/N$_2$-Air Diffusion Flame at HTP

The same 6-step reduced mechanism developed in Section 4.6.2 is applied to HTP conditions on the basis that these conditions are matched to those expected in the off-gas burner. Figure 4.4a shows a comparison of the calculated species mole fractions and temperature. An excellent agreement is found for all species and temperature. The only discrepancy appears in the prediction for OH, with GRI-Mech 3.0 over-predicting and shifting the region of high values to the rich side when compared to the starting and reduced mechanisms.

Figure 4.4b shows a comparison of the calculated minor species mole fractions. The reduced mechanism agrees well with the starting mechanism for all species. The peak values and their locations are captured. There is some difference between the reduced and starting mechanisms and GRI-Mech 3.0. GRI-Mech 3.0 tends to over-predict peak values generally, and NO where $Z > 0.5$. A difference is seen with the prediction of NO where $Z > 0.6$ with the reduced mechanism over-predicting the values and not capturing the concentration in the fuel-rich range. This is presumably because the HCN chemistry included from GRI-Mech 2.11 is having no effect on the NO level due to the lack of CH radicals. However, the overall prediction of NO using the reduced mechanism is very good (within 1% of the starting mechanism for $Z < 0.5$) and, again, consistent with the findings of Barlow et al. [5], Naha and Aggarwal [84], and Ravikrishna and Laurendeau [101].

4.6.4   7-step H$_2$/CO/N$_2$-Air Diffusion Flame

In diffusion flames the overall NO$_x$ level (usually taken as the sum of NO and NO$_2$) is determined by the NO level due to the short residence times and stoichiometric conditions (cf. Figures 4.2b and 4.4b, the NO profile closely follows that of temperature). How-
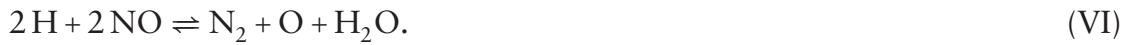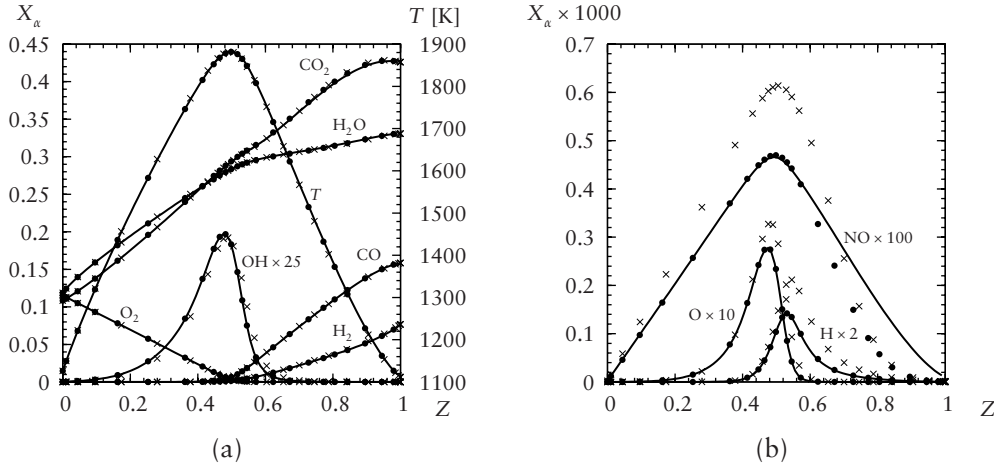
Figure 4.4: Comparison of OPPDIF predictions for Case C using full and reduced mechanisms for $H_2/CO/N_2$: —— 6-step mechanism, • starting mechanism [30] and × GRI-Mech 3.0 mechanism [108].

ever, the performance of a reduced mechanism in overall lean conditions, such as those expected to be found downstream of lean-burning industrial burners, is also of interest. At very lean, low temperature conditions, the reactions involving NO_2 become more important [113]. The main route of formation is via $NO + HO_2 \rightleftharpoons NO_2 + OH$. However, HO_2 levels are not specifically calculated in the 6-step mechanism. A reduction of the starting mechanism is made to include NO_2 resulting in a seven-step mechanism by the addition of

$$OH + NO \rightleftharpoons H + NO_2 \tag{VII}$$

to the 6-step mechanism. For both ATP and HTP conditions Reaction (VII) is found to be dominant over the $NO + HO_2 \rightleftharpoons NO_2 + OH$ step when compared with the full mechanism. At HTP conditions, Reaction (VII) is approximately 15 times more active than $NO + HO_2 \rightleftharpoons NO_2 + OH$. At ATP conditions Reaction (VII) is approximately twice as active. This appears to justify the exclusion of HO_2 from both the 6- and 7-step

(a) Case B
(b) Case C
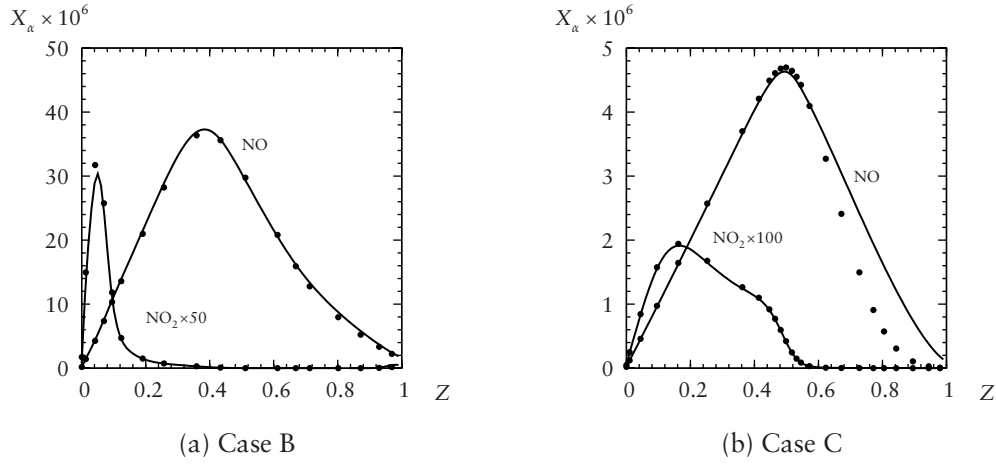
Figure 4.5: Comparison of OPPDIF predictions for Cases B and C using full and reduced 7-step mechanisms for $H_2/CO/N_2$: —— 7-step mechanism and • starting mechanism [30]

mechanisms.

The 7-step mechanism applied to the same conditions described earlier produces no noticeable difference from the results for major species and temperatures shown in Figure 4.2 and 4.4 for the 6-step mechanism. Figure 4.5 shows profiles for NO and NO_2 against mixture fraction for both sets of conditions. For HTP conditions a slight reduction (< 1.5%) in peak NO mole fraction is seen when compared to the starting mechanism, shown in Figure 4.5b. For ATP conditions a slight increase (< 1.1%) in peak NO mole fraction is seen when compared to the starting mechanism, shown in Figure 4.5a. These slight differences can be explained by the NO_2 mole fraction profiles. With the HTP case NO_2 is being formed at lean conditions from $0 < Z < 0.5$ since $Z_{st} = 0.5$. The reactions involving NO and NO_2 ($HO_2 + NO \rightleftharpoons NO_2 + OH$ and $NO_2 + O \rightleftharpoons NO + O_2$) become significant at lean conditions and high concentrations. For ATP conditions, NO_2 is only formed in very lean conditions; $Z \lesssim 0.2$ since $Z_{st} = 0.393$. An excess concentration of O_2 results in the overall formation of NO_x ($OH + NO \rightleftharpoons H + NO_2$) shifting towards NO_2, which is in agreement with an earlier study [35].

The predictions of NO_2 using the 7-step reduced mechanism compare well with the starting mechanism, particularly at HTP.

4.7 Summary

This chapter set out to determine if a reduced $H_2/CO/N_2$ mechanism could reasonably approximate a full mechanism when applied to an opposed-flow laminar diffusion flame at ATM and HTP conditions, with unusual dilute reformate gases. A 3-step mechanism (excluding nitrogen chemistry) is tested against the starting and GRI-Mech 3.0 mechanisms. Good agreement is found between the reduced and starting mechanism. A 6-step mechanism including NO chemistry from GRI-Mech 2.11 is tested against the full starting and GRI-Mech 3.0 mechanisms at both atmospheric and high temperature and pressure conditions. Good agreement is found in both cases for major species and temperature profiles. A 7-step mechanism, including NO_2, is tested against the 6-step and starting mechanisms. Again, good agreement is found for all major species and temperature profiles, as well as NO_x, over a range of flame stretch values. Overall, it is observed that the 6- and 7-step reduced mechanisms developed here give good approximations of the starting mechanism and capture all the relevant kinetics for both atmospheric and high temperature and pressure conditions for stretched laminar diffusion flames. This gives confidence for the application of the mechanism to turbulent combustion modelling as will be tested in Chapter 5. Reaction rates used in the reduced mechanisms are listed in Appendix B for reference.

Chapter 5

Model Validation Cases

In this chapter the validation of the reduced mechanism from Chapter 4, integrated with the numerical and modelling framework from Chapter 3, is presented. The reduced mechanism is used to calculate two flame configurations. These flames use syngas fuels at atmospheric conditions. The syngas has a composition similar to those used in the atmospheric off-gas burner experiments. The flames that have been selected have high turbulence levels providing a tougher test for the mechanism and underlying turbulence-chemistry interaction models. Turbulence-chemistry interaction has a large impact on NO_x formation and CO consumption through fluctuations of temperature.

The primary goal of the present chapter is to validate the predictions of simple turbulence and kinetic models against experimental results on practical turbulent flames of syngas-air mixtures. Syngas mixtures provide an interesting challenge for turbulent combustion computations as the kinetics are of intermediate complexity; being simpler than hydrocarbon kinetics, but more complex than hydrogen kinetics. If the models developed perform well, their application as a design tool to the SOFC hybrid off-gas burner, and other syngas burners, would be justified.

5.1   Background

The present chapter considers validation of the modelling procedure against two exper-
imental targets: (i) the work by Correa and Gulati on a bluff-body stabilized diffusion
flame [28], and (ii) the work on jet diffusion flames by Barlow et al. [4]. In the former
study [28], there is a recirculation zone downstream of the bluff-body which stabilizes
the flame. An accurate representation of the recirculation zone, by the use of an appro-
priate turbulence model, is required to ensure correct flame stabilization. In the second
study [4], preferential (or differential) diffusion effects are observed to be important in
these flames since hydrogen is a major component of the fuel. Numerical simulations
which fail to represent these effects have been shown to suffer blow-off. Furthermore,
the combination of fast-reacting hydrogen and slow-reacting carbon monoxide in the
syngas fuel mixtures, and the requirement for accurate NO_x prediction, requires finite-
rate kinetics to be included in any simulation.

These flames have been studied to develop and test different aspects of turbulent
combustion models [29, 46, 48, 49, 60, 62]. Both the standard k-ε model, corrected
for the round-jet anomaly [98], and the Reynolds stress turbulence closure were used in
those studies. The level of complexity used for modelling chemistry has ranged from fast
1- and 2-step mechanisms [29, 48] to full kinetics with 22 species and 102 reactions [60].
In some cases [62] the NO_x was post-processed using the Zel'dovich mechanism. In the
present work recent updates to H_2/CO kinetics will be included with the SLFM and
EDC, and combined with the realizable k-ε and linear RS turbulence closures.

Previous modelling work on the Correa and Gulati bluff-body flame used the stan-
dard k-ε model in conjunction with an assumed-shape PDF model with library-based
chemistry using only the kinetics of recombination reactions [28]. This chemistry clo-
sure was also used with the joint-PDF model [29]. Acceptable differences between the

predicted scalar profiles and experiment were reported, and these differences were attributed to the simplified chemistry and non-equilibrium effects at low temperatures. The Reynolds stress (RS) model has also been used with the Eddy Dissipation Concept (EDC) [74] incorporating detailed chemistry, with good results compared to experiment [48]. However, when the EDC with detailed finite-rate chemistry was used with the standard k-ε model, the computed flame was observed to become unstable and blew off due to the incorrect prediction of the mixing field particularly in the recirculation zone [48].

The Barlow et al. [4] jet flame from the TNF workshop [6] is widely used for turbulent combustion validation as the flame is geometrically simple and of intermediate complexity with regards to chemical kinetics [4, 6]. Previous published work modelling this flame have used the steady and unsteady flamelet models [62], LES-based approaches [41], and CMC [60]. Kim et al. [62] and Kim et al. [60] utilized the standard k-ε model with Pope's correction [98], fuel kinetics from Warnatz et al. [114], and a full 66-step and skeletal 33-step NO_x mechanism, respectively. Giacomazzi et al. [41] utilized a reduced 6-step mechanism [22] as well as single step fast chemistry for both H_2 and CO.

The modelling details are presented in the next section, followed by a discussion on the boundary conditions. The results of the present computations are compared to published experimental and computational results in Section 5.5. The conclusions of this validation study are summarized in the last section.

5.2 Numerics

In the present work, the reduced 6-step $H_2/CO/N_2$ kinetic mechanism described in Chapter 4 [27] is applied to two flame configurations which use syngas fuel: (i) a bluff-

body stabilized flame [28] and (ii) a jet flame [4]. Detailed experimental species profiles are available. Two different turbulent combustion modelling approaches are used: (i) the Steady Laminar Flamelet Model [90] and (ii) the Eddy Dissipation Concept [74]. Two turbulence closures are adopted: (i) the realizable k-ε closure [105] and (ii) the Reynolds stress closure [65]. Although more advanced models and approaches are available, e.g. jPDF, CMC and LES, the interest in this work is to benchmark the simplest models and to test their predictive abilities for syngas flames by comparing simulation results with experiments. The motivation is primarily to minimize computational time at acceptable accuracy for use in design and parametric studies. The 7-step mechanism developed in Chapter 4 is not used as the presented cases are at atmospheric pressure, where the contribution of NO_2 to the total NO_x is believed to be negligible, as discussed in Section 3.3.

The governing equations described in Chapter 3 are solved using the commercial CFD code FLUENT [39]. Full multi-component transport is used when the EDC is used, as described in Section 3.2. Simpler transport, with unity Lewis numbers, is used with the SLFM as described in Section 3.2.3. Second order upwind discretization is used for all scalars along with the PRESTO scheme for pressure, as discussed in Section 3.5.1 [87]. The SIMPLE algorithm [87] is used to maintain the pressure-velocity coupling. A solution is considered to be converged when the scaled residuals are below 10^{-6} and the energy balance is of the order of 10^{-2} W. In the present study, the realizable k-ε closure converges faster, and with greater stability, than the RS closure. Once suitable flamelets are generated using OPPDIF [58], the SLFM converges more quickly, by nearly an order of magnitude compared to the EDC approach.

For the bluff-body flame, the flamelet library comprises 12 flamelets with scalar dissipations ranging from 9 to 240 s^{-1}, corresponding to stretch values, a_{nom}, of 15 to 400 s^{-1}. For the jet flame, the library comprises 12 flamelets with scalar dissipations

ranging from 7 to 170 s^{-1}, corresponding to stretch values of 15 to 355 s^{-1}.

5.3   CFD-Kinetics Interface

For the EDC calculation, a modified form of the CHEMKIN CKWYP [58] subroutine calculates the molar production rates using the reduced mechanism developed in Chapter 4 given the pressure, temperature and species mass fractions [21]. The six global reaction rates are expressed in terms of the elementary rates as functions of the steady-state species; see Appendix B.2. This subroutine can be called independently from CHEMKIN. The commercial CFD code used in this study, FLUENT, has a built in kinetics solver for the EDC and finite-rate models which uses tabulated Arrhenius reaction rates similar to those used in CHEMKIN [39]. However, reduced reactions can not be expressed as simple Arrhenius rates without simplifications which lose the details of the chemistry. A specific User Defined Function (UDF) [39] is used to replace the rates of production, R_α, generated by the CFD code with those calculated using the CKWYP subroutine for the EDC. Values of $\tilde{T}$, $\bar{p}$ and $\tilde{Y}_\alpha$ for each cell are retrieved by the UDF during each iteration cell loop, converted to the appropriate units, and passed to the external CKWYP subroutine, as shown schematically in Figure 5.1. The CKWYP subroutine calculates and returns to the UDF molar rates of production, $\dot{\omega}_\alpha$, which are then converted to mass rates, R_α. These are then used by the EDC to calculate $\bar{R}_\alpha$ as discussed in Section 3.2.2.

An additional UDF is used to reconstruct the Bilger mixture fraction, Z, using the mass fractions at each cell following Warnatz et al. [114] to allow further comparison with the SLFM and experiment.
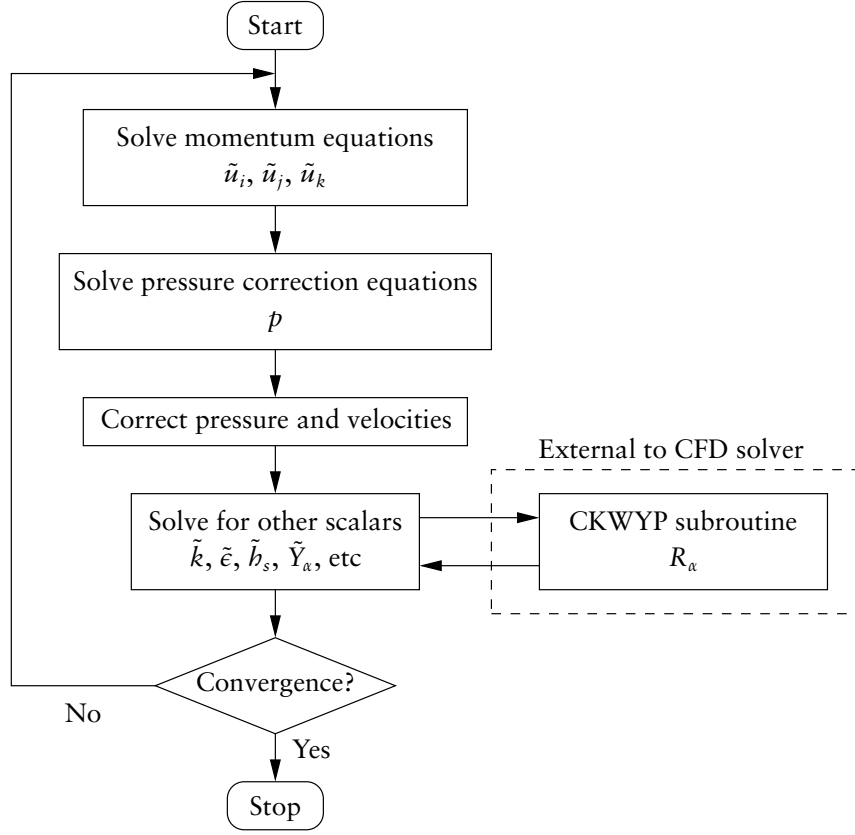
Figure 5.1: Schematic of SIMPLE algorithm [87] showing CFD-kinetics interface.

5.4   Boundary Conditions

Four cases (denoted as A, B, C and D) are calculated for both the bluff-body and jet flames using the realizable k-ε or RS model for turbulence closure, and the EDC or SLFM for reaction rate modelling as specified in Table 5.1. Cases A and B use the EDC with the realizable k-ε and RS closures, respectively. Cases C and D use the SLFM with the realizable k-ε and RS closures, respectively. All calculations for the present work use the reduced 6-step mechanism for chemical kinetics [27].

A general schematic of the computational domain used in this study is given in Figure 5.2, with characteristic dimensions as noted in Table 5.2. The computational domain

Table 5.1: Simulation cases for both the bluff-body flame and the jet flame.

Case	Turbulence Closure	Combustion Model
A	Realizable k-ε	EDC
B	RS	EDC
C	Realizable k-ε	SLFM
D	RS	SLFM
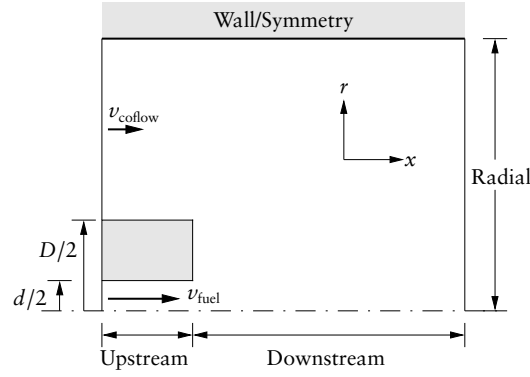
Figure 5.2: Schematic of the computational domain for the bluff-body; not to scale. The same layout also applies to the jet flame, except the bluff-body becomes an infinitely thin wall; $D/2 = d/2$. Actual dimensions are given in Table 5.2.

is extended upstream of the fuel port to allow the flow to develop and reduce the sensitivity of calculations to turbulence boundary conditions. Inlet profiles are assumed to be top-hat in shape. Details of the boundary conditions are given in Table 5.3. The integral turbulent length scale at the upstream inlets is calculated assuming fully-developed flow using $\ell = 0.07d_h$, where d_h is the hydraulic diameter. All walls are assumed adiabatic and to have no slip. The pressure on the downstream boundary is set to to be atmospheric.

For the bluff-body flame the experimental configuration extends radially to 152.0 mm in a square cross-section wind tunnel [28]. The computational domain is axisymmetric, with an area approximately matching the outer radius to the experimental square

Table 5.2: Details of computational domain for the bluff-body and jet flames. Geometric dimensions taken from Correa and Gulati [28] for the bluff-body flame and Barlow et al. [4] for the jet flame.

	Bluff-Body	Jet
Fuel jet diameter, d [mm]	3.18	7.72
Bluff-body diameter, D [mm]	38.1	—
Upstream extent, x/d	6	5
Downstream extent, x/d	55	120
Radial extent, r/d	27	30

Table 5.3: Boundary conditions for bluff-body and jet flame calculations. Boundary conditions taken from Correa and Gulati [28] for the bluff-body flame and Barlow et al. [4] for the jet flame.

	Bluff-Body		Jet	
	Fuel	Coflow	Fuel	Coflow
Bulk velocity, v_{bulk} [m/s]	80.0	6.5	45	0.75
Turbulence intensity, I [%]	5.0	3.0	10.0	2.0
Temperature, T [K]	300	300	292	290
X_{H_2}	0.323	—	0.3	—
X_{CO}	0.275	—	0.4	—
X_{N_2}	0.402	—	0.3	—
X_{O_2}	—	0.21	—	0.206
X_{N_2}	—	0.79	—	0.783
X_{H_2O}	—	—	—	0.011

cross-section. An adiabatic, no slip wall boundary condition is used at the radial extent. The wall location is sufficiently far away so as not to affect the flow in the area of interest. For the jet flame, the pipe wall is assumed to be infinitely thin ($d = D$ in Figure 5.2) for computational simplicity. A symmetry (zero gradient) boundary condition at the radial extent was used, as the experimental configuration is unconfined. Heat loss to the inlet fuel pipe is neglected, although this is known to have some effect on experimental flame stability [3]. Radiative heat transfer was neglected in all simulations unless otherwise stated, on the assumption that the flame is optically thin. The pressure is atmospheric (101 kPa).

A non-uniform axisymmetric grid is used for each flame, given in Figures 5.3 and 5.4. The bluff-body flame used 100 cells axially and 96 cells radially; the grid density was increased until results obtained showed little change. The grid used is finer than those used in previous studies of the same flame [28, 29, 47]. The upstream fuel pipe is resolved with 16 cells across the radius and 20 cells in the axial direction. The bluff-body diameter is resolved with 40 cells in order to provide sufficient mesh density to capture the recirculation region. The jet flame uses 200 cells axially and 85 radially; again, the grid density was increased until the results showed little change. The grid used is similar to previous piloted jet flame studies [15]. The fuel pipe is resolved with 10 cells across the radius and 18 cells axially. In both flames, the cell spacing is varied to ensure high mesh density at the fuel pipe outlet and in the area of high shear. In addition, the cell spacing growth rate is kept sufficiently small to reduce numerical error.
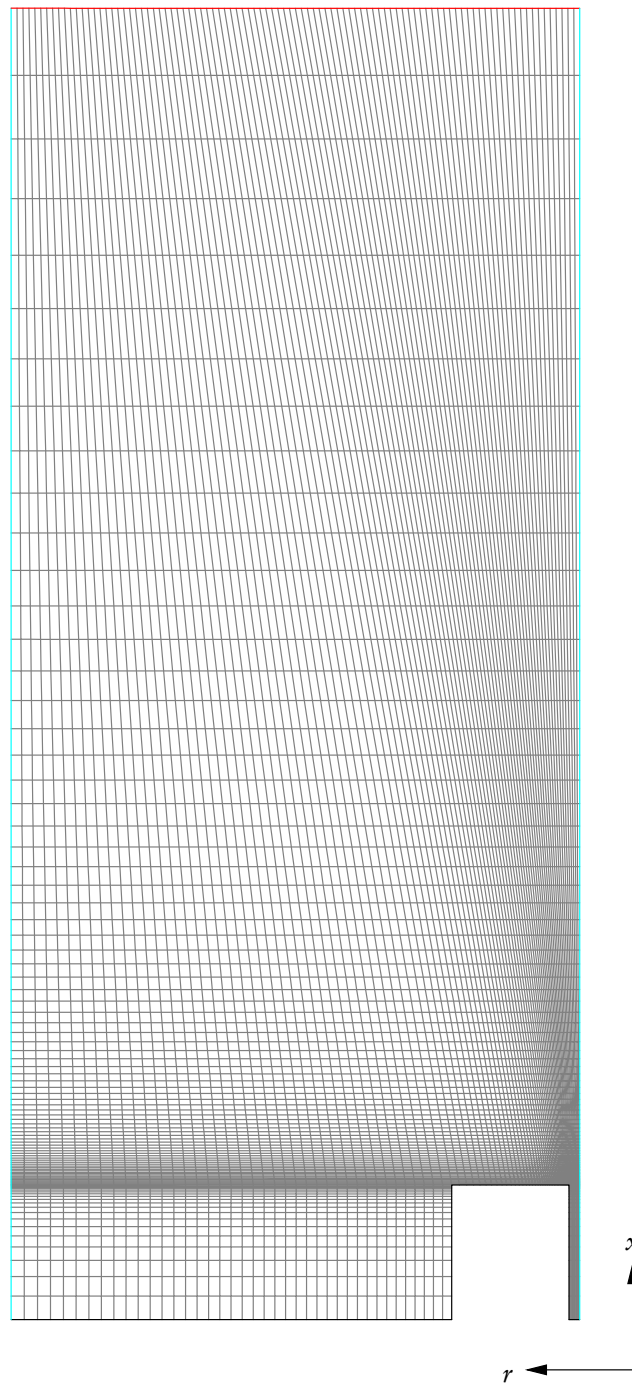
Figure 5.3: Computational mesh used for bluff-body flame calculations.
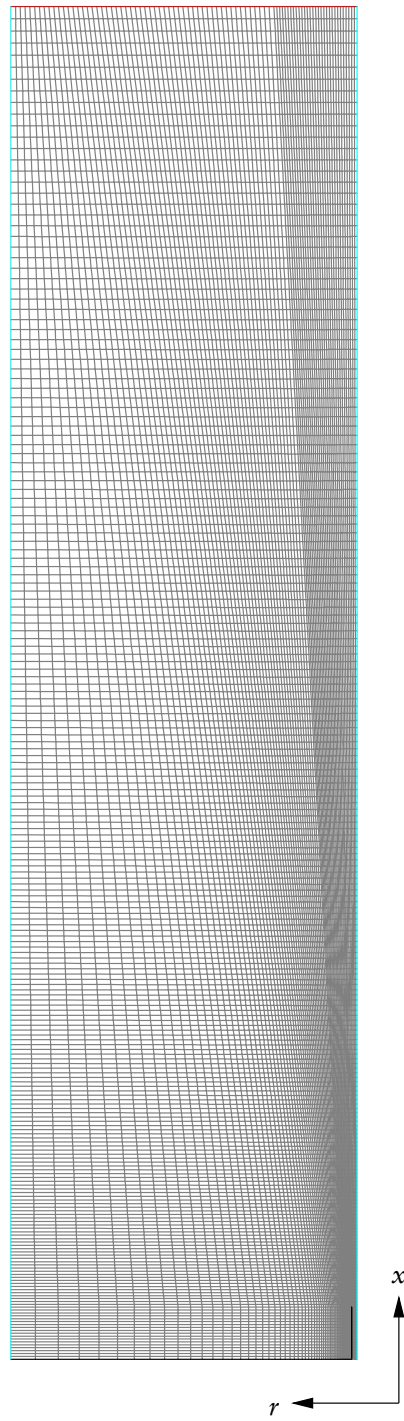
Figure 5.4: Computational mesh used for jet flame calculations.

Table 5.4: Model constants used in computations.

	σ_k	σ_ε	$C_{\varepsilon 1}$	$C_{\varepsilon 2}$	Sc_t	Pr_t	C_μ
Standard realizable k-ε [39]	1.0	1.2	Eq. (3.14)	1.9	0.7	0.85	Eq. (3.15)
Standard RS [97]	1.0	1.3	1.44	1.92	0.7	0.85	0.09
Altered realizable k-ε	1.0	1.2	Eq. (3.14)	1.8	0.775	0.85	Eq. (3.15)
Altered RS	1.0	1.3	1.44	1.8	0.7	0.85	0.09
RS used by Gran [46]	1.0	1.3	1.44	1.92	0.7	0.7	0.065

5.5 Results and Discussion

This section gives the results of CFD calculations using the reduced 6-step mechanism as described above. Flow and scalar field comparisons are made to experimental and computational results for both the target flames.

5.5.1 Bluff-Body Flame

5.5.1.1 Flow Field Comparison

In a bluff-body flame, stabilization occurs in the recirculation region downstream of the bluff-body. It is important that the position, size and strength of this recirculation zone be accurately captured to ensure the correct mixing of fuel and oxidizer streams. The flow pattern in this region for Cases A, B and C (see Table 5.1) obtained using standard model constants (Table 5.4) are shown in Figure 5.5 as streamlines. The flow pattern in Case D is observed to be similar to that in Case C, Figure 5.5b, and thus, it is not shown. The right side of Figure 5.5b shows data taken from Gran [46] using the RS closure with a presumed β-PDF model for mixture fractions and fast chemistry model for combustion.
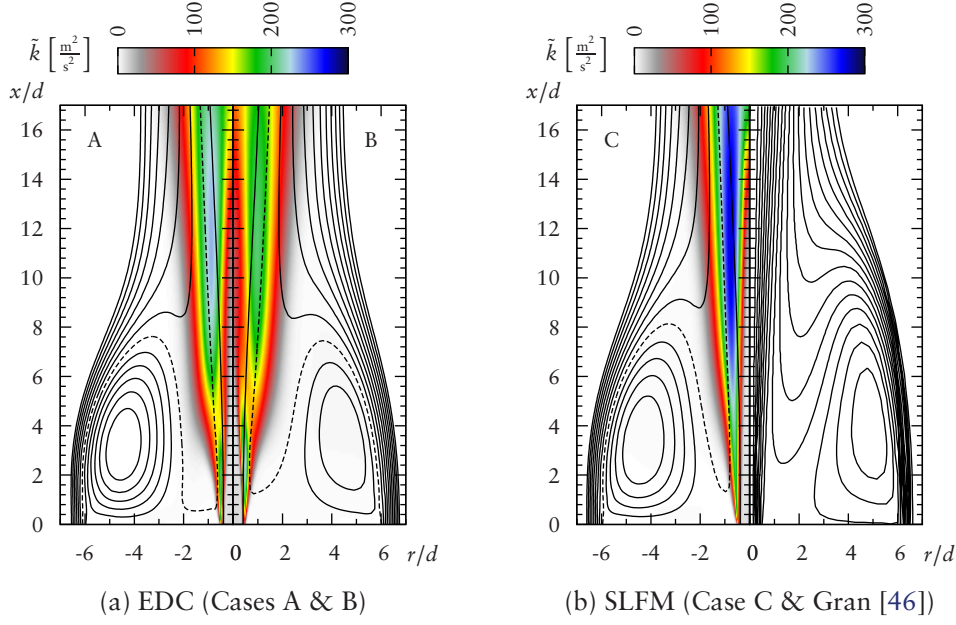
Figure 5.5: Streamlines behind the bluff-body which extends from $r/d = 0.5$ to $r/d = 6$. The predicted turbulent kinetic energy, $\tilde{k}$, is also shown as a colour-map. The right side of (b) shows RS closure results of Gran [46]. Case D (not shown) gives results similar to Case C. Dashed line indicates path-line of air to fuel inlet.

By comparing Figure 5.5a and 5.5b, it seems that the recirculation zone in the current predictions is less skewed and more compact than the somewhat elliptical shape predicted by Gran [46]. The length of the recirculation zone is observed to be about $9d$ in the current calculations using the realizable k-ε and RS closures, whereas the data of Gran [46] shows a longer recirculation zone, about $11d$. The current predictions also show that the streamlines at $x/d \approx 16$ are roughly parallel and aligned with the x-axis indicating the flow is developed, whereas the data of Gran [46] shows that the flow is still developing at this location. This implies that the current predictions are less diffusive. The influence of the combustion model on the length of the recirculation zone is observed to be small. By comparing Case A and Case C only a small ($\approx 0.5d$) difference in recirculation zone length is observed between the EDC and SLFM predictions. Cases A and C suggest that the recirculation region extends closer to the centreline in the re-

alizable k-ε closure than in the RS closure, shown in Figure 5.5a. It is also clear that the recirculation region introduces a mass flux from the air stream into the region where the flame anchors. This is highlighted by the dashed streamline in Figure 5.5 for Cases A–C. This mass flux can influence the predicted temperature field by introducing colder gas to the hot region, as will be discussed later. As one would expect, the RS closure shows a greater strain rate which is indicated in the near-field region by closely spaced streamlines at $r/d > |6|$.

The variation of turbulent kinetic energy, $\tilde{k}$, is also shown in Figure 5.5 for Cases A–C. The variation in Case D is observed to be similar to that in Case C, shown in Figure 5.5b, thus, it is not shown. Comparing Cases A and B it seems that the realizable k-ε and RS closures predict similar spatial variation of $\tilde{k}$, except for its peak value and its location. The RS closure predicts a peak value further downstream than the realizable k-ε closure; compare Cases A and B shown in Figure 5.5a. This difference is due to the anisotropy of the flow, which creates an anisotropic production of $\tilde{k}$. One can expect these differences, given the complex nature of the flow.

Although the combustion submodels do not significantly influence the flow pattern, their influence on the turbulent kinetic energy prediction is observed to be large. Cases A and C, shown on the left half of Figure 5.5a and 5.5b, use the realizable k-ε closure for turbulence with the EDC and SLFM, respectively. By comparing these two cases one can clearly observe that the turbulent kinetic energy predicted by the SLFM is about 25% larger than in the calculation with the EDC. Also, the EDC gives two distinct regions with large values of $\tilde{k}$, whereas the SLFM gives monotonic variation as in Figure 5.5b. It is important to note that the results obtained using the RS turbulence closure with the EDC, shown on the right half of Figure 5.5a, also depict two regions having large $\tilde{k}$ values. This difference could be due to the separation of mixing and kinetics, which is implicit in the SLFM approach, whereas the EDC maintains a closer coupling, particu-

(a) EDC (Cases A & B)

(b) SLFM (Cases C & D)
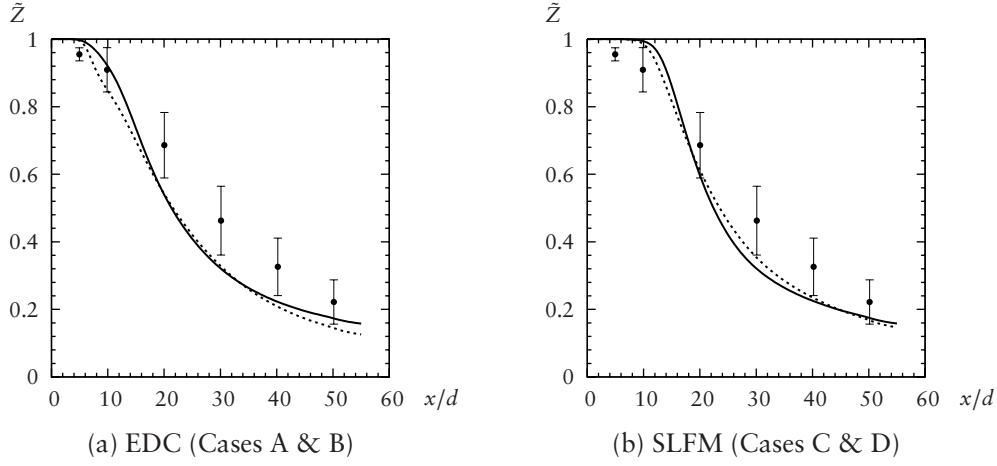
Figure 5.6: Centreline variation of mixture fraction, $\tilde{Z}$, for the bluff-body flame:
• experimental data [28], ——realizable k-ε model and ····RS model predictions with 6-step reduced mechanism. The width of the error bars denotes two standard deviations of the mixture fraction fluctuation.

larly between $\bar{\rho}$ and $\tilde{k}$ via Equations (3.46) and (3.47). The influence of the secondary high-$\tilde{k}$ region on the location of flame stabilization will be discussed later.

Figure 5.6 shows axial profiles of the mean mixture fraction, $\tilde{Z}$, for all cases. For the results shown in Figure 5.6a, which are obtained using the EDC, values of $\tilde{Z}$ are reconstructed from the mean species mass fractions, $\tilde{Y}_\alpha$, following Warnatz et al. [114]. In the calculations using the SLFM a transport equation for $\tilde{Z}$ is solved. Both the realizable k-ε and the RS closures with standard model constants, given in Table 5.4, yield relatively poor predictions; both of these closures over-predict the rate of mixing compared to experiment and, hence, they give a faster decay of $\tilde{Z}$. A difference between the EDC and the SLFM is seen in the near-field region; compare Figures 5.6a and 5.6b. The potential core calculated using the EDC is about half the length calculated using the SLFM, where the initial decay in $\tilde{Z}$ occurs at $x/d \approx 10$. This is probably due to preferential diffusion effects included in the EDC calculations; the light H_2 diffuses quickly away from the fuel stream, thus decreasing $\tilde{Z}$. As noted earlier, full multi-component transport is in-

cluded in the calculations with the EDC since the importance of differential diffusion on flame stabilization is noted in an earlier study [4]. As the fuel considered in this work can have a high proportion of H_2, differential diffusion effects could be important to capture stabilization in turbulent flames. In addition, the assumption of constant Lewis numbers in the SLFM may not be acceptable when species with largely differing molecular weights are present, such as H_2 and CO in the fuel stream. An accurate mixture fraction prediction is important if the resulting scalar fields are to be correct, as will be discussed later.

In the present study, the realizable k-ε closure with the EDC is able to predict the flow without experiencing blow-off, unlike previously reported results using the standard k-ε closure [48]. This is likely to be due to the more accurate prediction of the physical attributes of the recirculation zone, thus giving the correct mixing of the fuel, air and hot product streams. Standard model constants, given in Table 5.4, are used for the current calculations. However, for the RS closure, modifications to the model constants made in Gran and Magnussen [47] could not be tested as blow-off occurred. The reason for this behaviour is unclear and it may, perhaps, be due to different numerical implementations of the models in their work [47].

5.5.1.2   Scalar Field Comparison

The predicted mean OH mass fraction and temperature fields for all cases obtained using standard model constants are shown in Figure 5.7. Qualitatively, the predictions using the EDC with the realizable k-ε and RS turbulence closures (Cases A and B) are very similar. The same observation is made for the SLFM (Cases C and D). The influence of the combustion submodels is observed to be large. Cases A and C use the realizable k-ε closure and the EDC and SLFM, respectively. By comparing the temperature field for these two cases (shown on the left side of Figures 5.7a and 5.7c) one can clearly observe

the difference in locations of flame stabilization. The SLFM predicts an attached flame, whereas the EDC predicts a lifted flame stabilizing at $x/d \approx 2$. A similar observation is made using the RS turbulence closure (Cases B and D) by comparing the left sides of Figures 5.7b and 5.7d. The predicted $\tilde{Y}_{OH}$ fields (shown on the right side of Figures 5.7a–5.7d) follow the $\tilde{T}$ fields closely, but are more pronounced.

Predictions of the EDC with the realizable k-ε closure show an initial temperature rise slightly closer to the bluff-body than the RS closure; compare the left sides of Figures 5.7a and 5.7b at $x/d < 2$. The region of higher temperature observed in the realizable k-ε closure (Case A) implies that there is a weaker recirculation of the cold air stream to the flame base than that predicted with the RS closure, where the predicted temperatures are lower in the same region. The location of the maximum temperature region is predicted at a similar location for Cases A and B; $x/d \approx 3.6$. Case B shows a larger high temperature region than Case A. Comparing the turbulence closure methods for the SLFM (Cases C and D) shows little difference in temperature fields. Comparing the combustion submodels using the realizable k-ε closure one can clearly see that the EDC approach predicts higher peak temperatures ($\tilde{T} \approx 1800$ K) than the SLFM ($\tilde{T} \approx 1500$ K); compare Cases A and C. A similar observation is made for the RS closure.

Predictions of $\tilde{Y}_{OH}$ using the EDC and the realizable k-ε closure show slightly lower peak values ($\tilde{Y}_{OH} \approx 0.0038$) at the downstream extent than for Case B ($\tilde{Y}_{OH} \approx 0.0042$) using the RS closure; shown in the right side of Figures 5.7a and 5.7b, respectively. The same comparison for the SLFM shows that both turbulence closures give very similar predictions. By comparing the combustion submodels a clear difference is again seen. The EDC predicts higher values of $\tilde{Y}_{OH}$ (Cases A and B) than the SLFM (Cases C and D). In addition, the SLFM shows a greater spread of $\tilde{Y}_{OH}$ than the EDC. The major difference between flame stabilization locations predicted by the EDC and SLFM could
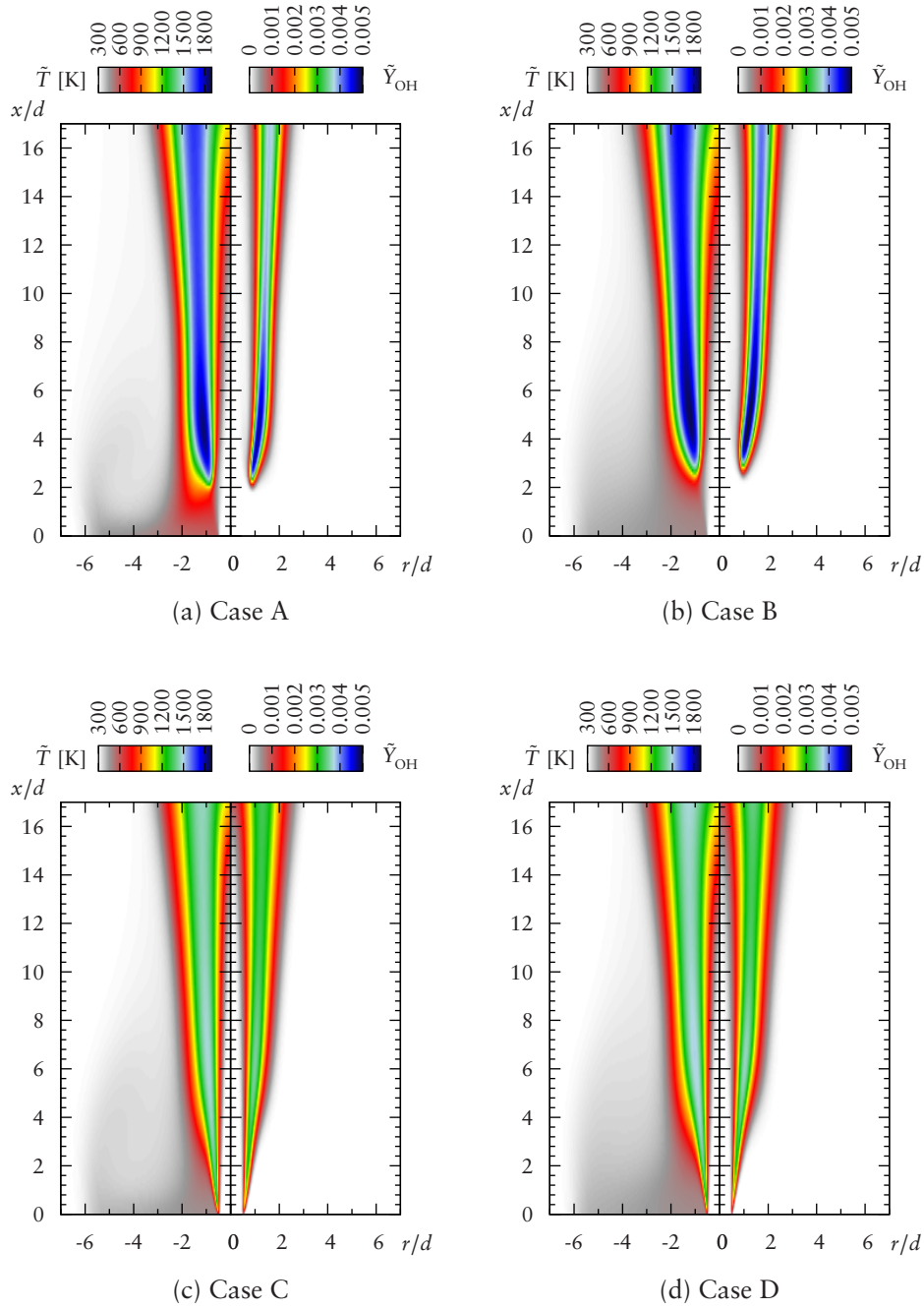
Figure 5.7: Contours of predicted temperature and OH mass fractions for the bluff-body flame; the bluff-body extends from $r/d = 0.5$ to $r/d = 6$. (a) and (b) are for the EDC, (c) and (d) are for the SLFM.

be explained by the lack of an extinguished flamelet in the library used in the SLFM or an incorrect prediction of the mixture fraction variance in the highly-strained region at the nozzle outlet. The EDC model could be affected by the turbulence field in the near-nozzle region. A comparison of the $\tilde{Y}_{OH}$ fields to the $\tilde{k}$ fields given in Figure 5.5 shows that the SLFM gives a consistent pattern in values. The EDC predicts an increase in $\tilde{Y}_{OH}$ (and hence temperature) just downstream of the initial peak in $\tilde{k}$. This initial peak could act as a trigger for the reaction through Equations (3.47) and (3.46). Unfortunately, experimental evidence is not available for this flame to compare where the flame stabilization actually occurs.

The effect of turbulence closures using the EDC approach is shown in Figure 5.8. Radial profiles of major species mean mass fractions, $\tilde{Y}_{\alpha}$, mean mixture fraction, $\tilde{Z}$, and mean temperature, $\tilde{T}$, calculated for Cases A and B at two downstream locations ($x/d = 10$ and $x/d = 20$) are given. Comparison is made with experimental results [28]. In general, the effect of the incorrect prediction of the mixing field at $x/d = 20$ can be seen in Figures 5.8a, 5.8c and 5.8e whereby it affects the products of the reaction and the flame temperature. Small differences exist between the predictions using the realizable k-ε and RS closures. The RS closure suggests slightly enhanced radial diffusion as in Figures 5.8a, 5.8c and 5.8e. The present work over-predicts the reported value of $\tilde{Y}_{CO_2}$ by nearly 100%. It is surprising to note that comparison to the previous simulations using the EDC with detailed chemistry was not possible due to the lack of published computational data [48]. However, previous results using simplified chemistry and the transported-PDF model also show a large ($\approx 100\%$) departure from the experimental values [29]. Indeed, the presented results for $\tilde{Y}_{CO_2}$ are in general agreement with those reported by Correa and Pope [29]. This suggests that the experimental data may be inaccurate, as it is known that measuring CO_2 using the Raman method is difficult [28]. However, it can be seen that the RS closure predicts a higher peak value compared to
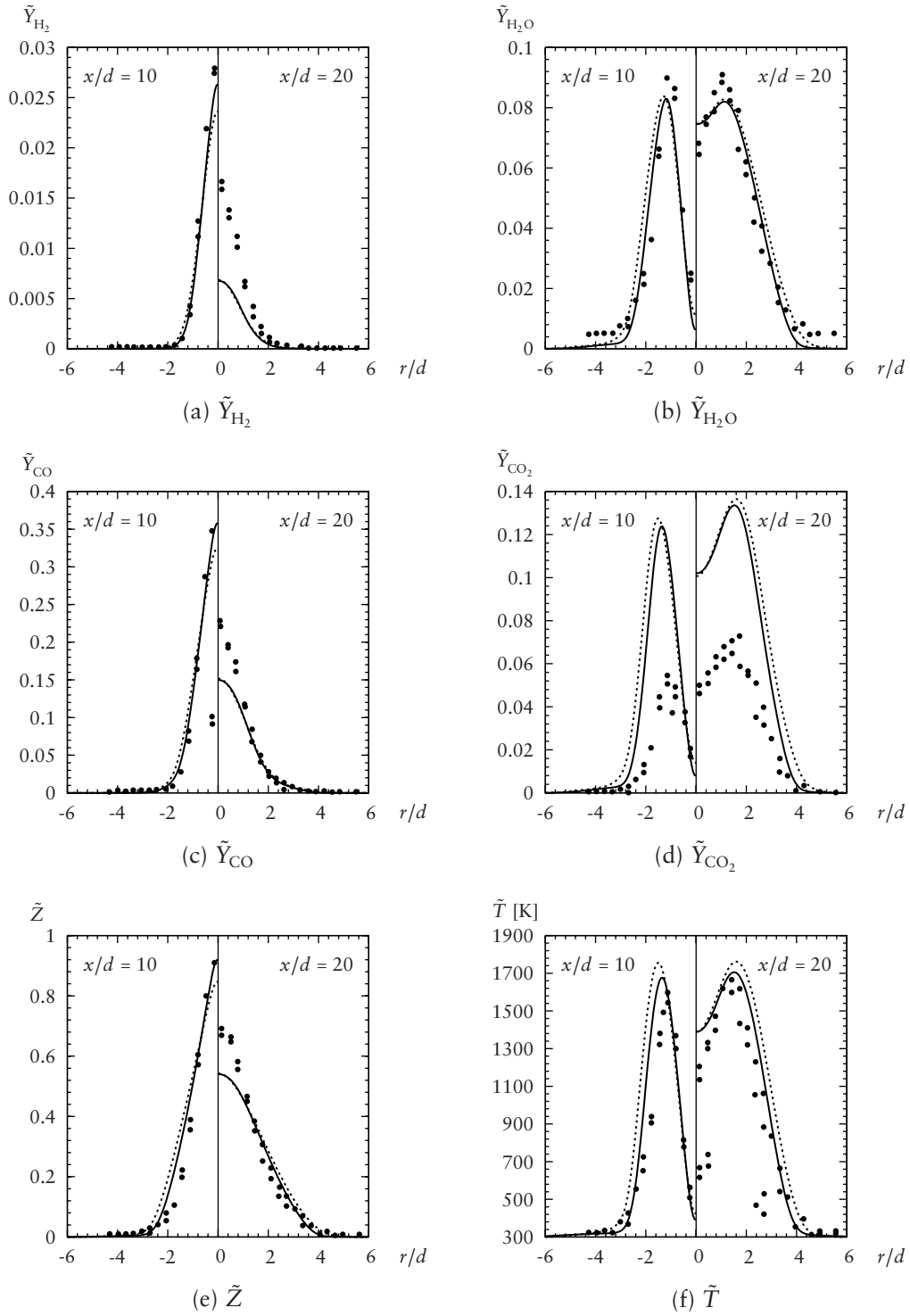
(a) $\tilde{Y}_{H_2}$

(b) $\tilde{Y}_{H_2O}$

(c) $\tilde{Y}_{CO}$

(d) $\tilde{Y}_{CO_2}$

(e) $\tilde{Z}$

(f) $\tilde{T}$

Figure 5.8: Radial profiles of mass fractions, $\tilde{Y}_\alpha$, mixture fraction, $\tilde{Z}$, and temperature, $\tilde{T}$, using the EDC (Cases A & B) for the bluff-body flame at two downstream locations: • experimental data [28], ——realizable k-ε model and $\cdots\cdots$ RS model predictions with 6-step reduced mechanism.

the realizable k-ε closure; consistent with a higher rate of reaction.

Differences between turbulence closures become apparent by viewing the peak radial temperatures, Figure 5.8f. The realizable k-ε closure gives a slightly better prediction than the RS closure at both locations relative to experiments. At x/d = 10 the realizable k-ε and RS closures over-predict by 10% and 15%, respectively. At downstream locations, the difference is lower but still significant; 4% and 8%. These differences can again be attributed to variations in mixing, and hence reaction. In addition, the lack of heat loss due to radiation in the simulations necessarily results in an over prediction of temperature. It is known that the temperature can decrease due to radiation of H_2O and CO_2 by about 50 K in these flames [5].

5.5.2   Jet Flame

5.5.2.1   Flow Field Comparison

For a simple jet flame, stabilization usually occurs very close to the fuel nozzle, if not anchored on the nozzle surface. Stabilization is helped by radiative heat transfer from the flame to the fuel pipe; either acting to pre-heat the fuel stream or providing a hot region to anchor the flame. As large regions of recirculation are not present in jet flames, the region downstream of the nozzle does not need to be resolved as highly as in the bluff-body flame. The flow pattern downstream of the nozzle for all cases (see Table 5.1) obtained using standard model constants (Table 5.4) is shown in Figure 5.9 as stream-lines. The influence of the combustion model on the flow acceleration is observed to be small. By comparing Cases A and C using the realizable k-ε closure (the left side of Figures 5.9a and 5.9b, respectively) a small ($\approx 0.6r/d$) difference in streamline contraction is observed at x/d = 20 between the EDC and SLFM predictions. A similar observation is made for Cases B and D using the RS closure (the right side of Figures 5.9a and 5.9b,

(a) EDC (Cases A & B)　　　　　(b) SLFM (Cases C & D)
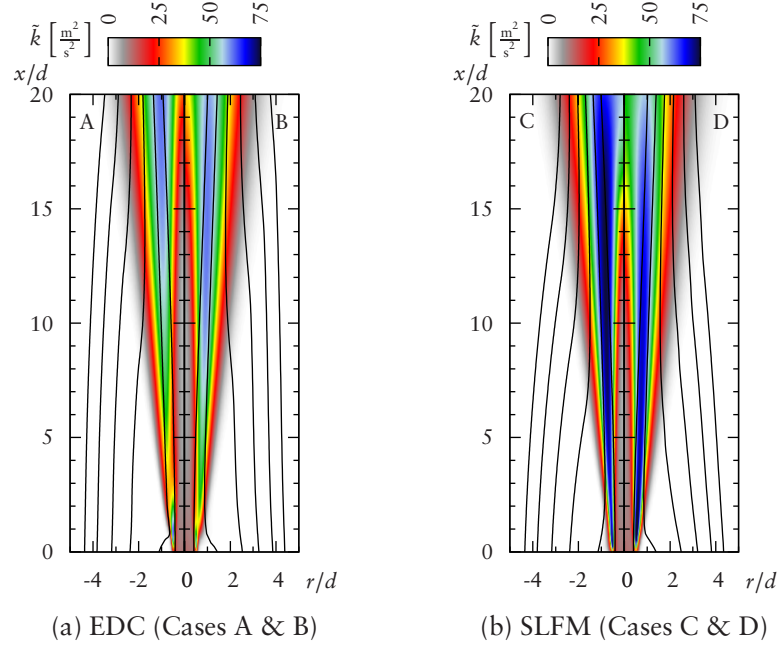
Figure 5.9: Streamlines downstream of the jet inlet. The predicted turbulent kinetic energy, $\tilde{k}$, is also shown as a colour-map.

respectively). The influence of the turbulence closure is also observed to be small by comparing the left and right sides of Figures 5.9a and 5.9b for the EDC and SLFM, respectively.

The variation of turbulent kinetic energy, $\tilde{k}$, is also shown in Figure 5.9 for all cases. As with the bluff-body flame, the realizable k-ε and RS closures give similar spatial variation in all but the near-field. The peak $\tilde{k}$ location is closer to the nozzle with the RS closure than the realizable k-ε closure. The combustion submodels have only a small influence on the mean flow pattern but their influence on maximum $\tilde{k}$ is observed to be large, as with the bluff-body flame. Comparing Cases A and C one can clearly observe that $\tilde{k}$ predicted by the SLFM is about 25% larger than the EDC predictions, which is consistent with the results for the bluff-body flame. Also, as with the bluff-body flame, the EDC gives two distinct regions with large $\tilde{k}$ values, whereas the SLFM gives monotonic variation as in Figure 5.9b. The predictions for Case B, with the RS closure,

(a) EDC (Cases A & B) (b) SLFM (Cases C & D)
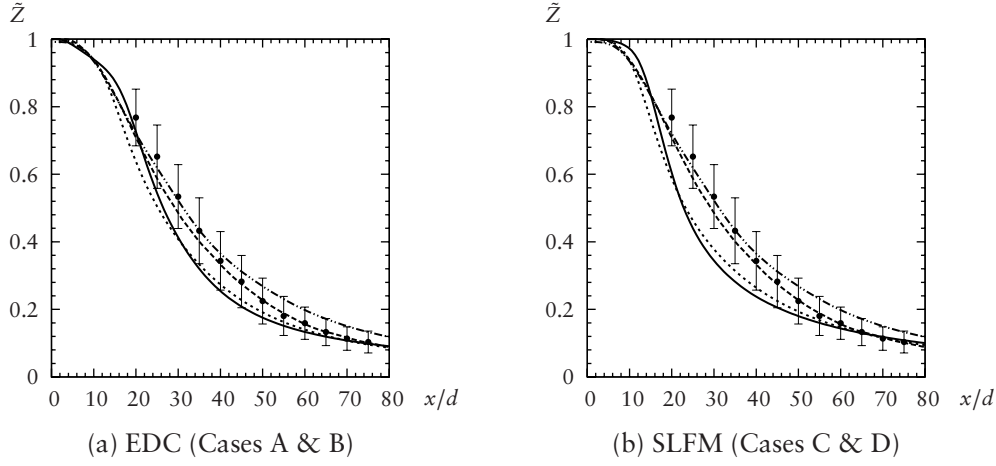
Figure 5.10: Centreline variation of mixture fraction, $\tilde{Z}$, for the jet flame: • experimental data [6], —— realizable k-ε model and ···· RS model with 6-step reduced mechanism. Also shown: —·· — CMC method [60] and - - - SLFM [62], both using the k-ε closure with Pope's correction [98]. The width of the error bars denote two standard deviations of the mixture fraction fluctuation.

also depict two distinct regions although the secondary region is smaller in size. As with the bluff-body flame, the difference could be due to the separation of mixing and kinetics in the SLFM. The influence of the secondary high-$\tilde{k}$ region on the location of flame stabilization will be discussed later.

Figure 5.10 shows axial profiles of the mean mixture fraction, $\tilde{Z}$, for all cases. Comparison is made to experimental values [4, 6] and other computational predictions using the SLFM [62] and CMC [60] approaches, both using the standard k-ε model with Pope's correction. As in the bluff-body flame, both turbulence closures over-predict the rate of mixing and hence they give a faster decay of $\tilde{Z}$. A difference between the EDC and SLFM is seen in the near-field; the potential core length calculated using the EDC is about half the length calculated with the SLFM, where the initial decay in $\tilde{Z}$ occurs at $x/d \approx 10$. This is probably due to preferential diffusion effects included in calculations with the EDC, as discussed in Section 5.5.1.1. The EDC gives a slightly better prediction of the centreline decay than the SLFM when the standard model constants are used.

The previous predictions, using Pope's correction [98] and an altered turbulent Schmidt number of 0.65 [60, 62], show excellent agreement to the experimental result.

5.5.2.2 Scalar Field Comparison

The predicted mean OH mass fraction and temperature fields for all cases obtained using standard model constants are shown in Figure 5.11. As for the bluff-body flame, the predictions using the EDC with the realizable k-ε and RS closures (Cases A and B) are very similar; this is also observed for the SLFM (Cases C and D). The influence of the combustion submodel is again observed to be large. Comparing the temperature field for Cases A and C (shown on the left side of Figures 5.11a and 5.11c) shows the SLFM to predict an attached flame, whereas the EDC predicts a lifted flame stabilizing at $x/d \approx 0.8$. Cases B and D, with the RS model, give a similar observation but with Case B stabilizing at $x/d \approx 0.5$. The ignition location is indicated by the $\tilde{Y}_{OH}$ field which follows closely that of $\tilde{T}$. Specific experimental data on the position of flame stabilization (photographic or otherwise) is unavailable. However, the flame is believed to be attached or stabilized within $x/d < 0.2$, as determined visually [3]. The discrepancy could be due to the mesh density in the shear layer between the two streams close to the nozzle. In addition, the assumption of an infinitely thin wall reduces the production of turbulent kinetic energy that would be present around the small recirculation region immediately downstream of the nozzle. As discussed, this would affect the values of $\tilde{k}$ and $\tilde{\varepsilon}$ and, thus, the reaction rate calculated with the EDC. As for the bluff-body flame, the initial increase in $\tilde{Y}_{OH}$ coincides with the secondary high-$\tilde{k}$ region shown in Figure 5.9. Finally, none of the models consider heat transfer from the flame to the fuel inlet pipe. It is known that the flame does not stabilize until the fuel pipe is suitably heated [3]. These experimental details are not included in the present adiabatic study, nor in any previous studies known to the author. Such heat transfer would be expected

Figure 5.11: Contours of predicted temperature and OH mass fractions for the jet flame. (a) and (b) are for the EDC, (c) and (d) are for the SLFM.

(a) EDC (Cases A & B)

(b) SLFM (Cases C & D)
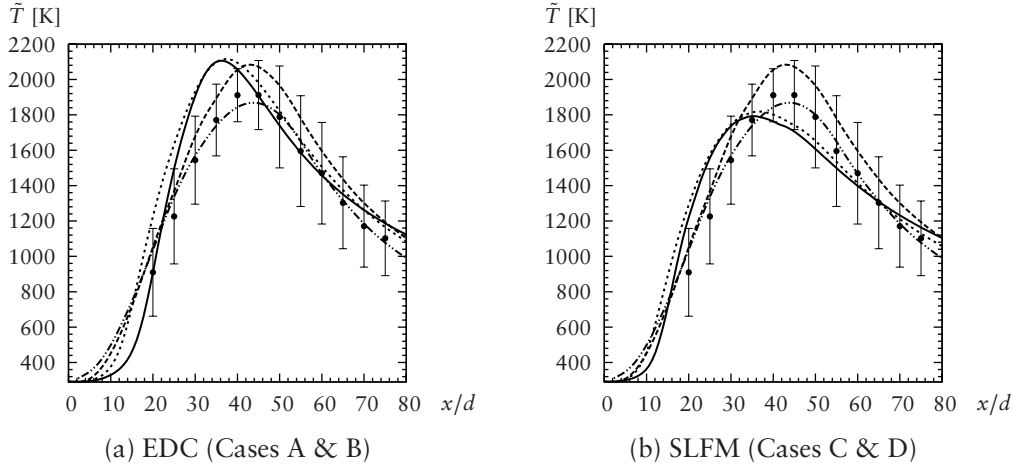
Figure 5.12: Centreline variation of mean temperature, $\tilde{T}$, along for the jet flame: • experimental data [6], ——realizable k-ε model and ···· RS model with 6-step reduced mechanism. Also shown: —··— CMC method [60] and --- SLFM [62], both using the k-ε closure with Pope's correction [98]. The width of the error bars denote two standard deviations of the temperature fluctuation.
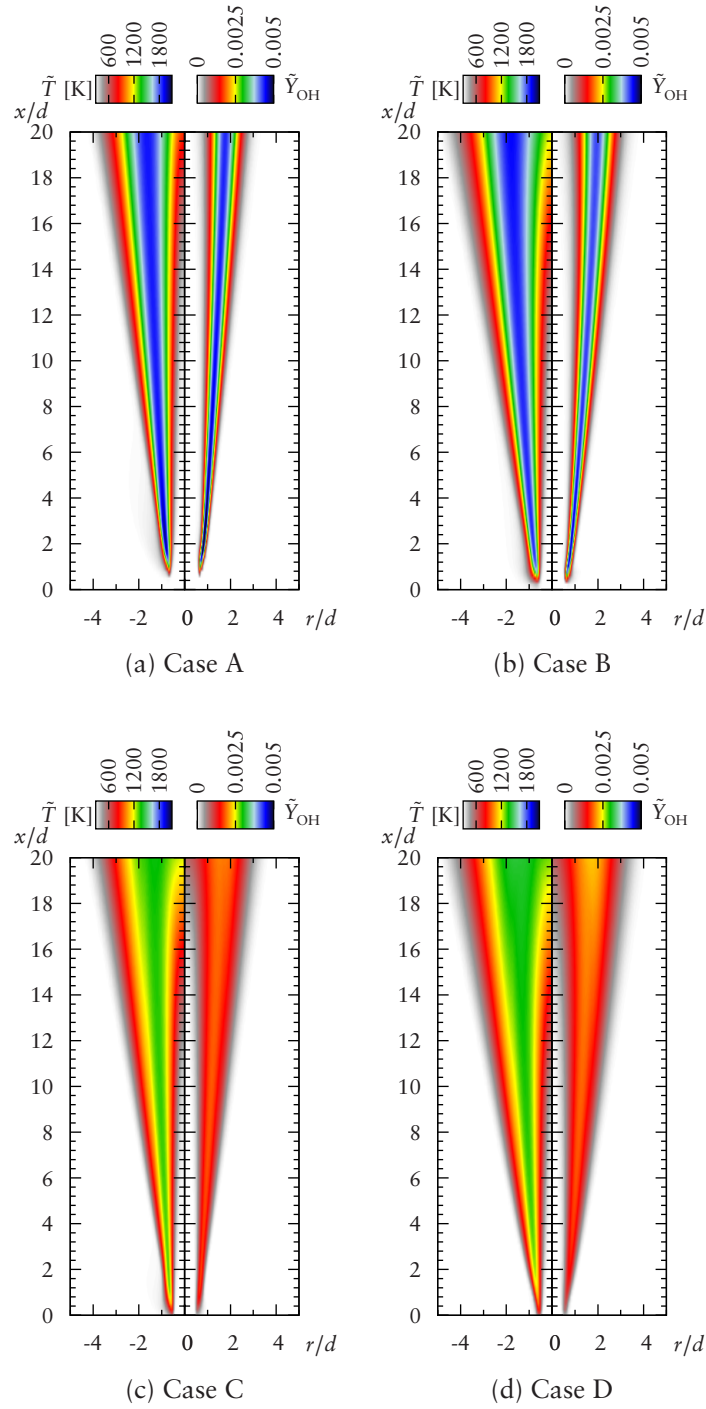
to reduce the lift-off height experienced with the EDC due to the increased temperature. The EDC predicts a higher temperature than the SLFM by about 100 K. The peak $\tilde{Y}_{OH}$ values predicted using the SLFM are about 50% lower than predicted with the EDC. The SLFM predicts a greater spread of OH than the EDC. Both these observations are likely to be due to the unity Lewis number assumption of the SLFM.

Figure 5.12 shows axial profiles of mean centreline temperature for all cases. Comparison is made to experimental values [6] and computational predictions using the SLFM [62] and CMC [60] approaches. Both the EDC and SLFM agree reasonably well with the measured temperature profile, although the peak temperature predicted by the EDC (2180 K) is significantly higher than the measured value of 1930 K; the SLFM gives 1800 K. The location of the predicted peak temperature ($x/d \approx 36$) is closer than the experimental location ($x/d \approx 42$). These differences can be attributed to the incorrect prediction of the mixing and mixture fraction field. For the EDC, the mixture fraction prediction indicates that there is increased mixing when compared to experiment. This

suggests that higher values of $\tilde{k}$ or $\tilde{\varepsilon}$ are being predicted which increases the reaction rate via Equations (3.47) and (3.46). Similarly, for the SLFM the incorrect prediction of $\tilde{Z}$, along with its variance, $\widetilde{Z''^2}$, can lead to the incorrect calculation of scalar dissipation, $\tilde{\chi}$. Subsequently, incorrect temperature and scalar values are obtained from the flamelet library. For both the EDC and SLFM, the location of the peak temperature coincides with the location of the largest deviation of predicted mixture fraction from the experimentally determined values, shown in Figure 5.10. The downstream values (x/d = 80) are in close agreement which further suggests the mixing rate is not correctly captured. There is a slight difference in temperature gradients between the predictions made with the realizable k-ε and the RS closures. With both the EDC and SLFM, the initial temperature rise is predicted earlier with the RS closure (Cases B and D), and the temperature takes longer to decrease from the peak value. The previous SLFM predictions [62] over-predict the peak temperature by a similar amount as with the current EDC predictions, as shown in Figure 5.12a.

Figure 5.13a shows axial profiles of $\tilde{Y}_{NO}$ for Cases A, B and C. Comparison is made to experiment [4, 6] and predictions made using the CMC approach [60]. Figure 5.13b shows axial profiles of NO mole fraction, $\tilde{X}_{NO}$ [ppm], for Cases A and B. Comparison is made to experiment [4, 6] and predictions made using the SLFM with a NO post-processing step [62]. The location of the peak values along the centreline for Cases A and B follows that of temperature (Figure 5.12a). The over-prediction of peak temperature is also seen to influence the prediction of $\tilde{Y}_{NO}$ and $\tilde{X}_{NO}$. However, the magnitude of predicted values is largely within 2σ of the experimental values, albeit shifted further upstream due to the incorrect mixing field. The values predicted for Case C (using the SLFM) are two orders of magnitude larger than experiment as indicated in Figure 5.13a. This highlights a known limitation of the SLFM in its steady formulation with respect to pollutant formation [62, 89]. A transient formulation of the flamelet model with

(a) Mass Fraction (Cases A, B & C)　　　(b) Concentration (Cases A & B)
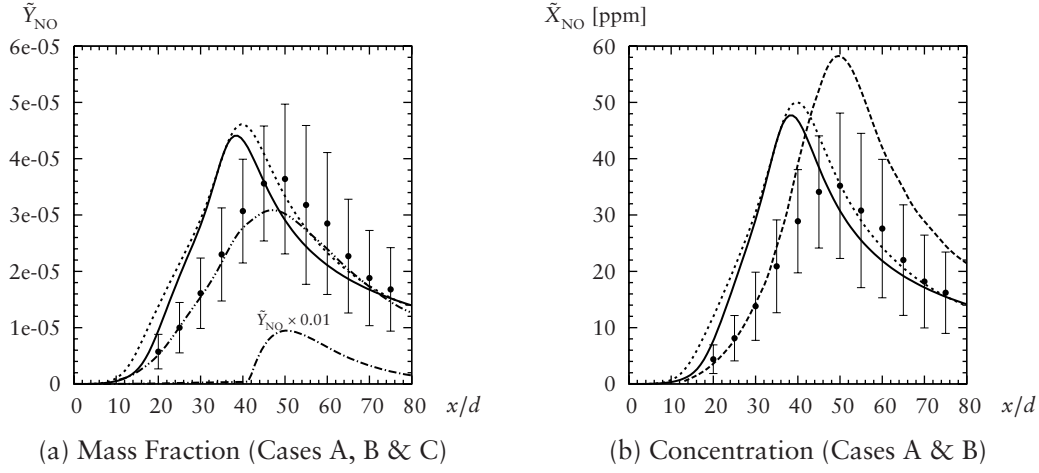
Figure 5.13: Centreline variation of NO mass fractions (a) and concentrations (b) for the jet flame: • experimental data [6], ——realizable k-ε model, ···· RS model, and —·— SLFM solution (Case C) with 6-step reduced mechanism. Also shown: —··— CMC method [60] and --- SLFM [62], both using the k-ε closure with Pope's correction [98]. The width of the error bars denote two standard deviations of the respective scalar fluctuation.

radiative heat loss seems to improve the NO predictions [62]. Further downstream at x/d = 50, where the temperature predictions are in agreement with experiment, the values for $\tilde{Y}_{NO}$ are in good general agreement with experiment. A slight difference between the predictions using the realizable k-ε and RS closures is seen. Again, this reflects the differences in temperature predictions. However, as NO predictions are highly sensitive to temperature, the differences are accentuated, particularly downstream of the peak value in Figure 5.13a. The recent CMC predictions [60] show excellent agreement to experiment as shown in Figure 5.13a. The previous SLFM predictions using a NO post-processing step [62] over-predict the peak mole fraction by ≈ 23 ppm, compared to the current EDC predictions (≈ 15 ppm), as shown in Figure 5.13b.

A comparison of turbulence closures using the EDC approach is shown in Figure 5.14. Radial profiles for Cases A and B at two downstream locations (x/d = 20 and x/d = 50) are given. Comparison is made with experimental results [4, 6]. For H_2 and CO comparison is made at x/d = 20 and x/d = 30 due to the low values measured
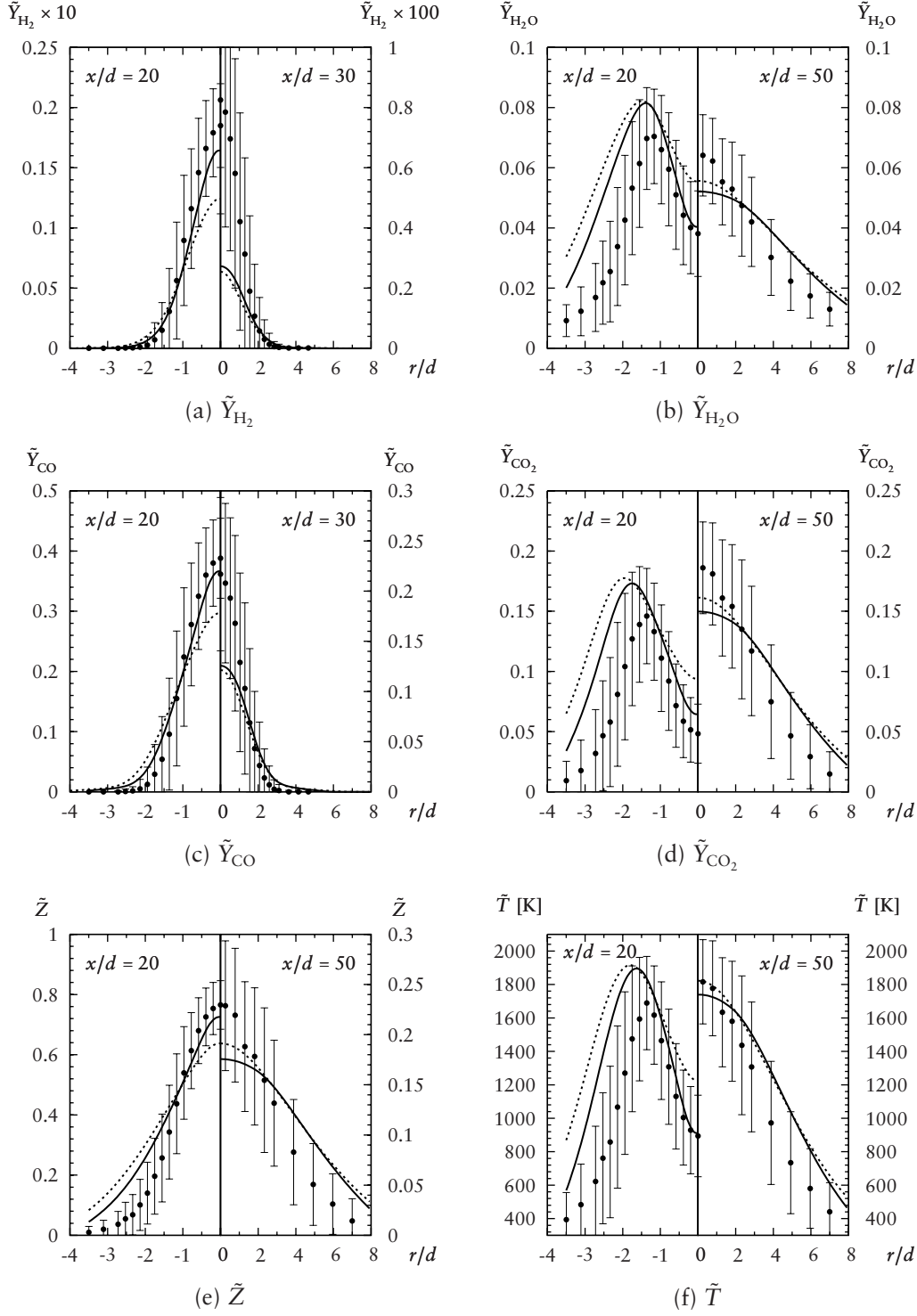
Figure 5.14: Radial profiles of mass fractions, $\tilde{Y}_\alpha$, mixture fraction, $\tilde{Z}$, and temperature, $\tilde{T}$, using the EDC (Cases A and B) for the jet flame at two downstream locations: ● experimental data [6], —realizable k-ε model and ···· RS model with 6-step reduced mechanism. The width of the error bars denote two standard deviations of the respective scalar fluctuation.

and predicted at x/d = 50. As in the bluff-body flame, some deviation exists due to the variation in mixture fraction field, as can be seen in Figures 5.14a, 5.14c and 5.14e; in particular at the downstream locations. Greater mixing and spreading of the jet is observed; particularly notable in Figure 5.8e. The over-predicted mixing also affects the products of the reaction and the flame temperature through the incorrect prediction of $\tilde{k}$ and $\tilde{\varepsilon}$. Small differences exist between the predictions using the realizable k-ε and RS closures. The centreline values at x/d = 20 are under-predicted using the RS closure as seen in Figures 5.14a and 5.14c, with a similar deviation seen in Figure 5.14e. Comparison of predicted CO_2 values to experimental results gives good agreement, unlike the bluff-body flame (Figure 5.8d). A similar peak temperature (shown in Figure 5.8f) is predicted at x/d = 20 using the realizable k-ε and RS closures; however, the RS closure gives a differing location. At x/d = 50 the differences are less pronounced. The differences seen can again be attributed to variations in mixing, and hence reaction. In addition, taking account of heat loss due to radiation would be expected to cause a further decrease in peak temperatures [5].

These observations, discussed above, all lend confidence to the presented method of coupling the reduced 6-step mechanism to the CFD code, using the less computationally intensive realizable k-ε turbulence closure. For parametric studies, the EDC negates the need for specific flamelet libraries to be generated, as required for the SLFM, which would be advantageous for industrial design optimization.

5.6 Sensitivity to Model Constants

In the previous sections, it has been shown that the mixing fields calculated using the realizable k-ε and RS closures, using standard model constants, with both the EDC and SLFM differ somewhat from those measured experimentally. If an un-characterized

combusting flow, such as a novel combustor configuration, is under design then this is the accuracy that can be expected for turbulent flames. However, as is customary in turbulent combustion, some adjustment of the model constants is acceptable to facilitate more accurate predictions. Where no experimental data for comparative purposes exists, one must accept the accuracy demonstrated in the preceding sections. To demonstrate that the models used in the present study can give more accurate predictions, the generally accepted values for turbulence parameters and constants are altered for the bluff-body and jet flames using the EDC and realizable k-ε turbulence closure (Case A). The axial profile of mean mixture fraction, $\tilde{Z}$, is used to compare with experiment as the mixture fraction reflects the effect of turbulence and, thus, kinetics for the EDC.

The constants C_2 in the realizable k-ε turbulence closure, Equation (3.13), and Sc_t in the species transport equation, Equation (3.24), are varied. The constant C_2 controls the destruction of $\tilde{\varepsilon}$ and, thus, the spreading of the solutions. This constant only alters the realizable k-ε model equation for $\tilde{\varepsilon}$ and isn't affected by other modelling approaches, such as for μ_t, unlike σ_ε. Sc_t controls the turbulent species diffusion. The two constants are altered independently to observe the impact on the centreline mixture fraction profiles.

Figure 5.15 shows the effects of the variation of C_2 and Sc_t for the bluff-body flame. The value of C_2 is decreased from its standard value (Table 5.4) by $\approx 2.6\%$ and $\approx 5.2\%$, with the centreline profile of $\tilde{Z}$ given in Figure 5.15a. As the value of C_2 is decreased the decay of the centreline $\tilde{Z}$ is decreased as the solution becomes less dissipative, as expected. The value of Sc_t is increased from its standard value by $\approx 11\%$ and $\approx 21\%$, with the centreline profile of $\tilde{Z}$ given in Figure 5.15b. As the value of Sc_t is increased the decay of $\tilde{Z}$ decreases as the fuel species diffuse slower. The bluff-body flame is more complex than a jet flame. The values of these constants are also expected to alter the size and shape of the recirculation zone which, as discussed in Section 5.5.1, are important
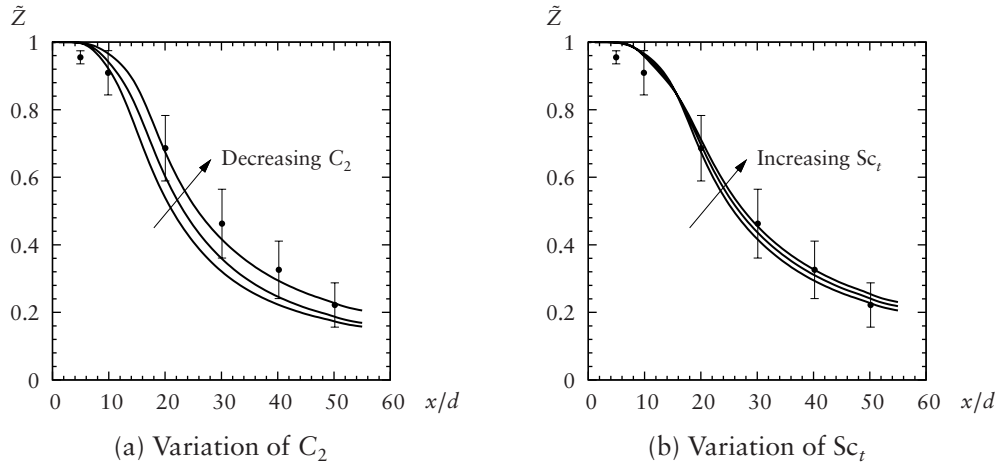
Figure 5.15: Graphs showing effects of model constant variation on centreline variation of mixture fraction, $\tilde{Z}$, for the bluff-body flame using the realizable k-ε turbulence closure. (a) shows predictions made with C_2 = 1.9, 1.85, 1.8 and Sc_t = 0.7. (b) shows predictions made with Sc_t = 0.7, 0.775, 0.85 and C_2 = 1.8.

for the correct prediction of the flame stabilization location.

Similar alterations of the model constants is applied to the jet flame, shown in Figure 5.16. The values of C_2 are altered by the same amount as described above, with the centreline profiles of $\tilde{Z}$ given in Figure 5.16a. In addition, the effect of the change of C_2 on $\tilde{T}$ and $\tilde{X}_{NO}$ is given in Figure 5.17. As with the bluff-body flame, a decrease in C_2 results in a decrease in dissipation as seen by the slower decay of $\tilde{Z}$ in Figure 5.16a. A slight increase in the peak $\tilde{T}$ values, as well as a variation in the location of the peak, with decreasing C_2 is seen in Figure 5.17a. These two observations are also shown in the centreline $\tilde{X}_{NO}$ profiles in Figure 5.17b, but with the effect of higher temperatures clearly visible. The increase in flame length, indicated by the peak temperature location, with decreasing C_2 is consistent with a decrease in dissipation and reduction in the spreading of the jet. The small increase in peak temperature is likely to be due to the reduced spreading of the hot products into the cold oxidizer cold flow. The values of Sc_t are increased by $\approx 11\%$ and decreased by $\approx 7\%$ with the centreline profiles given in

(a) Variation of C_2
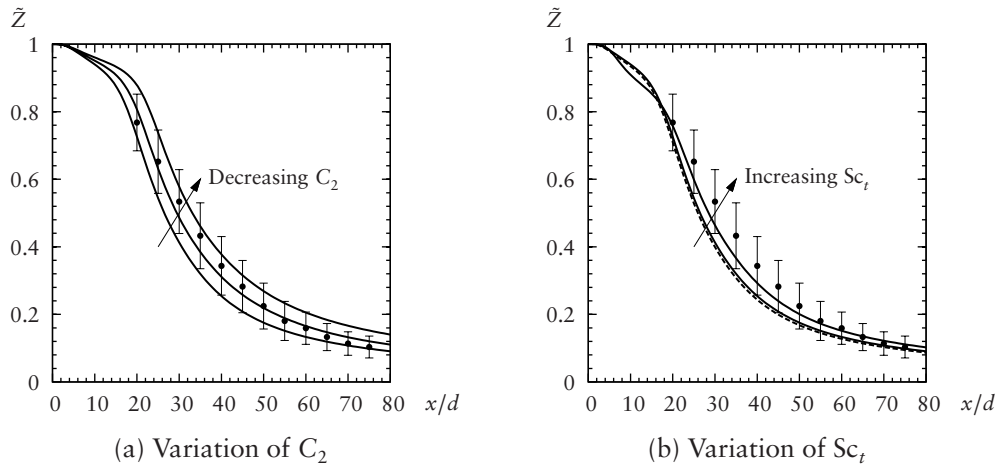
(b) Variation of Sc_t

Figure 5.16: Graphs showing effects of model constant variation on centreline variation of mixture fraction, $\tilde{Z}$, for the jet flame using the realizable k-ε turbulence closure. (a) shows predictions made with C_2 = 1.9, 1.85, 1.8 and Sc_t = 0.7. (b) shows predictions made with Sc_t = 0.65, 0.7, 0.775 and C_2 = 1.9; dashed line indicates Sc_t = 0.65 predictions for clarity.

Figures 5.16b and 5.18. As with the bluff-body flame, less sensitivity to Sc_t than C_2 is seen. A decrease in Sc_t increases the rate of decay of $\tilde{Z}$ and lowers the peak $\tilde{T}$ and $\tilde{X}_{NO}$ values; consistent with increase diffusion. A decrease in Sc_t reverses this trend.

For the bluff-body flame a combination of C_2 and Sc_t alterations for the realizable k-ε turbulence closure are used to improve the predictions, as shown in Table 5.4. The RS model is also used with altered constants. A small reduction ($\approx 6\%$), obtained iteratively, in the values of $C_{\varepsilon 2}$ and C_2 in the RS and realizable k-ε closures, respectively, is used. The turbulent Schmidt number is increased by $\approx 11\%$, reducing mass diffusion.

Figure 5.19 shows the centreline profile of the mean mixture fraction for Cases A and B calculated using altered constants, given in Table 5.4. Comparison is made between the experimental values [28] and computational predictions [48]. The results using the RS closure show excellent agreement with experiment in all but the near-field region (x/d < 10). The much simpler realizable k-ε closure still shows good agreement. Although the current predictions for the $\tilde{Z}$ profile using the RS closure gives a better result
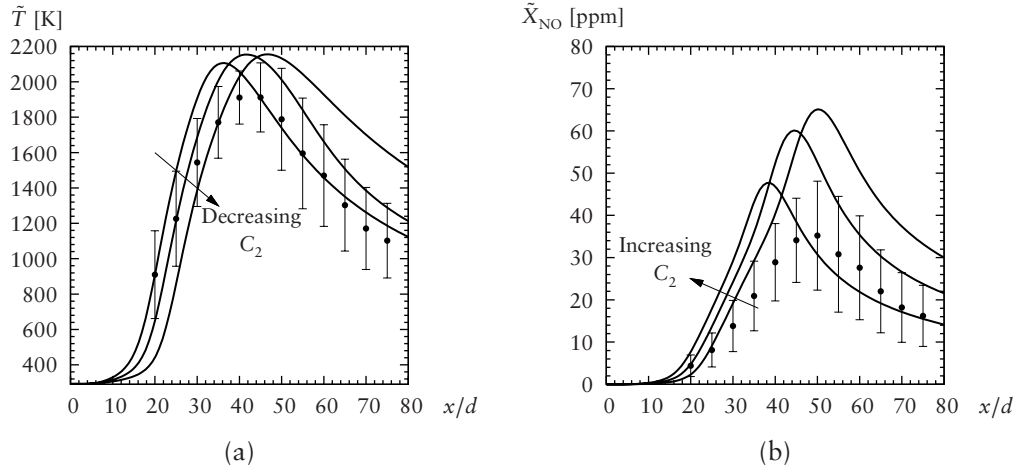
Figure 5.17: Graphs showing effects of variation of model constant C_2 on centreline profiles of temperature, $\tilde{T}$, and $\tilde{X}_{NO}$ for the jet flame using the realizable k-ε turbulence closure. Predictions made with C_2 = 1.9, 1.85, 1.8 and Sc_t = 0.7.
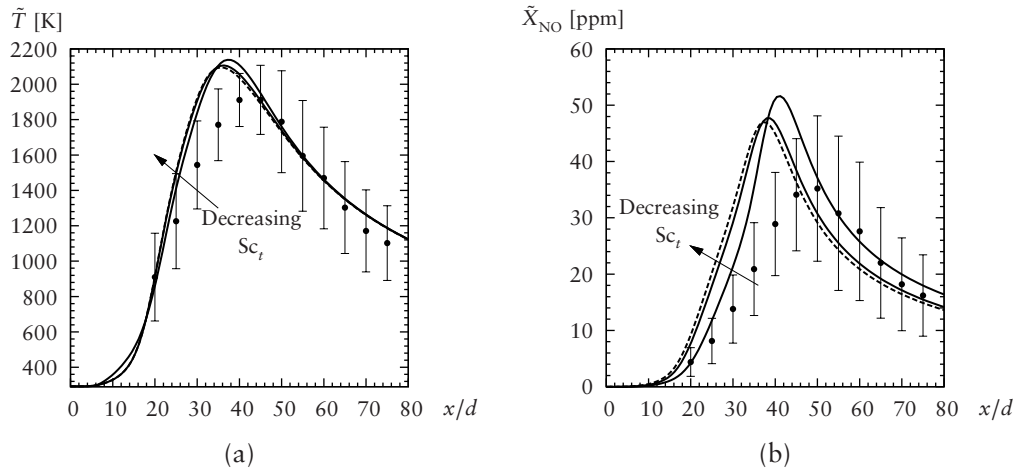
Figure 5.18: Graphs showing effects of variation of model constant Sc_t on centreline profiles of temperature, $\tilde{T}$, and $\tilde{X}_{NO}$ for the jet flame using the realizable k-ε turbulence closure. Predictions made with Sc_t = 0.65, 0.7, 0.85 and C_2 = 1.9. Dashed line indicates Sc_t = 0.65 predictions for clarity.
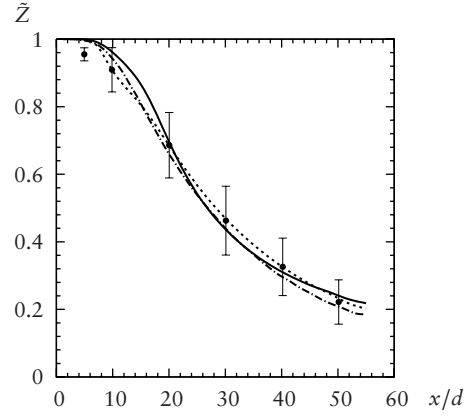
Figure 5.19: Centreline variation of mixture fraction, $\tilde{Z}$, for the bluff body flame using the EDC (Cases A & B) with altered constants: • experimental data [28], ——realizable k-ε and ···· RS closure predictions with 6-step reduced mechanism. Also shown: —·— computational data [48] using the RS closure and detailed kinetics [72]. The width of the error bars denotes two standard deviations of the mixture fraction fluctuation.

than the realizable k-ε closure, the realizable k-ε closure gives an acceptable match using fewer scalars resulting in faster computation times.

If the $\tilde{Z}$ field, constructed from the mass fractions of the participating species, is correct, then it follows that the mass fractions are in agreement. Figure 5.20 shows the radial profiles at two downstream locations; $x/d = 10$ and $x/d = 20$. In general, very little deviation in the predictions of $\tilde{Y}_{\alpha}$ and $\tilde{Z}$ exist. However, the anomaly for CO_2 is still present. There is a slight difference in the peak temperatures predicted at $x/d = 10$ in Figure 5.20f. At $x/d = 20$ the realizable k-ε closure gives a better prediction than the RS closure.

5.7 NO$_x$ Prediction

The post-processing method for NO_x, discussed in Section 3.3, using Zel'dovich chemistry with and without partial equilibrium assumptions for O and OH, is applied to
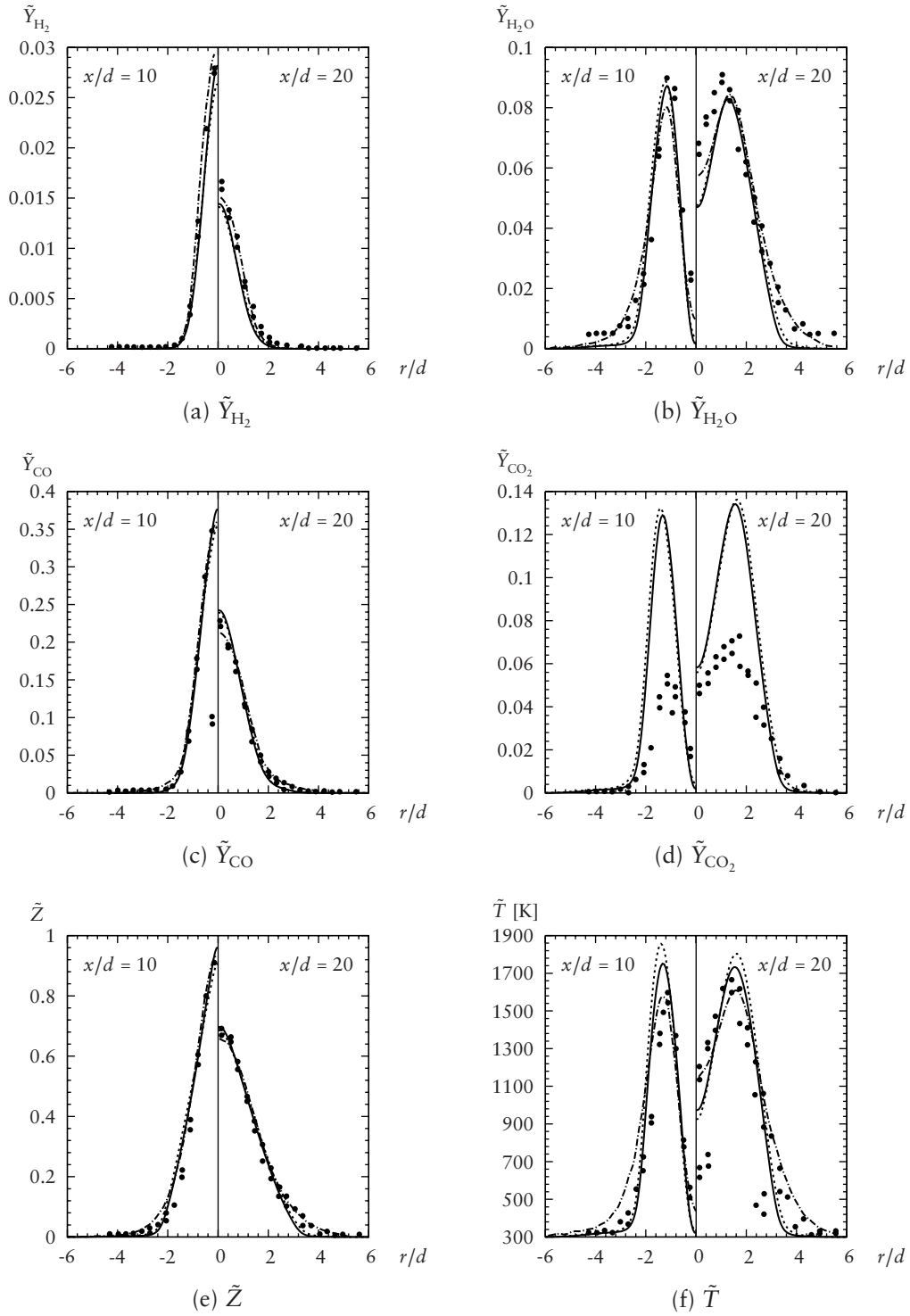
Figure 5.20: Radial profiles of mass fractions, $\tilde{Y}_\alpha$, mixture fraction, $\tilde{Z}$, and temperature, $\tilde{T}$, using the EDC (Cases A & B) with altered constants: • experimental data [28], ——realizable k-ε and ···· RS closure predictions with 6-step reduced mechanism.
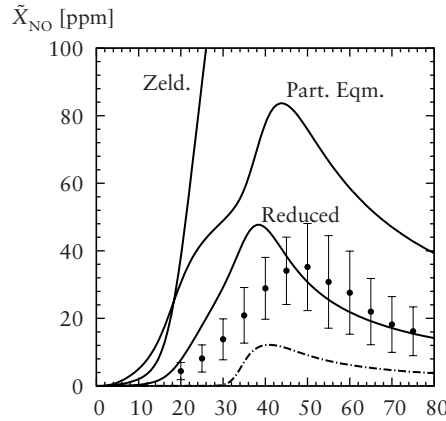
Figure 5.21: Graph showing variation of centreline NO values using different prediction methods for the jet flame. The post-processing approach using the 3-step Zel'dovich chemistry with and without partial equilibrium assumptions for O and OH (see Section 3.3) are shown, along with the prediction for Case A using the 6-step reduced mechanism. Also shown (as — · —) is the post-processing approach applied to the SLFM prediction (Case C).

the jet flame for Case A. The scalar fields are frozen, with only a $\tilde{Y}_{NO}$ transport equation solved. The source term is supplied using Equations (3.62) and (3.66). If partial equilibrium is assumed for O and OH then their concentrations are calculated using Equations (3.63) and (3.64), respectively. The $\tilde{X}_{NO}$ predictions using three approaches are given in Figure 5.21: (i) $\tilde{Y}_{NO}$ predicted using the reduced 6-step mechanism given in Chapter 4; (ii) $\tilde{Y}_{NO}$ predicted using the Zel'dovich mechanism with O and OH predicted using the reduced 6-step mechanism; and (iii) $\tilde{Y}_{NO}$ predicted using the Zel'dovich mechanism with O and OH assumed to be in partial equilibrium. In addition, Figure 5.21 gives the $\tilde{Y}_{NO}$ prediction using the Zel'dovich approach with the SLFM and realizable k-ε turbulence closure; Case C.

A large variation in the predicted peak values is seen. The reduced mechanism gives the closest prediction to experimental values. The Zel'dovich approach greatly over-predicts the peak values by an order of magnitude due to the over-prediction of $\tilde{T}$ shown in Figure 5.12a. As NO$_x$ is highly sensitive to temperature, any over-prediction in $\tilde{T}$

is expected to have a large impact on NO_x predictions [113]. However, the prediction made using the reduced mechanism does not suffer from this, likely to be due to NO removal in the post-flame gases. Inaccurate calculation of the concentration of O and OH are also a possible source of error. Interestingly, the predictions using the Zel'dovich approach with partial equilibrium assumptions are better than those made without the assumptions. This is likely to be due to the compounding of errors; the partial equilibrium assumptions are probably under predicting O and OH concentrations resulting in a lower value of $\tilde{Y}_{NO}$ for the same value of $\tilde{T}$. The predictions made for Case C, using the SLFM instead of the EDC, give a lower peak value than found experimentally. This is consistent with the lower peak temperature predicted, shown in Figure 5.12b. The post-processing method of Kim et al. [62], shown in Figure 5.13b, involves calculating the reaction rates of NO prior to the CFD calculation and storing them in the flamelet files. These reaction rates are then extracted and the Favre-mean reaction rate is calculated in the same way as species mass fractions. This means the variance of mixture fraction (and hence temperature) has a greater impact on the reaction rate values than through the assumptions made in formulating Equation (3.68). This may explain why the post-processing approach of the current study gives predictions that deviate somewhat from experiment. In addition, the predictions are sensitive to the number of 'bins' in normalized temperature, $\mathcal{T}$, space due to the non-gaussian shape of NO formation in relation to temperature.

5.8   Radiation Effects

The radiation model described in Section 3.4 is implemented via a custom-written UDF following Barlow et al. [5]. This adds a sink term, $\bar{\mathcal{Q}}$, in Equation (3.27) which depends on the local values of temperature, pressure and concentrations of H_2O, CO_2 and CO.
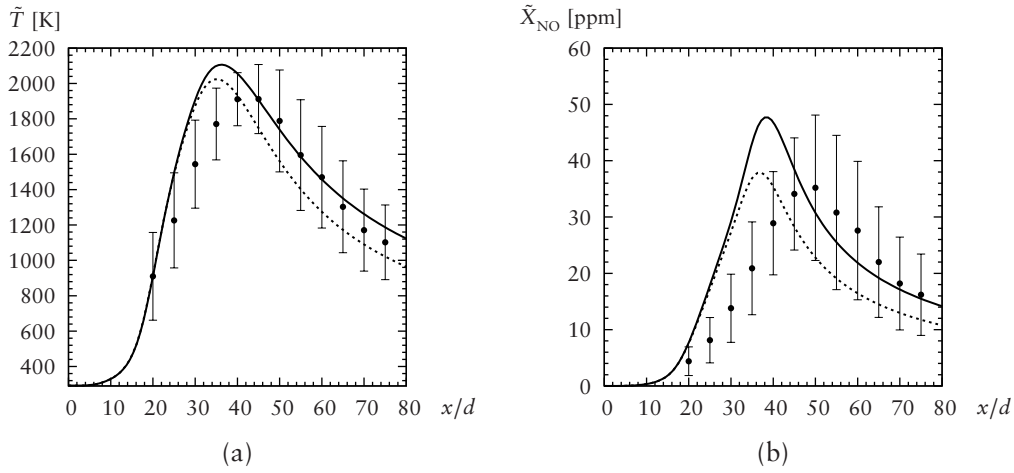
Figure 5.22: Adiabatic and non-adiabatic centreline profiles of temperature, $\tilde{T}$, and $\tilde{X}_{NO}$ [ppm] for the jet flame using the EDC (Case A) with standard constants: • experimental data [6], — adiabatic and ···· non-adiabatic predictions with 6-step reduced mechanism.

Figure 5.22 gives a comparison of the adiabatic and non-adiabatic profiles of centreline temperature and NO concentration for the jet flame. The inclusion of $\bar{\mathcal{Q}}$ decreases the peak temperature by $\approx 80\,°C$ or 4%, as shown in Figure 5.22a. Downstream of the peak location, the difference between adiabatic and non-adiabatic solutions widens. The NO predictions, as expected, follow a similar trend as shown in Figure 5.22b. The peak $\tilde{X}_{NO}$ value is decreased by ≈ 10 ppm or 20%. The inclusion of radiation gives a better prediction of both peak temperature and peak NO values, although the peak location differs somewhat from experiment. This result suggests that including radiation in combination with a decrease in C_2, as shown in Section 5.6 and Figure 5.17, would give a better agreement with experiment.

5.9 Summary

The reduced 6-step mechanism developed in Chapter 4 is applied to two turbulent syngas flames. Predictions are made with the reduced mechanism via two turbulent combustion models (the EDC and SLFM) using two turbulence closures (the realizable k-ε and RS). Comparison is made to published experimental and numerical data for temperature and species. The performance of the reduced mechanism is acceptable for both flame configurations studied. The differing reaction rate modelling approaches (using standard constants) give acceptable agreement to experiment, though the predictions differ between models. The inclusion of preferential diffusion in the EDC may have an impact on the location of flame stabilization. A greater interaction is seen between the reaction rate model and the turbulence closure using the EDC compared to the SLFM, suggesting a closer coupling.

The simpler realizable k-ε turbulence closure is found to give predictions very similar to those of the more complex RS closure. Alteration of turbulence closure constants is found to have an impact on the mixture fraction field predictions, and hence the scalar field. Slight alterations of the constants are made and a better match to experiment is found. Inclusion of heat loss due to radiation has an effect on both temperature and NO predictions. Using both altered and un-altered constants with the EDC gives reasonable NO and CO predictions. Given prior knowledge of detailed scalar measurements suitable alterations of model constants may be made to improve the predictions. However, without such knowledge (as in the off-gas burner) the standard model constants give acceptable agreement to experiment for the use of the modelling approach presented as a design tool.

The use of the reduced 6-step mechanism with the EDC, with turbulence closure given by the simpler realizable k-ε closure, appears justified for turbulent H_2/CO/N_2

flames. The EDC has an advantage over the SLFM as it includes preferential diffusion, which may be important in the off-gas burner, and it does not require the generation of a flamelet library. For parametric studies where fuel or oxidizer streams vary, this could give a significant saving of pre-processing time. The modelling approach discussed in this chapter is now applied to the off-gas burner.

Chapter 6

Slotted Burner Modelling

The slotted burner design, forming the basis of this study, was developed and tested by Grimwood [50] who undertook comprehensive measurements at atmospheric pressure. The effect of ambient ($\approx$ 300 K) and high ($\approx$ 1100 K) inlet temperatures on the burner performance were investigated where pollutant evolution, particularly readings for CO and NO_x, was of particular interest. In this chapter the modelling of the off-gas burner is discussed and the results of the simulations are presented.

Much of the burner design work was conducted concurrently with the modelling work presented in previous chapters. Initially, the burner design was thought to give a turbulent flame. Thus, the modelling work conducted in Chapter 5 was for turbulent flames. As the burner configuration changed during the design process, the flow was observed to be mostly laminar [50]. This resulted in a change in the modelling procedure, as will be discussed below.

6.1 Background

The SOFC hybrid cycle, described in Chapter 2, requires a low-emissions burner to oxidize the partially reacted streams (known as off-gas or tail gas and having mixture compositions similar to syngas) exiting the fuel cell. The design process for the burner looked at a number of ways of introducing the fuel and oxidizer streams to achieve high levels of mixing with low pressure loss, before settling on a slotted configuration [50]. This configuration features a number of individual fuel and oxidizer streams (not necessarily in a 1 : 1 ratio) combined together in repeating sections as described in Chapter 2. The streams are separated by splitter plates which results in a number of flames forming above the fuel slots, as shown in Figure 2.6a. The flow direction within each stream is controlled through the use of corrugations, which can be angled from 0° to ±30°, with the intention that mixing would be improved by a larger relative flow angle between adjacent slots.

At the outset of the experimental work it was thought that the large number of shear layers generated downstream of the splitter plates would result in a turbulent flow field [50]. However, the results presented by Grimwood [50] indicate that the flow field was predominantly laminar in the near-field, becoming turbulent further downstream. It was also found that the angled flow had relatively little impact on the overall level of mixing, as indicated by CO and NO levels downstream of the burner. A greater effect on the mixing was observed by varying the fuel to air slot ratio within each section. The greatest impact was by varying the mass flow (and hence velocity) difference between the fuel and air streams, however, this has the undesirable consequence of increasing the pressure loss across the burner. These observations of the mixing behaviour allow a number of assumptions (periodicity and reduction in dimensionality) which help to simplify the model of the burner and thus reduce the computational requirement.

The burner features a wide range of geometrical length scales. The downstream limit of the computational grid required to capture the flow field is ≈ 100 mm for the atmospheric temperature case and ≈ 240 mm for the high temperature case. In the third dimension a depth of at least the width of the actual burner is required if entrainment is ignored, and this would be increased if the effects of entrainment were to be included. To capture this mixing field with sufficient accuracy a very fine mesh is needed, particularly in the near-field of the splitter plates. This has the unavoidable consequence of increasing the computational effort. Reducing the mesh density close to the inlet and downstream of the splitter plates reduces the resolution of the flow details. For example, immediately downstream of the splitter plates will be a region of high shear. It is this shear that results in mixing of the fuel and oxidizer streams. A coarse mesh in this region could result in an incorrect calculation of the shear layer and incorrectly model the mixing field. The correct prediction of the scalar field relies on representing their mixing accurately and a trade-off exists between the accuracy of a dense mesh and the speed of a coarse mesh. Other simplifications can be made to reduce the computational requirements, as discussed next.

The impact of flow angle difference on emissions was observed to be small [50]. Hence, this feature of the geometry can be ignored without significantly affecting the calculated emissions. A further assumption is that the flow is uniform in the z direction (as indicated in Figure 2.6b), and the burner could be modelled in two dimensions assuming infinitely long slots. In a two-dimensional model, the effects of entrainment are ignored. In addition, the repeating (or periodic) nature of the slots may be used to reduce the number of 'units' modelled — each unit in any burner has an identical make-up. In the results presented below, two units are modelled with periodic boundary conditions on either side.

These geometric simplifications, when combined with the simple turbulence and ki-

netic models discussed in Chapters 3 and 4, make multi-variable parametric studies, of the type used in industrial design, less prohibitive financially. The numerics and boundary conditions are presented next.

6.2 Numerics

Previous work observed that the flow through the burner was predominantly laminar in the near-field developing to turbulent flow downstream [50]. The realizable k-ε closure is used to close the RANS equations as it has the advantage of requiring fewer variables than the Reynolds stress closure and, hence, lower computational requirements. The standard realizable k-ε closure constants are used (given in Table 3.1) because velocity and turbulence quantities were not available from experiments. The numerical study of jet and bluff-body flames presented in Chapter 5 gives confidence that the standard constants will give acceptable predictions of the mixing. Other numerical details are as described in Section 3.5, unless otherwise indicated. The 6-step reduced mechanism detailed in Chapter 4 is used for all simulations unless stated otherwise.

The grid used is a combination of quadrilateral and tetrahedral cells, as shown in Figure 6.1. The grid is quadrilateral and dense immediately downstream of the inlets, changing to an expanding triangular grid to reduce memory requirements. The total number of nodes is ≈ 8600. For the high temperature simulations the domain is extended downstream to the experimental measuring location. The grid was increased in resolution until changes in results were small.
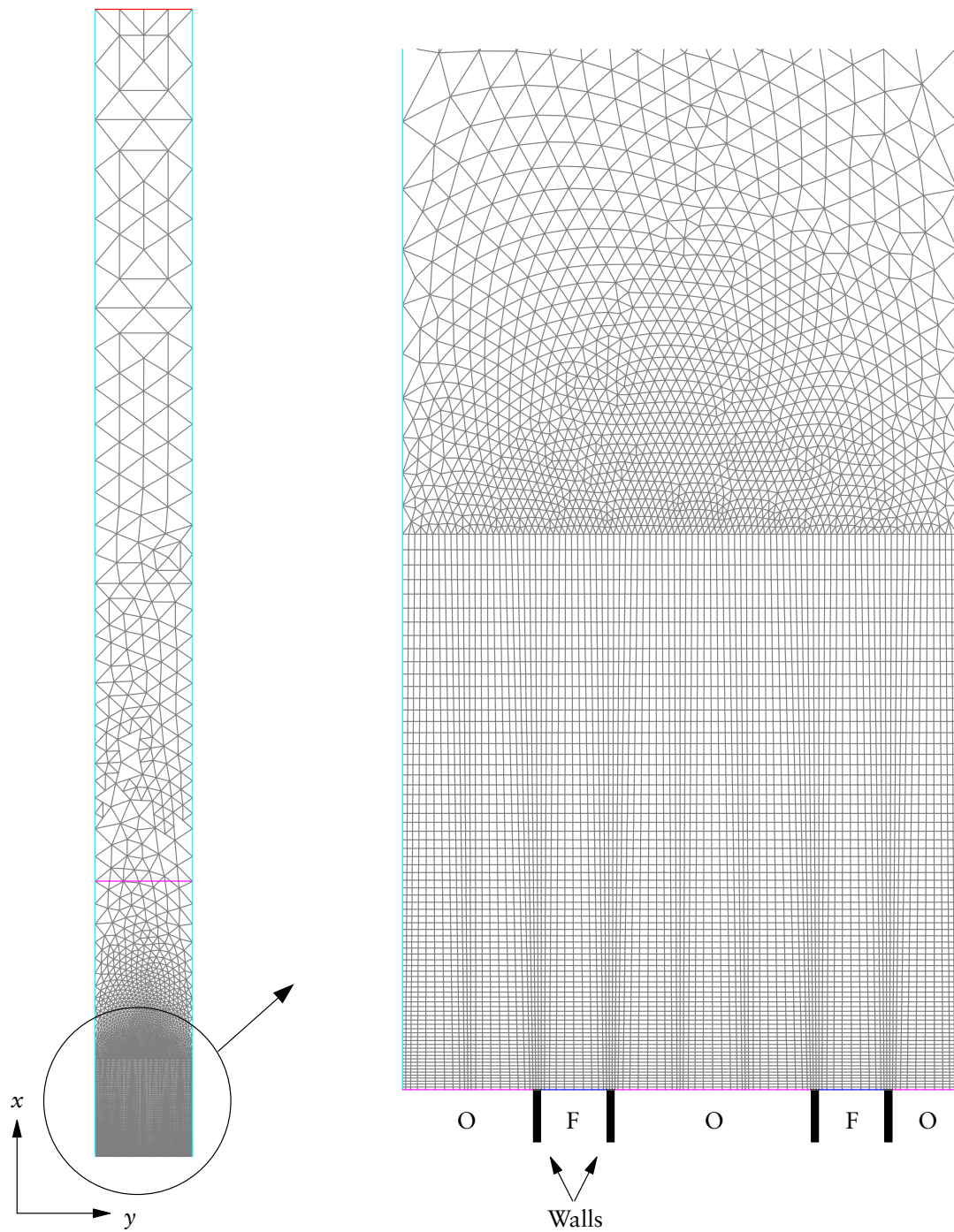
Figure 6.1: Computational mesh used for atmospheric off-gas burner calculations. A structured quadrilateral mesh is used for the inlet region, changing to a tetrahedral mesh further downstream; shown in the expanded view. Also shown are the locations of fuel (F) and oxidizer (O) stream inlets, and the location of the splitter plate walls.

Table 6.1: Overview of off-gas burner atmospheric (ATP) test conditions.

Variable	Conditions	Figure
Equivalence Ratio, ϕ	Table C.1	Figure 6.3
Bulk Velocity, v_{bulk}	Table C.2	Figure 6.5
H_2 : CO Ratio	Table C.3	Figure 6.6

Table 6.2: Overview of off-gas burner high temperature (HT) test conditions.

Variable	Conditions	Figure
Equivalence Ratio, ϕ	Table C.4; DATUM & 1–4	Figure 6.8
Bulk Velocity, v_{bulk}	Table C.4; 8–11	Figure 6.9

6.3   Boundary Conditions

The inlet boundary conditions used in this study match the experimental conditions from Grimwood [50]. A full listing of those used is given in Appendix C.1. The inlet boundary conditions used for each variable sweep are given in Tables 6.1 and 6.2 for the atmospheric (ATP) and high temperature (HT) simulations, respectively. The figure giving the corresponding results is also indicated. For each case the equivalence ratio, ϕ, and the bulk velocity, v_{bulk}, are varied keeping other variables as constant as the experimental methods allowed [50]. In addition, the H_2 : CO ratio for the ATP conditions is varied.

Mass flow inlets are used for each fuel and oxidizer inlet. Turbulence parameters are set by prescribing a low value of turbulence intensity, $I = 0.1\%$, reflecting the experimentally observed laminar flow emerging from each slot, and the calculated hydraulic diameter, d_h. The turbulent length scale is calculated using $\ell = 0.07 d_h$, where $d_h = 1.97 \times 10^{-3}$ m [82]. For simplicity, a top-hat profile is used for both mass flows and

turbulence parameters. This is justified by the short length of the corrugations used in the actual burner. The inlet temperatures are set to 300 K for the ATP calculations. For the HT calculations the inlet temperatures are set to values given in Table C.4, corresponding to those determined experimentally [50]. All walls are assumed to be adiabatic and have no slip conditions. The pressure on the downstream boundary is set to be atmospheric. The left and right boundaries are set as periodic. Results for the ATP and HT conditions are given next, followed by high pressure cases.

6.4   Results for Atmospheric Conditions

The reduced mechanism developed in Chapter 4 is used via the interface between FLUENT and the external subroutine described in Section 5.3. This reduced mechanism incorporates recent updates to $H_2/CO/N_2$ kinetics [30] with fewer scalars than the full, detailed mechanism, whilst retaining the relevant physics, such as the varying chemical timescales present. The presence of hydrogen in the fuel stream necessitates the use of full multi-component molecular and thermal diffusion effects.

The general procedure, using the realizable k-ε closure, detailed in Chapter 5 is applied to the off-gas burner to capture the turbulent flow field later on. FLUENT's implementation of the EDC and SLFM fails to predict a stable flame and blow-off is observed. There is not enough scope in the uncertainty of the boundary conditions, such as the turbulence intensity, inlet stream or wall temperatures, to be able to produce a stable flame by varying them.

The failure of the EDC approach may be attributed to its eddy-cascade-based formulation. The turbulent kinetic energy and its rate of dissipation appear in Equation (3.46) via the fine-structures fraction, Equation (3.47), and the fine-scale mixing,

Equation (3.49), respectively;

$$\gamma^* = \left(\frac{3C_\beta}{4C_\alpha^2}\right)^{1/4}\left(\frac{\nu^*\tilde{\varepsilon}}{\tilde{k}^2}\right)^{1/4},$$
$$\tau^* = \left(\frac{C_\beta}{3}\right)^{1/2}\left(\frac{\nu^*}{\tilde{\varepsilon}}\right)^{1/2}.$$

If the turbulence quantities are incorrectly predicted (either in magnitude or location), or simply too low, the values of γ^* and τ^* could vary and directly impact on the mean reaction rates calculated. The strong non-linearity of Equation (3.46) increases the effect of any discrepancy. If, for example, $\tilde{\varepsilon}$ is over-predicted then the mixing time τ^* decreases. This decrease could reduce the time over which the reaction occurs to a level where blow-off occurs. Likewise, an over-prediction of $\tilde{k}$ leads to a decrease of γ^*, the fraction of flow where reaction can occur. The SLFM, with a differing formulation to the EDC, still fails to predict a stable flame. Like with the EDC, low values of $\tilde{k}$ and $\tilde{\varepsilon}$ would impact on the $\widetilde{Z''^2}$ field through the presence of μ_t ($= \bar{\rho}C_\mu\tilde{k}^2/\tilde{\varepsilon}$) and $\tilde{\chi}$ ($= C_\chi\widetilde{Z''^2}\tilde{\varepsilon}/\tilde{k}$) in Equation (3.57) and of μ_t in Equation (3.55). This could lead to incorrect scalar values being interpolated from the flamelet library. If alternate conditions are used, particularly featuring an increase in bulk velocity, the EDC and SLFM may be more appropriate choices to represent the increased turbulence-chemistry interaction, as in Chapter 5. In addition, the adiabatic assumption, whereby radiative heat transfer to the burner surface is neglected, and therefore the pre-heating the incoming fuel and air is not represented, could be detrimental to flame stabilization. In fact, this contribution to flame stability was discussed for the jet flame in Section 5.5.2 [3].

As the flow issuing from the slots is laminar, laminar finite-rate kinetics (as described in Section 3.2.1) are adopted for the results presented here, meaning $\bar{R}_\alpha = R_\alpha$ in Equation (3.24) and turbulent fluctuations of temperature are ignored. This may be appro-
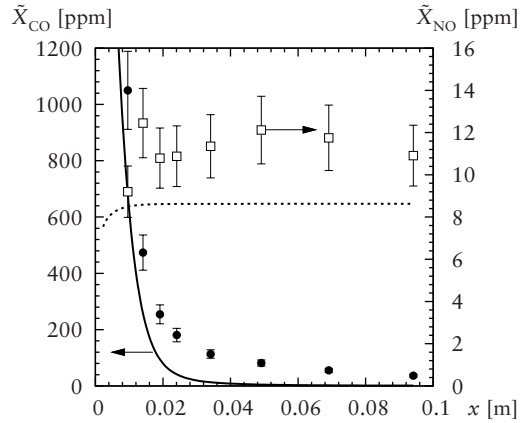
Figure 6.2: Graph of CO and NO concentrations [ppm] downstream of the inlet for atmospheric Condition 1 at atmospheric pressure: —— and • CO results for computation and experiment [50], respectively, ···· and □ NO results for computation and experiment [50], respectively. Error bars indicate estimated uncertainties [50]. Inlet conditions used are given in Table 6.1.

priate for the off-gas burner under the particular conditions studied here due to the low turbulence levels at the inlets [14]. As with the EDC, transport equations for each species are solved but with $\bar{R}_\alpha$ calculated directly using the reduced mechanism via the CHEMKIN subroutine. As such, the total number of species appearing in the mechanism has a clear impact on computational requirements.

Figure 6.2 shows the downstream evolution of CO and NO concentrations for Condition 1 at ATP, given in Table C.1. The experimental values given in Figure 6.2 were obtained using the 30° burner configuration [50, Chapter 8] as results for 0° are not available for this particular set of readings. The predictions are made assuming a two-dimensional 0° configuration. This is justified as the experimental work showed little difference in readings between 0°, 15° and 30° flow angles for both CO and NO readings [50]. The predictions for both CO and NO give similar profiles to experiment. The predicted NO level rises and reaches a steady value before $x \approx 0.02$ m. The experimental results show a similar profile, though higher values are indicated and there is some
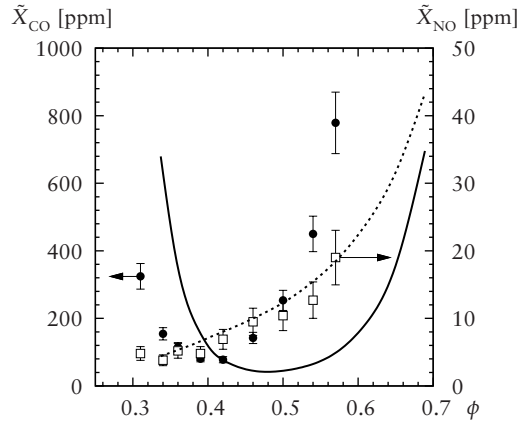
Figure 6.3: Graph of CO and NO concentrations [ppm] with varying equivalence ratio, ϕ: —— and • CO results for computation and experiment [50], respectively, ···· and □ NO results for computation and experiment [50], respectively. Error bars indicate estimated uncertainties [50]. Inlet conditions used are given in Table 6.1.

variation downstream. This shows that NO is formed close to the flame front, then the NO level is quickly frozen by mixing with cool oxidizer and the subsequent temperature reduction. The CO evolution indicates the longer τ_{CO} times expected for CO oxidation. The predicted CO concentrations reach zero at $x \approx 0.06$ m. The experimental results indicate that the CO oxidation is even slower, as a significant concentration of CO is seen at $x = 0.1$ m.

The results for sweeps of equivalence ratio, bulk velocity and $H_2 : CO$ ratio for ATP conditions are given in the following sections.

6.4.1 Effect of Equivalence Ratio

Figure 6.3 shows CO and NO concentrations with varying equivalence ratio, ϕ. The experimental conditions used for the calculations are given in Table C.1. The NO predictions give good agreement to experiment. The trend and magnitude of the readings are within the experimental uncertainty over the equivalence ratio range. NO forma-

tion occurs in high temperature regions such as the flame front. The flame temperature increases with ϕ due to the increase of fuel and corresponding decrease of diluent, indicated in Figure 2.1. The observed NO concentrations increase with ϕ due to the increase in flame temperature. The agreement between the experimental NO and calculated NO levels, formed via the thermal NO_x route, suggest that the heat release and temperature predictions are likely to be in agreement with those from experiment.

The experimental results of Grimwood [50] show that CO concentrations initially decrease with increasing ϕ until a minimum point is reached; approximately 77.7 ppm at $\phi \approx 0.42$. From this minimum the CO concentrations then increase with increasing ϕ. The computational results for CO predict a similar trend. However, the minimum value is shifted to richer conditions; 44.0 ppm at $\phi = 0.463$. The predicted minimum CO region is broader than indicated by the experiments; as seen in the range $0.42 \lesssim \phi \lesssim 0.55$ for the predictions and $0.38 \lesssim \phi \lesssim 0.44$ for the experimental results. The predicted decrease and increase of CO before and after this minimum region gives similar magnitudes to experiment. For $\phi \lesssim 0.42$ the predictions appears shifted to richer conditions. Whereas for $\phi \gtrsim 0.42$ the computational model appears to under-predict the CO concentration.

The differences between predictions and experiment may be attributed to incorrect prediction of mixing or kinetics, or even a combination of the two. The differences in CO values between experiment and calculations can partly be explained by considering the effect of the local mixture composition and temperature on the kinetics. The oxidizer stream mixing with the fuel stream close to the splitter plates will supply the O_2 needed for oxidation. Further downstream, the oxidizer stream mixing with the hot post-flame gases will reduce the temperature of the mixture, inhibiting oxidation. For $\phi \lesssim 0.42$ the increase of CO concentration is due to the decrease in temperature as the mixture becomes leaner. This reduction in temperature inhibits CO oxidation. Any discrepancy
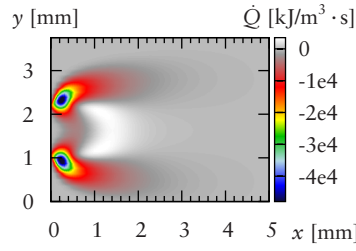
Figure 6.4: Heat release, $\dot{Q}$ [kJ/m$^3\cdot$s], in the near-field region for Condition 1 at atmospheric pressure shown as a colour-map. The fuel slot extends from 1.126 to 2.126 mm. Inlet conditions used are given in Table 6.1.

in temperature predictions has a knock-on effect on the reaction rate of CO. The reduced mechanism may be under-predicting these rates at such low temperatures ($\approx$ 1200 K). For $\phi \gtrsim 0.42$ the increase in CO concentration is due to the lack of O$_2$ locally as the mixture becomes richer. This lack of O$_2$ inhibits the oxidation of CO.

However, the NO predictions give confidence that the temperature is being correctly predicted. This implies the kinetics may not be the source of the shift in CO predictions. Mixing, both turbulent and molecular, in the near field is the likely source of discrepancy. As shown in Figure 6.4 the majority of the heat release, $\dot{Q}$, occurs very close to the splitter plates; within 1 mm or one slot width. Hydrogen is expected to diffuse quickly away from the fuel stream and react faster compared to CO. The radicals formed by this process go on to oxidize CO. The shift in CO predictions could be due to deficiency in the transport properties of H$_2$ and H at these lean, dilute conditions [33, 80]. If the diffusion (either thermal or molecular) of H$_2$ is over-predicted there may be a lack of O radicals to oxidize the CO, as the O may have recombined to form H$_2$O. Dong et al. [33] and Middha et al. [80] have shown a discrepancy between the standard CHEMKIN transport properties for H$_2$, as used in the present work, and experiment over a range of pressures and temperatures. These discrepancies in the binary diffusion coefficient $\mathcal{D}_{\text{H}_2,\text{N}_2}$ lead to large changes in extinction strain rates in premixed flames [33]. It is
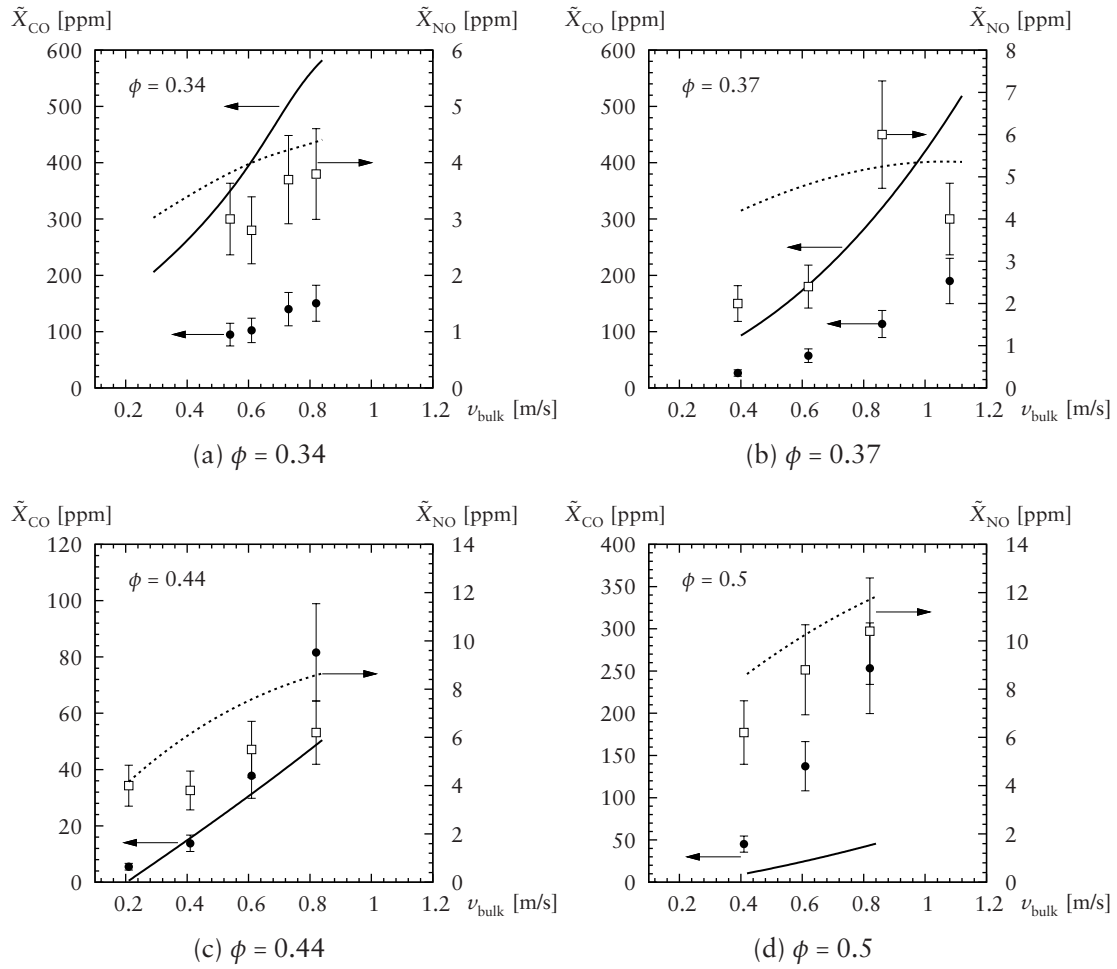
Figure 6.5: Graph of CO and NO concentrations [ppm] with varying bulk velocity, v_{bulk} [m/s]: ── and ● CO results for computation and experiment [50], respectively, ···· and □ NO results for computation and experiment [50], respectively. Error bars indicate estimated uncertainties [50]. Inlet conditions used are detailed in Table 6.1.

reasonable to expect a similar impact on non-premixed flames where diffusion effects are more important.

6.4.2 Effect of Bulk Velocity

Figure 6.5 gives CO and NO concentrations with varying bulk velocity, v_{bulk}, at differing equivalence ratios. The experimental conditions used for the calculations are given in

Table C.2. The bulk velocity is inversely related to the mean residence time with high values of v_{bulk} giving shorter residence times. In addition, increases in v_{bulk} also increase the flame length.

In general, the NO predictions follow the experimental trend at each value of ϕ; increasing with increasing v_{bulk}. This is due to the increase in size of the high temperature region, caused by the increase of the flame length as v_{bulk} increases. A large high temperature region increases the region where NO can form. Figure 6.5 also shows that as ϕ increases the NO concentration increases. This is due to the increase of flame temperature with ϕ, and thus a corresponding increase in NO. Once out of the high temperature region, the reaction is quenched due to the fast mixing of the cold oxidizer stream. However, at these low levels of NO_x emissions, the sensitivity of the measuring equipment used results in a large degree of uncertainty [50].

The CO predictions follow the experimental trend; CO levels increase with increasing v_{bulk}, or decreasing residence time. As the residence time decreases the length of time CO spends in the high-temperature region is reduced. Consequently, there is less time for oxidation of CO to occur. This is consistent with known timescales for CO oxidation [66]. The predictions are consistent with the findings in Section 6.4.1. At $\phi \lesssim 0.42$ (shown in Figures 6.5a and 6.5b) the computational model over-predicts the CO concentration, possibly due to the temperature being under-predicted and hence inhibiting CO oxidation, or the lack of O radicals due to incorrect prediction of H_2 diffusion, as discussed above. At $\phi = 0.44$ the CO values predicted are in agreement with experiment over the range of v_{bulk} values, which coincides with the closest match in Figure 6.3. In general, the discrepancies between experiment and predictions increase with increasing v_{bulk}. As the mass flows of fuel and oxidizer are increased concurrently, the flow becomes increasingly turbulent. The lack of turbulence-chemistry interaction becomes noticeable in the CO predictions. In this case, diffusion via turbulence begins
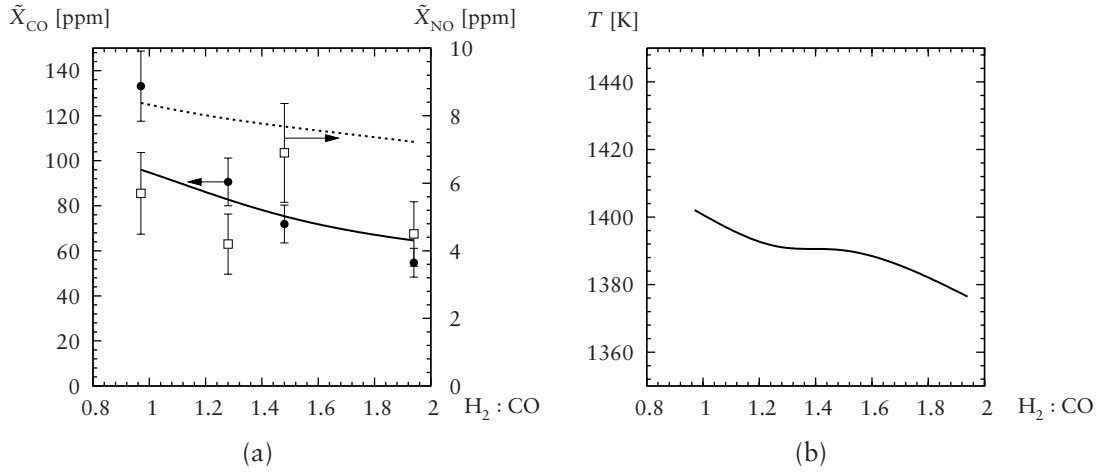
Figure 6.6: Graph of CO and NO concentrations [ppm] (a), and temperature [K] (b) with varying H_2 : CO ratio at $\phi \approx 0.42$: —— and • CO results for computation and experiment [50], respectively, ···· and □ NO results for computation and experiment [50], respectively. Error bars indicate estimated uncertainties [50]. Inlet conditions used are given in Table 6.1.

to dominate over molecular or thermal diffusion. On the other hand, increasing the velocity increases the flame length. The discrepancies could be caused by CO bypassing the hot regions immediately downstream of the splitter plates in the calculations.

6.4.3   Effect of H_2 : CO Ratio

Figure 6.6 gives CO and NO concentrations, and temperature with varying H_2 : CO ratio at $\phi \approx 0.42$. The experimental conditions used for the calculations are given in Table C.3. The CO predictions follow the experimental trend; decreasing with increasing H_2 : CO ratio, as shown in Figure 6.6a. The CO magnitudes are in general agreement with experiment, coinciding with the trend identified in Sections 6.4.1 and 6.4.2 for $\phi \approx 0.42$. The drop in CO concentrations is likely to be a consequence of both the reduced CO input into the system and the increased H_2 presence. As the H_2 : CO ratio increases there is a greater proportion of H_2 and thus a greater proportion of H_2O

formed, involving OH and O. Any increase in the availability of O will increase the oxidation of CO (see page 62).

A small temperature drop of the order of 15 K is observed in both predicted values, shown in Figure 6.6b, and experiment [50] (not shown due to large experimental uncertainties present). This temperature drop can be attributed to the increasing specific heat of the products due to the increased H_2O present. NO predictions follow the rough experimental trend of decreasing with increasing H_2 : CO ratio. This small decrease is due to the temperature variation with H_2 : CO ratio. As discussed above, the experimental uncertainty at these low NO_x values is high. However, the predictions give good qualitative results.

6.5   Results for High Temperature Conditions

Predictions are made using a set of high temperature and atmospheric pressure conditions (denoted HT and given in Tables 6.2 and C.4) that vary the equivalence ratio, ϕ, and bulk velocity, v_{bulk}. In the experiments a catalyst was used to generate the high temperatures and appropriate mixture compositions required. The inlet values for mixture composition represent theoretical estimates based on equilibrium calculations and, hence, there is a high degree of uncertainty in the species concentrations. It is therefore difficult to determine the behaviour as there may be discrepancies between the actual products of the catalyst reaction and those determined from theory [50].

The same numerics are used as in Section 6.4; the realizable k-ε closure with finite-rate kinetics and reduced 6-step mechanism. The computational domain has been extended to correspond to the experiment.

Figure 6.7 shows the downstream evolution of CO and NO concentrations for the DATUM condition at HT, given in Table C.4. No experimental data is available for
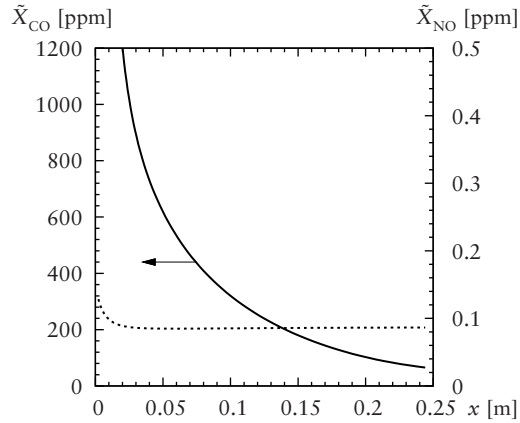
Figure 6.7: Graph of CO and NO concentrations [ppm] downstream of the inlet for high temperature DATUM condition at atmospheric pressure: —— CO and $\cdots$ NO results for computation. Inlet conditions used are given in Table C.4.

comparison. As with the ATP evolution, the NO formation occurs at the flame front and the NO levels are quickly frozen by mixing with cooler oxidizer to a steady value, as shown at $x > 0.03$ m. The CO levels decrease very slowly due to the lower peak temperatures present at these conditions preventing full oxidation.

6.5.1 Effect of Equivalence Ratio

Figure 6.8 gives the CO and NO concentrations with varying equivalence ratio, ϕ, up to 0.15 for high temperature conditions. At such lean conditions (representing the mixture composition in the SOFC hybrid cycle) both the adiabatic and stoichiometric temperatures are low (around 1300 K) compared to those for the atmospheric conditions (around 1800 K). These low temperatures inhibit both CO oxidation and NO formation. The CO predictions are of the same order of magnitude as the experimental readings. However, due to the uncertainty over the inlet conditions, no further analysis is justified. For NO, the predictions are of the same order of magnitude as experimental values. However, the uncertainty in gas sampling is high at such low NO concentra-

Figure 6.8: Graph of CO and NO concentrations [ppm] with varying equivalence ratio, ϕ, for high temperature conditions: —— and • CO results for computation and experiment [50], respectively, ···· and □ NO results for computation and experiment [50], respectively. Inlet conditions used are given in Table C.4.

tions [50].

6.5.2 Effect of Bulk Velocity

Figure 6.9 gives the CO and NO concentrations with varying bulk velocity, v_{bulk}, for high temperature conditions at $\phi = 0.069$. Because of the uncertainty in gas sampling, the experimental results show a high degree of scatter for both CO and NO. However, as with Figure 6.8 the predictions are of the same order of magnitude for both CO and NO. CO concentrations were found to increase with v_{bulk} using a particular set of inlet conditions [50]. The predictions follow this trend using all the inlet conditions. Due to the low overall temperatures of the conditions used the NO concentrations are small and within the experimental uncertainty.
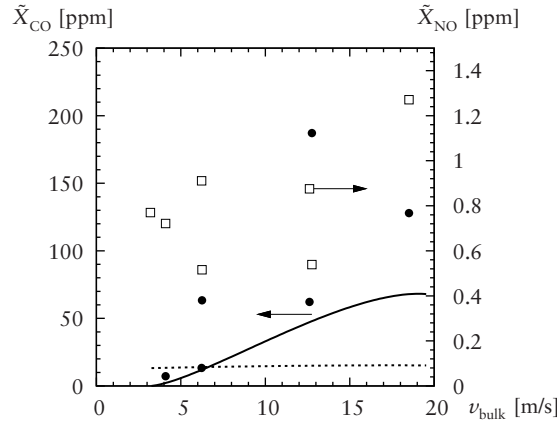
Figure 6.9: Graph of CO and NO concentrations [ppm] with varying bulk velocity, v_{bulk} [m/s], for high temperature conditions: — and • CO results for computation and experiment [50], respectively, ···· and □ NO results for computation and experiment [50], respectively. Error bars indicate estimated uncertainties [50]. Inlet conditions used are given in Table C.4.

6.6 Extension to High Pressure Conditions

The off-gas burner is intended to operate at high temperatures and pressures when used in an industrial setting. The ATP and HT conditions are selected for experimental convenience as high pressure tests are difficult and costly to conduct in a laboratory setting. This is where a computational model of the burner can be advantageous to the design process. The modelling procedure demonstrated above is extended by repeating Condition 1 from the ATP conditions (Table C.2) and DATUM from the HT conditions (Table C.4) with the pressure increased from 1 bar to 7 bar. Unfortunately, no experimental readings are available at high pressures to allow comparison. The ATP conditions are denoted as HP for the high pressure simulations. Similarly, the HT conditions are denoted as HTP for the high pressure simulations.
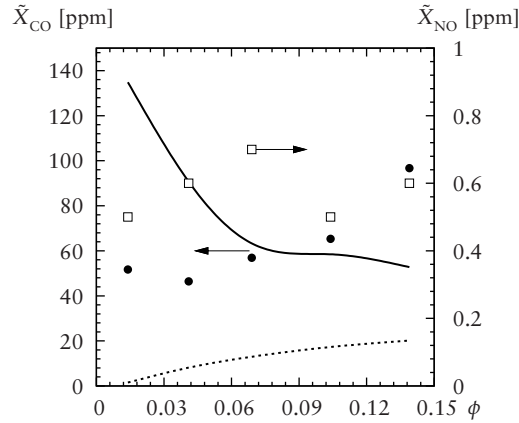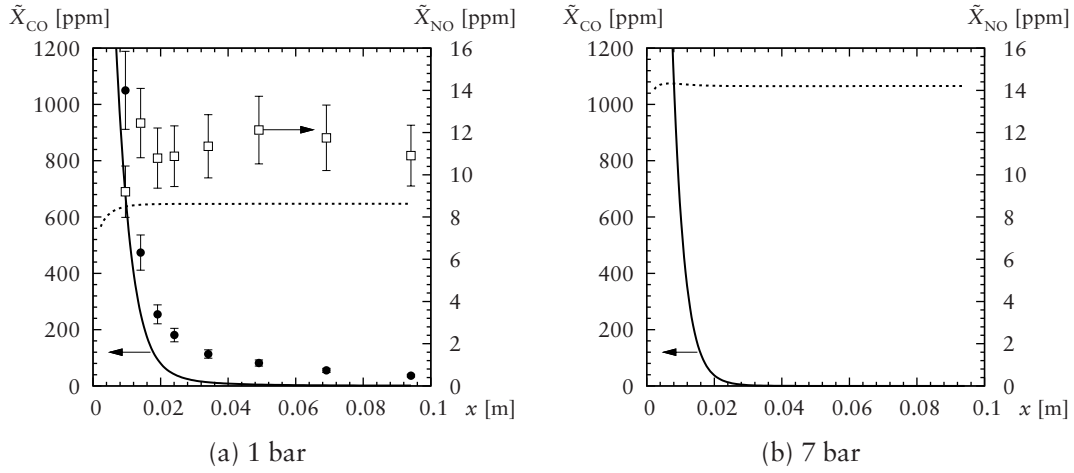
Figure 6.10: Graph of CO and NO concentrations [ppm] downstream of the inlet for atmospheric Condition 1 at atmospheric and high pressures: —— and • CO results for computation and experiment [50], respectively, ···· and □ NO results for computation and experiment [50], respectively. Error bars indicate estimated uncertainties [50]. Inlet conditions used are given in Table 6.1. (a) is a repeat of Figure 6.2.

6.6.1 ATP to HP Comparison

Figure 6.10 gives the downstream evolution of CO and NO concentrations for Condition 1 (ϕ = 0.502) at both 1 bar (repeated from Figure 6.2) and 7 bar. Similar evolutions of CO are seen for both ATP and HP. A slightly faster decrease (compared at x = 0.02 m) of CO concentrations is seen for 7 bar than for 1 bar. The NO predictions show an increase of $\approx$ 6 ppm from 1 bar to 7 bar. These two findings can be attributed to a faster reaction rate and higher temperatures achieved at the higher pressure. This is consistent with the greater number of molecular collisions expected at a higher pressure.

To highlight these observations, contour plots of OH mass fraction, $\tilde{Y}_{OH}$, and temperature are given in Figure 6.11 for both 1 bar and 7 bar. $\tilde{Y}_{OH}$ gives an indication of the flame front location. Viewing the temperature contours, it is seen that the high pressure case gives higher peak temperatures (1966 K at HP compared to 1837 K at ATP). The high temperature region (using the 1700 K contour) extends a similar distance in
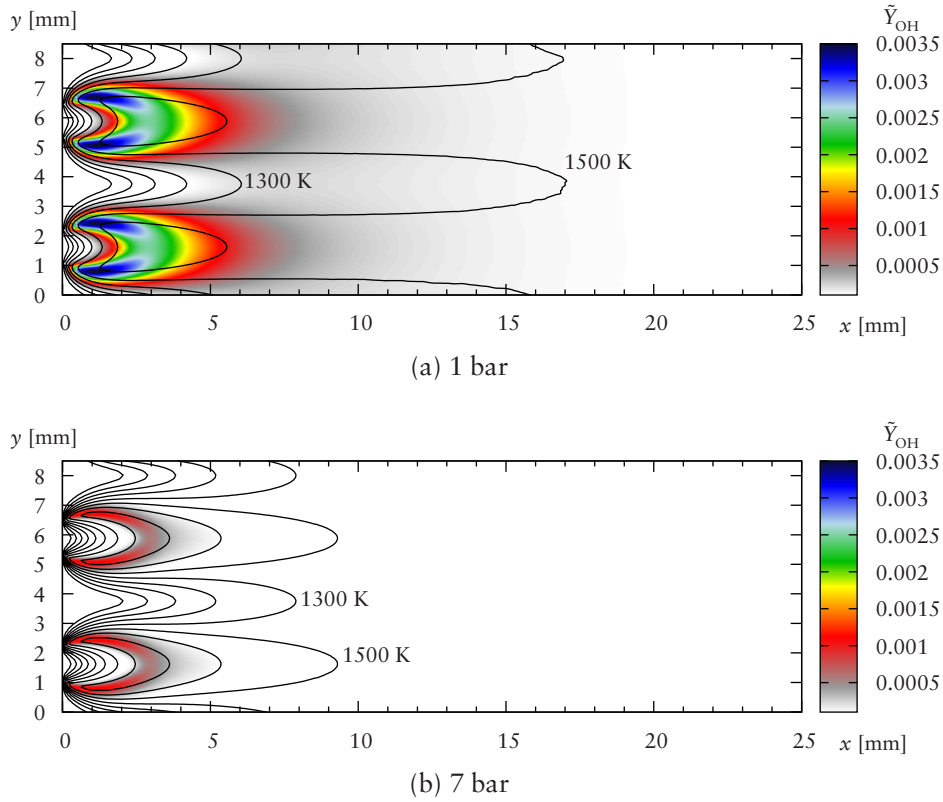
Figure 6.11: Temperature, $\tilde{T}$ [K], contour plot downstream of the burner for Condition 1 at atmospheric and high pressures. Temperature contours indicated at 200 K intervals, starting at 300 K. The predicted OH mass fraction, $\tilde{Y}_{OH}$, is also shown as a colour-map. The fuel slots extend from 1.126 to 2.126 mm and from 5.378 to 6.378 mm.

both cases. However, the temperature field reaches uniformity faster at high pressure, as seen by viewing the 1500 K contour. Viewing the OH field, it is seen that at high pressure the reaction zone is much thinner than at ATP. The peak value of $\tilde{Y}_{OH}$ at HP is also approximately three times less ($\tilde{Y}_{OH}$ = 0.0012) than at ATP ($\tilde{Y}_{OH}$ = 0.0035). This is as expected as the reactions occur faster and the intermediate species, such as OH, are converted to products.

To examine the reaction in the near field, plots of temperature, $\tilde{T}$ [K], heat release, $\dot{Q}$ [kJ/m$^3 \cdot$ s], and net rates of formation/destruction, $\bar{R}_\alpha$ [kg/m$^3 \cdot$ s], for CO, H$_2$ and NO are given in Figure 6.12 at both 1 bar and 7 bar. Firstly, the temperature plot again

shows a higher temperature predicted with the HP case. Secondly, it can be seen that the reaction zone is much thinner in the high pressure case by viewing the heat release or formation/destruction rates. This is particularly evident in the plots of $\bar{R}_{NO}$. The higher temperatures can be explained by the higher reaction rates, seen by viewing the maximum values of $\bar{R}_{\alpha}$ for CO and H_2. In the HP case, the rates are approximately three times higher than in the ATP case. The total heat release, $\dot{Q}$, is seen to be approximately six times higher in the HP case. As a result of this, the NO peak rate of formation is seen to be over two times higher for the HP case than the ATP. This explains the higher values predicted for the HP case shown in Figure 6.10. These findings are consistent with the greater number of molecular collisions expected at higher pressures.

A more detailed look at the NO field is given in Figure 6.13 for both 1 bar and 7 bar. Consistent with the findings for $\bar{R}_{NO}$ discussed above, it is seen that the peak NO concentrations are approximately two times higher at HP conditions. The majority of the NO is formed at the flame front, and the reaction is quickly quenched as mixing with the oxidizer stream occurs. The peak region is shorter with the HP case than the ATP case, as discussed above for the temperature field shown in Figure 6.11.

The velocity magnitude, v_{mag}, field for both 1 bar and 7 bar is shown in Figure 6.14. This comparison shows that at both pressures the predicted flow field remains similar, albeit with differing magnitudes.
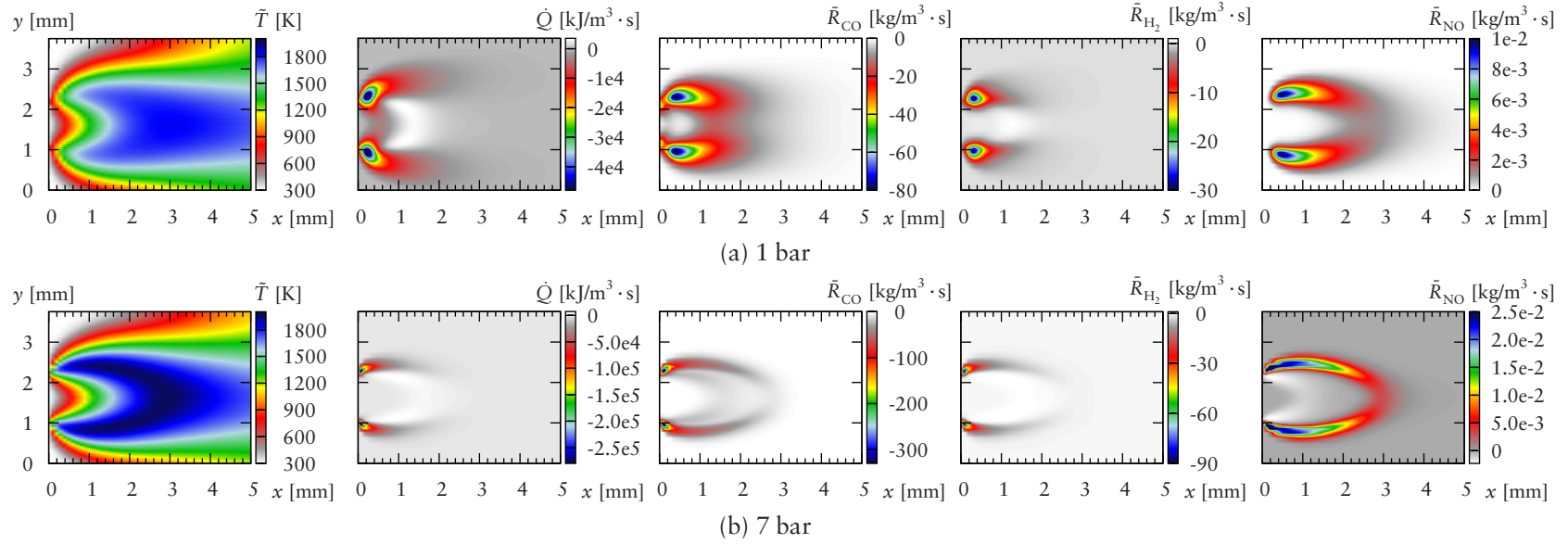
Figure 6.12: Temperature, $\tilde{T}$ [K], heat release, $\dot{Q}$ [kJ/m$^3 \cdot$s], and net rates of formation/destruction of CO, H$_2$ and NO, $\bar{R}_\alpha$ [kg/m$^3 \cdot$s], in the near-field region for Condition 1 at atmospheric and high pressures shown as a colour-map. The fuel slot extends from 1.126 to 2.126 mm.
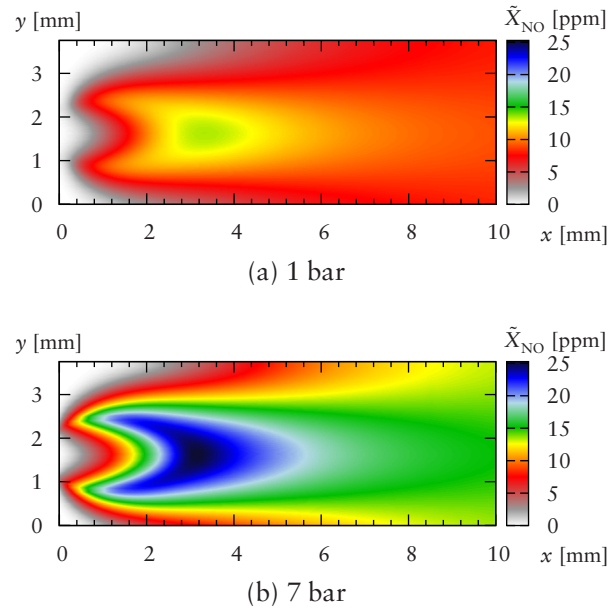
Figure 6.13: Plots of NO concentration, $\tilde{X}_{NO}$ [ppm], for Condition 1 at atmospheric and high pressures. The fuel slot extends from 1.126 to 2.126 mm.
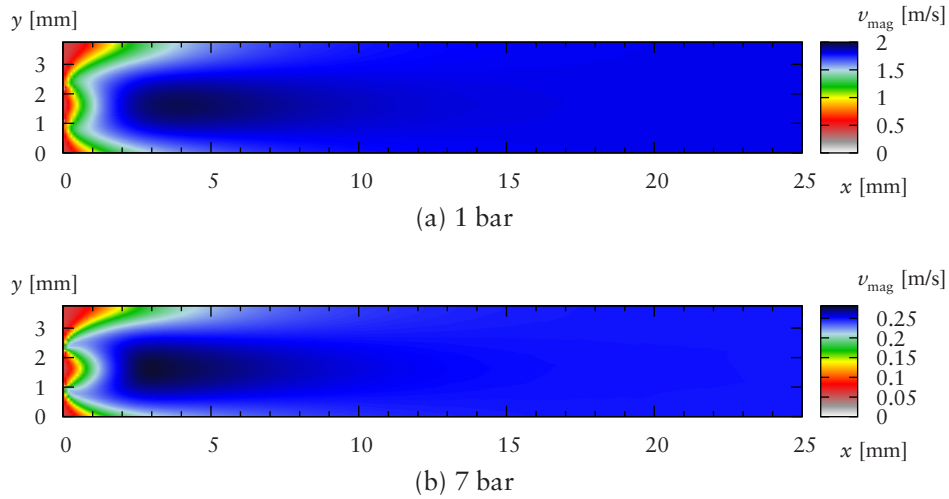
Figure 6.14: Plots of velocity magnitude, v_{mag} [m/s], for Condition 1 at atmospheric and high pressures. The fuel slot extends from 1.126 to 2.126 mm.

6.6.2 HT to HTP Comparison

The high temperature DATUM condition at 1 bar (given in Table C.4) is compared to the same inlet conditions at 7 bar, denoted as HTP. The same set of comparisons is made as in Section 6.6.1. No experimental data is available for comparison. The downstream evolution of CO and NO is given in Figure 6.15. For the HT DATUM case, shown in Figure 6.15a, the oxidation of CO is much slower than that seen in the ATP case (Figure 6.10a). The CO level predicted at the downstream extent is still developing with a value of ≈ 60 ppm. This is due to the very lean conditions and consequent low temperatures that inhibit CO oxidation. The NO levels are very low (sub-ppm) compared to the ATP case, again due to the low temperatures. The HTP case, shown in Figure 6.15b, indicates a much faster rate of CO oxidation (note the differing scales). There is a slight (< 0.02 ppm) increase in NO levels predicted. Both these observations are due to the greater rate of reaction and higher temperatures expected as the pressure is increased. This agrees with the observations in Section 6.6.1.

A comparison of the temperature field, shown in Figure 6.16 shows the higher temperatures experienced at high pressure (1766 K), indicated by the tightly spaced contours in Figure 6.16b, compared to 1 bar (1504 K). The length of the high temperature region, indicated by the 1300 K contour, is similar in both HT ($x = 11$ mm) and HTP cases ($x = 13$ mm). Comparing the OH field, also shown in Figure 6.16, shows that at high pressure the magnitude of $\tilde{Y}_{OH}$ is lower than at HT. As with the ATP and HP cases, shown in Figure 6.11, the increase in pressure increases the reaction rate due to the increase of molecular collisions leading to reaction. This in turn leads to a decrease in OH radicals, as they are consumed in the oxidation of H_2 and CO.

Examining the near-field temperature, heat release, and net rates of formation/destruction, shown in Figure 6.17, supports the previous observations. The flame area is

(a) 1 bar   (b) 7 bar
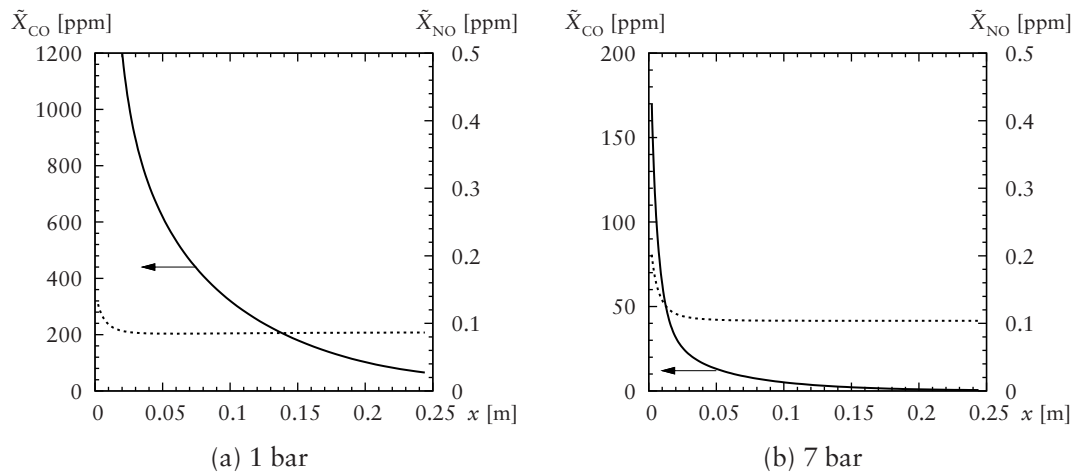
Figure 6.15: Graph of CO and NO concentrations [ppm] downstream of the inlet for high temperature DATUM condition at atmospheric and high pressures: —— CO and ···· NO results for computation. Inlet conditions used are given in Table 6.2. (a) is a repeat of Figure 6.7.

thinner and more compact in the HTP case than in the HT case. Due to the highly lean conditions present ($\phi = 0.069$), the flame is much smaller than in the ATP and HP cases (Figure 6.12). The high pressure predictions give higher temperatures, heat release, and net destruction rates of CO and H_2. The NO formation rate is seven times higher in the HTP case due to the higher temperatures. This observations can also be made by comparing NO concentrations, given in Figure 6.18. The concentrations predicted for the HTP case are two times those predicted for the HT case. Figure 6.19 compares the velocity magnitude predictions. Both cases give similar flow patterns, though the HT case gives a greater velocity magnitude.

(a) 1 bar

(b) 7 bar
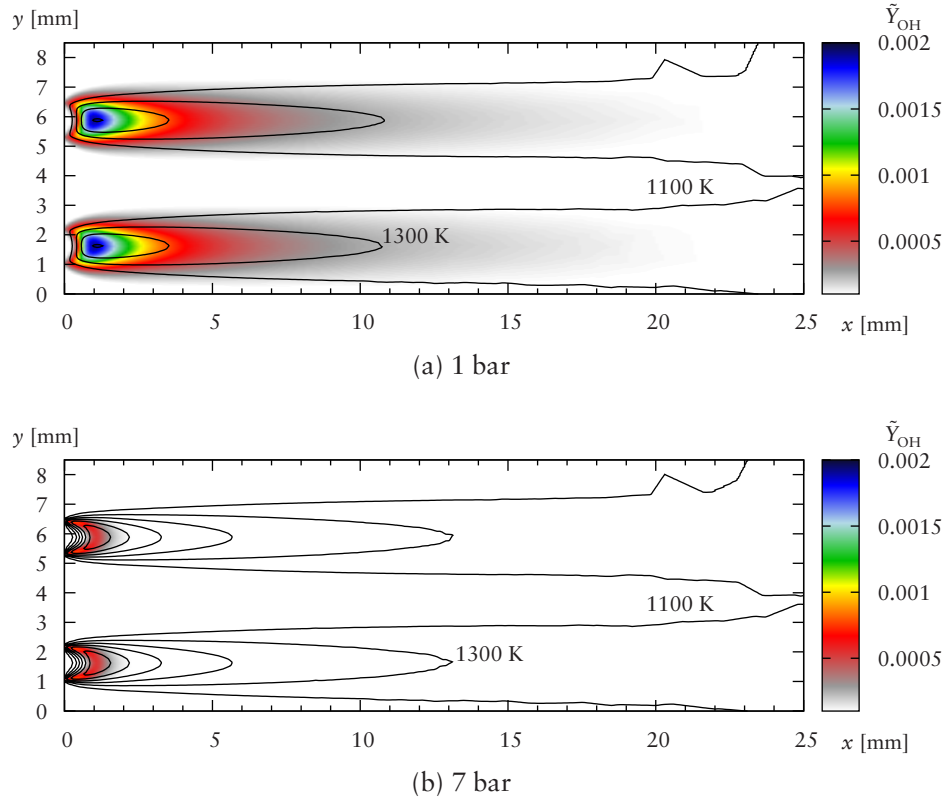
Figure 6.16: Temperature, $\tilde{T}$, contour plot downstream of the burner for DATUM condition at atmospheric and high pressures. Temperature contours indicated at 100 K intervals, starting at 1000 K. The predicted OH mass fraction, $\tilde{Y}_{OH}$, is also shown as a colour-map. The fuel slots extend from 1.126 to 2.126 mm and from 5.378 to 6.378 mm.
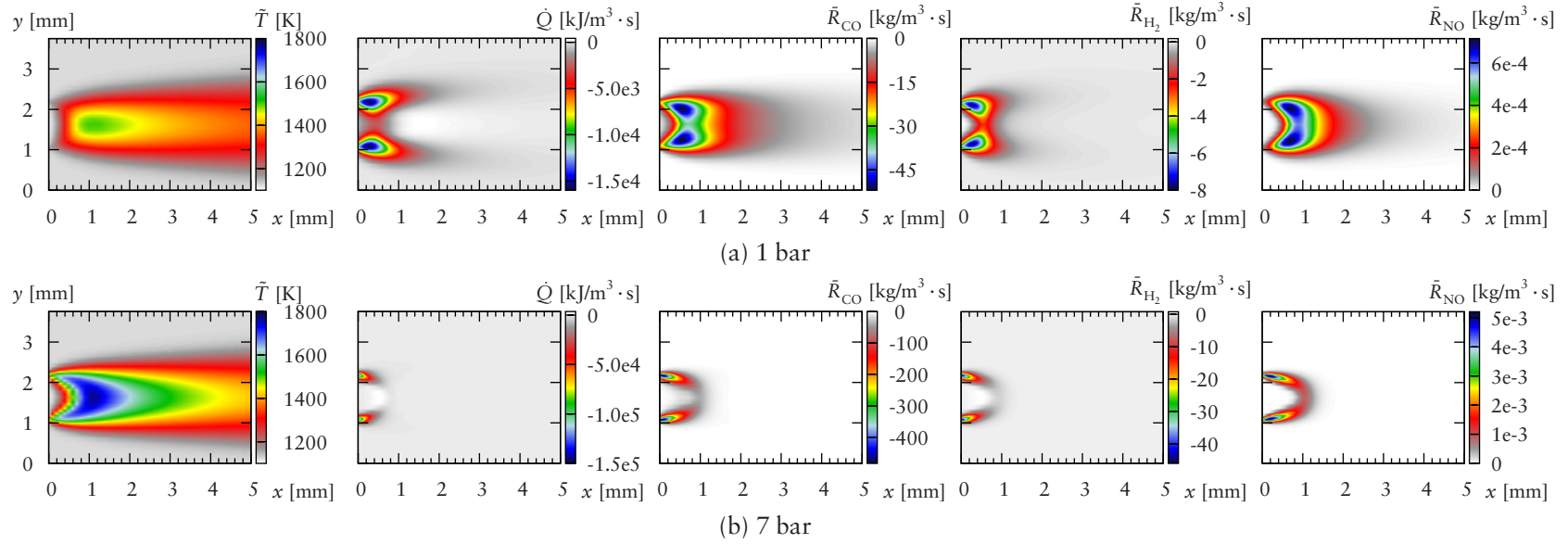
Figure 6.17: Temperature, $\tilde{T}$ [K], heat release, $\dot{Q}$ [kJ/m$^3\cdot$s], and net rates of formation/destruction of CO, H$_2$ and NO, $\bar{R}_\alpha$ [kg/m$^3\cdot$s], in the near-field region for DATUM condition at atmospheric and high pressures shown as a colour-map. The fuel slot extends from 1.126 to 2.126 mm.

(a) 1 bar

(b) 7 bar
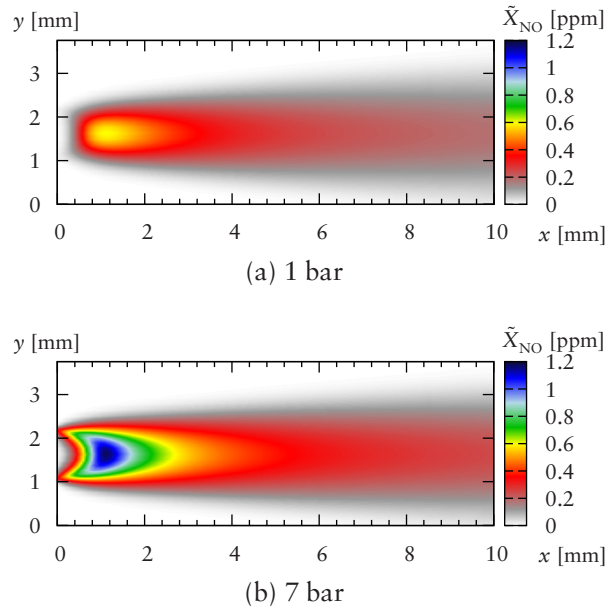
Figure 6.18: Plots of NO concentration, $\tilde{X}_{NO}$ [ppm], for DATUM condition at atmospheric and high pressures. The fuel slot extends from 1.126 to 2.126 mm.

(a) 1 bar

(b) 7 bar
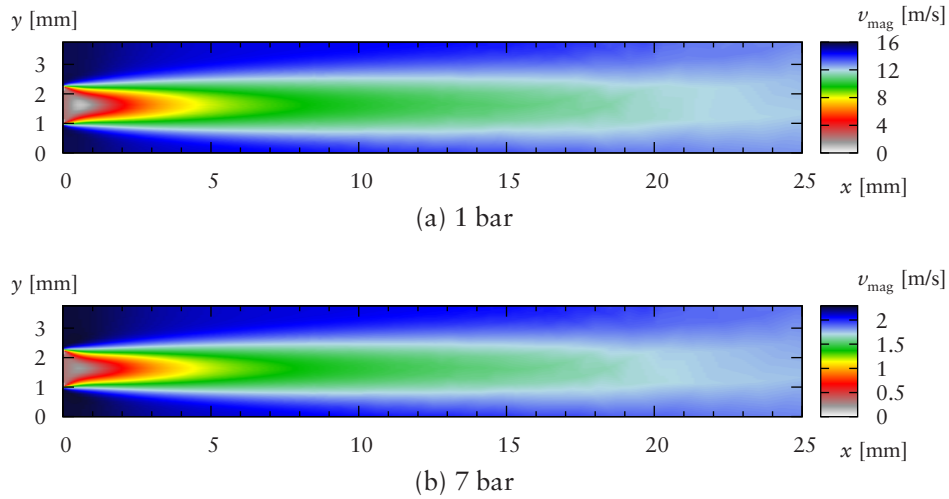
Figure 6.19: Plots of velocity magnitude, v_{mag} [m/s], for DATUM condition at atmospheric and high pressures. The fuel slot extends from 1.126 to 2.126 mm.

Table 6.3: Comparison of NO$_x$ predictions with 6- and 7-step reduced mechanisms.

			6-step		7-step		
Table	Condition	p [bar]	$\tilde{X}_{NO}$ [ppm]	$\tilde{T}$ [K]	$\tilde{X}_{NO_x}$ [ppm]	%NO$_2$[a]	$\tilde{T}$ [K]
C.2	1	1	8.62	1504.1	9.58	0.3	1504.1
		7	14.2	1425.9	13.7	1.1	1425.9
C.4	DATUM	1	0.0865	1216.5	0.0879	2.2	1216.5
		7	0.104	1212.8	0.109	4.8	1212.7

[a] The percentage contribution of NO$_2$ to the total $\tilde{X}_{NO}$ value.

6.7 NO$_2$ Contribution

The 7-step mechanism described in Chapter 4 is applied to both atmospheric and high temperature inlet conditions at atmospheric and high pressures. The total NO$_x$ is defined as $\tilde{X}_{NO_x} = \tilde{X}_{NO} + \tilde{X}_{NO_2}$ on a dry basis for the 7-step mechanism and as $\tilde{X}_{NO_x} = \tilde{X}_{NO}$ for the 6-step mechanism. Table 6.3 gives a comparison of the predicted NO$_x$ levels and the percentage contribution of NO$_2$. It is observed that the difference between the 6- and 7-step mechanisms, in terms of total NO$_x$ values, is small. The contribution of NO$_2$ is also shown to be small (< 5%) for both atmospheric and high pressures. The contribution of NO$_2$ increases with pressure, as expected [113]. Any small differences between the 6- and 7-step mechanisms can also be explained by the highly sensitive nature of NO$_x$ predictions to the temperature, as discussed above.

6.8 Summary

The reduced chemical mechanism developed in Chapter 4 is used with the realizable k-ε turbulence closure and laminar chemistry, and is applied to the off-gas burner. The con-

ditions employed in atmospheric and high temperature experiments are simulated using the model developed. The findings indicate that the correct prediction of the flow field (velocities, mixture fraction, species mass fractions and temperature, and their fluctuations) is critical for predicting the temperature and species fields. For the off-gas burner operating at the presented conditions, the use of laminar finite-rate chemistry appears to be justified. However, should the Reynolds number of the flow issuing from the slots increase due to possible design changes, the use of laminar finite-rate chemistry may lead to inaccuracies as the turbulence-chemistry interactions become increasingly important. However, the general procedure using the EDC and SLFM, detailed in Chapter 5, is still highly appropriate if the turbulence levels are high enough to sustain a flame.

The use of the reduced mechanism demonstrates that sensitivity tests can be made for equivalence ratio, bulk velocity, $H_2 : CO$ ratio etc. requiring more modest computational resources and less time than for full chemistry. Trends for CO and NO are predicted qualitatively over the ranges investigated, however there are discrepancies with CO predictions. Further work, both computational and experimental, is required to identify the source of the CO shift experienced in the equivalence ratio sweep. The extension of the model to high temperatures and pressures shows that its use is feasible as a design tool for further off-gas burner optimization. The NO_x and CO emissions predicted at high pressure are well within the design targets set. The agreement at atmospheric pressure is sufficient to support the model's use at high pressures. This lends confidence to the success of the burner operating at the actual operating conditions.

Chapter 7

Conclusions

The goal of this project was to develop a computational model of the Rolls-Royce Fuel Cell Systems SOFC hybrid off-gas burner. The previous chapters described the development and validation of a reduced chemical mechanism for $H_2/CO/N_2$ flames; including testing of the mechanism, along with the underlying turbulence closures and reaction rate models, against well-characterized turbulent flames. The relevant modelling methods have been applied to the SOFC hybrid off-gas burner. The main conclusions from the model development and application to the off-gas burner are summarized next, followed by suggestions for future work.

7.1   Summary

Chapter 4 set out to determine if a reduced $H_2/CO/N_2$ mechanism could reasonably approximate a full mechanism when applied to an opposed-flow laminar diffusion flame at ATP and HTP conditions, with dilute reformate gases.

- A 6-step mechanism including NO chemistry from GRI-Mech 2.11 was tested against the full starting and GRI-Mech 3.0 mechanisms at both ATP and HTP

conditions. Good agreement is found in both cases for major species and temperature profiles.

- A 7-step mechanism, including NO_2, was tested against the 6-step and starting mechanisms. Good agreement is found for all major species and temperature profiles, as well as NO_x, over a range of flame stretch values.

- Overall, it is observed that the 6- and 7-step reduced mechanisms developed give good approximations of the starting mechanism and capture all the relevant kinetics for both ATP and HTP conditions for stretched laminar diffusion flames.

- The results are comparable to the GRI-Mech 3.0 mechanism for CH_4.

- The 6-step reduced mechanism decreases the number of scalars required by a factor of three. A corresponding reduction in computation time is achieved for opposed-flow flame calculations.

These findings give confidence for the application of the mechanism to turbulent combustion modelling.

In expectation of significant turbulence-chemistry interaction in the experimental off-gas burner, the reduced mechanism was applied to two turbulent syngas flames which have been well-characterized by experiment [4, 28]. This involved developing an interface between CHEMKIN and FLUENT, discussed in Chapter 5.

- Two turbulence closure models were used; the relatively simple realizable k-ε closure and the more complex Reynolds Stress (RS) closure. It is demonstrated that the two closures give comparable results for the flames studied. The simpler realizable k-ε closure requires only two scalars compared to the RS closure's six, reducing computational requirements.

- The two reaction rate closures used, the EDC and the SLFM, give slightly different results. The SLFM model, although faster than the EDC in the CFD calculations, requires the prior generation of individual flamelet libraries (each containing ap-

proximately 12 flamelets) for each fuel and oxidizer combination. This is not a trivial task. The EDC, on the other hand, requires no such pre-processing, so its use for parametric studies would seem to be preferable.

- Standard model constants were used. With detailed prior knowledge of the flow and scalar fields the model constants can be altered to match the centreline mixture fraction profile and give a subsequent improvement in predictive capabilities.

- The NO and CO predictions are in general agreement to experiment once model constants are adjusted. Taking into account heat loss due to radiation further improves both the temperature and NO predictions for the EDC.

The ease of inclusion of preferential diffusion effects in the EDC suggests this approach has the advantage for $H_2/CO/N_2$ flames where H_2 diffusion may affect flame stabilization. It has been observed that tuning the constants in the realizable k-ε and RS turbulence closures is necessary. In general, a good procedure could be to tune the model on a Sandia flame with similar flow characteristics before application to the off-gas burner. The combination of reduced mechanism, realizable k-ε turbulence closure, and either the EDC or SLFM reaction rate models gives good predictions for these syngas flames. Its use for other syngas flames, and its adaptation to other turbulent combustion models, would seem appropriate.

7.2 Application to Off-Gas Burner

The general procedure developed in Chapters 4 and 5 was applied to the SOFC hybrid off-gas burner. The realizable k-ε turbulence closure was used with standard model constants. Turbulence-chemistry interaction has been ignored due to the failure of the EDC and SLFM to predict a stable flame at the low levels of turbulence experienced in the near-field; laminar finite-rate kinetics with the reduced mechanism are used. Alteration

of boundary conditions to give a stable flame was not possible due to the scope of the uncertainty of their values.

- The results obtained give general agreement with the experimental results available.

- However, there is a high degree of uncertainty with the experimental results, particularly at high temperature conditions.

- The general trends for CO and NO are captured.

- The extension of the reduced mechanism to high temperatures and pressures gives the expected behaviour, and indicates that the burner performs within the intended design specifications for CO and NO emissions.

- The use of the reduced mechanism (through either the laminar finite-rate, EDC or SLFM approaches) with the realizable k-ε turbulence closure gives a fast and accurate design tool for use with syngas flames.

7.3   Future Work

To improve on the model developed, a number of studies could be made involving both experimental and computational work. Firstly, further information from experiments would be very useful:

- Detailed experimental measurements of the off-gas burner flow field, including velocity components and their fluctuations, species (including OH and CO, for example), and temperature. A mixture fraction field could then be reconstructed from the species values, which would allow direct comparison to calculated values.

- Determination of actual inlet conditions for HT conditions where a catalyst is used to generate the input gases for the off-gas burner. Gas sampling could be used at the inlet to the burner to provide more accurate boundary conditions for

the simulations.

- Temperature measurements at the face of the burner, and the individual slots. This would allow heat transfer to the inlet gases to be included in future simulations.

Secondly, the numerical model could be extended based on the improved experimental results:

- With detailed turbulence measurements, more accurate turbulence inlet parameters could be set, and comparison of downstream values could be made.

- The model could be extended to three-dimensions to include the effect of any entrainment or flow angle variation.

- The reduced mechanism could be incorporated into more advanced combustion models, such as the CMC approach.

The model calibration can be conducted on a flame sharing some of the flow characteristics with the off-gas burner. Then the model becomes predictive for the off-gas burner. The goal of any future work in turbulent combustion modelling should be to produce general models that work for various flow and flame configurations and conditions, to increase the use of CFD as a predictive tool.

Appendix A

Numerical Details

The methods used to calculate physical properties, such as density and viscosity, in CHEMKIN [58] and FLUENT [39] are given below. In addition, an overview of the EDC is given.

A.1   Physical Properties

For temperature-dependent thermodynamic data the following general polynomial fit is used [39, 58];

$$\phi(T) = A_1 + A_2 T + A_3 T^2 + \ldots A_i T^{i-1}, \tag{A.1}$$

where A_i are prescribed coefficients.

Density

The mean mass density is calculated using the ideal gas law;

$$\rho = \frac{p}{R_u T \sum\limits_{\alpha} \frac{Y_\alpha}{W_\alpha}}. \tag{A.2}$$

Viscosity

Single component viscosities are calculated using kinetic theory, given by [58]

$$\mu_\alpha = 2.67 \times 10^{-6} \frac{\sqrt{W_\alpha T}}{\sigma_{\mathrm{LJ},\alpha}^2 \Omega_{\mu,\alpha}}, \tag{A.3}$$

where $\Omega_{\mu,\alpha}$ is a function of the reduced temperature, $\Omega_{\mu,\alpha} = \Omega_{\mu,\alpha}(T_\alpha^*)$, and

$$T_\alpha^* = \frac{T}{(\epsilon_{\mathrm{LJ},\alpha}/k_B)}. \tag{A.4}$$

The term $\epsilon_{\mathrm{LJ},\alpha}/k_B$ is viewed as a Lennard-Jones potential energy parameter. Assuming an ideal gas [118], the mixture viscosity is given by

$$\mu = \sum_{\alpha=1}^{n_s} \frac{X_\alpha \mu_\alpha}{\sum\limits_{\beta} X_\alpha \phi_{\alpha\beta}}, \tag{A.5}$$

where

$$\phi_{\alpha\beta} = \frac{\left[1 + \left(\frac{\mu_\alpha}{\mu_\beta}\right)^{1/2} \left(\frac{W_\beta}{W_\alpha}\right)^{1/4} \right]^2}{\left[8 \left(1 + \frac{W_\alpha}{W_\beta} \right) \right]^{1/2}}. \tag{A.6}$$

Thermal Conductivity

For the thermal conductivity of single species, λ_α, kinetic theory is used;

$$\lambda_\alpha = \frac{15}{4}\frac{R}{W_\alpha}\mu_\alpha\left[\frac{4}{15}\frac{c_{p,\alpha}W_\alpha}{R_u}+\frac{1}{3}\right].$$
(A.7)

For a mixture, an ideal gas is assumed and the thermal conductivity is calculated using [77]

$$\lambda = \sum_{\alpha=1}^{n_s}\frac{X_\alpha\lambda_\alpha}{\sum\limits_\beta X_\alpha\phi_{\alpha\beta}},$$
(A.8)

where $\phi_{\alpha\beta}$ is given by Equation (A.6).

Mass Diffusion

The species mass diffusion is calculated by kinetic theory using

$$D_\alpha^M = \frac{1-X_\alpha}{\sum\limits_{\beta,\,\beta\neq\alpha}\left(X_\beta/\mathcal{D}_{\alpha\beta}\right)}.$$
(A.9)

The binary mass diffusion coefficient, $\mathcal{D}_{\alpha\beta}$, is calculated using the Chapman-Enskog formula;

$$\mathcal{D}_{\alpha\beta} = 0.00188\frac{\left[T^3\left(\frac{1}{W_\alpha}+\frac{1}{W_\beta}\right)\right]^{1/2}}{p_{\text{abs}}\sigma_{\alpha\beta}^2\Omega_D},$$
(A.10)

where Ω_D is a function of the reduced temperature, $\Omega_D = \Omega_D(T_D^*)$, and

$$T_D^* = \frac{T}{(\epsilon_{LJ}/k_B)_{\alpha\beta}}. \tag{A.11}$$

$(\epsilon_{LJ}/k_B)_{\alpha\beta}$ for the mixture is the geometric average given by

$$(\epsilon_{LJ}/k_B)_{\alpha\beta} = \sqrt{(\epsilon_{LJ}/k_B)_\alpha (\epsilon_{LJ}/k_B)_\beta}. \tag{A.12}$$

For a binary mixture, $\sigma_{\alpha\beta}$ is the arithmetic average of the individual values of σ_{LJ} given by

$$\sigma_{\alpha\beta} = \frac{1}{2}(\sigma_{LJ,\alpha} + \sigma_{LJ,\beta}). \tag{A.13}$$

Thermal Diffusion

The species thermal (Soret) diffusion is calculated using

$$D_\alpha^T = -2.59 \times 10^{-7} T^{0.659} \left[\frac{W_\alpha^{0.511} X_\alpha}{\sum\limits_\alpha W_\alpha^{0.511} X_\alpha} - Y_\alpha \right] \cdot \left[\frac{\sum\limits_\alpha W_\alpha^{0.511} X_\alpha}{\sum\limits_\alpha W_\alpha^{0.489} X_\alpha} \right]. \tag{A.14}$$

A.2   Eddy Dissipation Concept Derivation

The general procedure for implementing EDC in CFD codes is to insert an extra calculation step when calculating mass fractions, temperatures, densities and viscosities [46]:

  (i) For adiabatic conditions, the enthalpy in fine-scales is set as being equal to the enthalpy in the surrounding fluid.

 (ii) Compute fine-structure state using chemistry (integration of Equation (3.53) using calculated reaction rates, see Chapter 4).

(iii) Compute composition of surrounding fluid, ψ°.

(iv) Compute temperature of surrounding fluid.

 (v) Compute density of surrounding fluid.

(vi) Compute viscosity of surrounding fluid.

(vii) Determine mean temperature, density and viscosity from the fine-structure and surrounding states.

This additional calculation loop is carried out at a pre-defined frequency; every n iterations of the 'outside' loop. For steady-state calculations previous work has identified that n can be very large without affecting the final solution or creating numerical difficulties [46]. This has the benefit of decreasing the computational time by a significant amount, as the solution of the PSR reactor (with complex chemistry) can take a considerable time. In the present work, the calculation procedure is carried out at every iteration, and an alternative method of reducing the computational time (the ISAT algorithm, Section 3.5.2) is used.

The Eddy Dissipation Concept [38, 73], outlined in Section 3.2.2, uses a cascade model to link the large scales of turbulence to the fine-scales where combustion generally takes place. A description of the derivation, taken from Ertesvåg and Magnussen [38], is presented below. The input to the cascade is the turbulent kinetic energy, $\tilde{k}$, and related length and time scales (through the dissipation rate $\tilde{\varepsilon}$). The large eddy velocity scale, $u^{\wr}$ (where the superscript '$\wr$' indicates the large scale), is related to the turbulent kinetic energy through

$$u^{\wr} = \sqrt{\frac{2}{3}\tilde{k}}. \tag{A.15}$$

It can be related to a strain-rate, $\Omega^\imath$, by

$$\Omega^\imath = \frac{u^\imath}{L^\imath}, \tag{A.16}$$

where $L^\imath$ is the large eddy length scale. These quantities reflect the energy contained at the large scales as well as the smaller scales. For the next energy level (smaller in size), the characteristic scales are $u^{\imath\imath}$, $L^{\imath\imath}$ and $\Omega^{\imath\imath} = 2\Omega^\imath$. These reflect the energy in this level and all smaller eddies. In this way, a general relationship between one level and the next can be formed by

$$\Omega_n = 2\Omega_{n-1}, \tag{A.17}$$

u_n, and L_n for the nth level.

The smallest eddies (where the superscript '$*$' indicates the fine-scales) are of the same order as the Kolmogorov scales; $L^* \approx \eta$, $u^* \approx u_\eta$ and $1/\Omega^* = \tau_\eta$. The transfer of work from the mean flow to the large eddy turbulent scales, $w^\imath$, is related to the production of $\tilde{k}$ by

$$w^\imath = \widetilde{u_i'' u_j''} \frac{\partial \tilde{u}_j}{\partial x_i}. \tag{A.18}$$

In a similar fashion, the transfer of work from the first to the second level, $w^{\imath\imath}$, is modelled by [38]

$$w^{\imath\imath} = \frac{3}{2} C_\alpha 2 u^{\imath\imath 2} \Omega^\imath = \frac{3}{2} C_\alpha u^{\imath\imath 2} \Omega^{\imath\imath} \tag{A.19}$$

using Equation (A.17), where C_α is a model constant.

The transfer of thermal energy from the first level, q^ι, is modelled as

$$q^\iota = C_\beta \nu \Omega^{\iota 2},$$ (A.20)

where C_β is a model constant and ν is the kinematic viscosity. The dissipation of the energy, ε, is expressed as the sum of transfer of work from the first to second levels and the thermal energy transfer; $\varepsilon = q^\iota + w^{\iota\iota}$. If the transfer from one level to another is assumed to be the same for all subsequent levels down to the fine-scales, a general equations for the nth level can be formed;

$$w_n = \frac{3}{2} C_\alpha \Omega_n u_n^2,$$ (A.21)

$$q_n = C_\beta \nu \Omega_n^2,$$ (A.22)

and the balance is given by

$$w_n = q_n + w_{n+1}.$$ (A.23)

For the fine-scale levels $\Omega^* = q^*$ and

$$w^* = \frac{3}{2} C_\alpha \Omega^* u^{*2}$$ (A.24)

$$q^* = C_\beta \nu^* \Omega^{*2}$$ (A.25)

For large Re, ε is small compared to w. For small values of n, q_n is small compared to w_n and $w_n \approx w_{n+1}$. This results in

$$\frac{1}{2} u_n^2 = u_{n+1}^2.$$ (A.26)

Thus, for $n = 2$

$$\frac{1}{2}u''^2 = u'''^2, \tag{A.27}$$

and the transfer of work from the second to third levels can be written, using Equation (A.19), as

$$\begin{aligned}
w'' &= \frac{3}{2}C_\alpha 2u''^2 \Omega' \\
&= C_\alpha \frac{3}{2}u'^2 \Omega' \\
&= C_\alpha \Omega' \tilde{k}. \tag{A.28}
\end{aligned}$$

The value of C_α is determined by combining Equation (A.19) with $u''^2 \approx \frac{1}{2}u'^2$ and Equation (A.16) giving

$$w'' = \frac{3}{2}C_\alpha \frac{u'''^3}{L'}. \tag{A.29}$$

Introducing the turbulent viscosity, $\nu_t = u'L'$, leads to

$$w'' = \frac{3}{2}C_\alpha \frac{u'^4}{\nu_t} \approx \varepsilon, \tag{A.30}$$

as $\varepsilon = q' + w''$ and q' is assumed to be negligible compared to w''. Using $\tilde{k} = \frac{3}{2}u'^2$, u'^4 can be written as

$$\left(\frac{2}{3}\tilde{k}\right)^2 = u'^4. \tag{A.31}$$

Substitution of Equation (A.31) into Equation (A.30) gives

$$\nu_t = \frac{2}{3} C_\alpha \frac{\tilde{k}^2}{\varepsilon},$$

(A.32)

which is proportional to Equation (3.6), giving

$$C_\alpha = \frac{3}{2} C_\mu = 0.135, \qquad \text{as } C_\mu = 0.09.$$

(A.33)

To determine the length and velocity scales at the fine-scale level it is assumed that $\varepsilon = \frac{4}{3} q^*$ [38]. Using Equation (A.25) and $\Omega^* = u^*/L^*$ gives

$$\begin{aligned}
\varepsilon &= \frac{4}{3} C_\beta \nu^* \Omega^{*2} \\
&= \frac{4}{3} C_\beta \nu^* \frac{u^{*2}}{L^{*2}}.
\end{aligned}$$

(A.34)

The balance at the last level is given by

$$\begin{aligned}
\varepsilon &= \frac{4}{3} w^* = 2 C_\alpha \Omega^* u^{*2} \\
&= 2 C_\alpha \frac{u^{*3}}{L^*}.
\end{aligned}$$

(A.35)

To determine u^*, Equation (A.35) is re-arranged to get L^* and substituted into Equation (A.34);

$$u^* = \left(\frac{C_\beta}{3 C_\alpha^2} \right)^{1/4} (\nu^* \varepsilon)^{1/4}.$$

(A.36)

To determine L^*, Equation (A.34) is cubed and Equation (A.35) is squared. Substitution of Equation (A.35) into Equation (A.34) gives

$$L^* = \frac{2}{3}\left(\frac{3C_\beta^3}{C_\alpha^2}\right)^{1/4}\left(\frac{v^{*3}}{\varepsilon}\right)^{1/4}. \tag{A.37}$$

Values for γ^* and $\dot{m}^*$, used in Section 3.2.2, are determined using

$$\gamma^* = \frac{u^*}{u^2} \tag{A.38}$$

$$\dot{m}^* = 2\frac{u^*}{L^*}. \tag{A.39}$$

Appendix B

Kinetic Mechanism

This appendix gives details of the starting and reduced kinetic mechanisms for $H_2/CO/N_2$ flames studied in Chapters 4–6.

B.1 $H_2/CO/N_2$ Mechanism

Details of the starting mechanism, taken from Davis et al. [30] and GRI-Mech 2.11 [13], are given in Tables B.1 and B.2. This starting mechanism is used to develop a reduced mechanism in Chapter 4.

Table B.1: Starting reaction mechanism; Reactions 1–38 from Davis et al. [30] and Reactions 39–116 from Bowman et al. [13]. Reaction rate coefficients in form $k_f = A_r T^{\beta_r} \exp\left(-E_r/R_u T\right)$ with units of mol, cm, s, cal.

No.	Reaction	A_r	β_r	E_r
1	$H + O_2 \rightleftharpoons O + OH$	2.644e16	−0.6707	17041.00
2	$O + H_2 \rightleftharpoons H + OH$	4.589e04	2.700	6260.00
3	$OH + H_2 \rightleftharpoons H + H_2O$	1.734e08	1.510	3430.00
4	$OH + OH \rightleftharpoons O + H_2O$	3.973e04	2.400	−2110.00
5[a]	$H + H + M \rightleftharpoons H_2 + M$	1.780e18	−1.000	0.00
6	$H + H + H_2 \rightleftharpoons H_2 + H_2$	9.000e16	−0.600	0.00
7	$H + H + H_2O \rightleftharpoons H_2 + H_2O$	5.624e19	−1.250	0.00
8	$H + H + CO_2 \rightleftharpoons H_2 + CO_2$	5.500e20	−2.000	0.00
9[a]	$H + OH + M \rightleftharpoons H_2O + M$	4.400e22	−2.000	0.00
10[a]	$O + H + M \rightleftharpoons OH + M$	9.428e18	−1.000	0.00
11[a]	$O + O + M \rightleftharpoons O_2 + M$	1.200e17	−1.000	0.00
12[a]	$H + O_2 \rightleftharpoons HO_2$	5.116e12	0.440	0.00
13	$H_2 + O_2 \rightleftharpoons HO_2 + H$	5.916e05	2.433	53502.00
14[a]	$OH + OH \rightleftharpoons H_2O_2$	1.110e14	−0.370	0.00
15	$HO_2 + H \rightleftharpoons O + H_2O$	3.970e12	0.000	671.00
16	$HO_2 + H \rightleftharpoons OH + OH$	7.485e13	0.000	295.00
17	$HO_2 + O \rightleftharpoons OH + O_2$	4.000e13	0.000	0.00
18[*]	$HO_2 + OH \rightleftharpoons O_2 + H_2O$	2.375e13	0.000	−500.00
19[*]	$HO_2 + OH \rightleftharpoons O_2 + H_2O$	1.000e16	0.000	17330.00
20[*]	$HO_2 + HO_2 \rightleftharpoons O_2 + H_2O_2$	1.300e11	0.000	−1630.00
21[*]	$HO_2 + HO_2 \rightleftharpoons O_2 + H_2O_2$	3.658e14	0.000	12000.00
22	$H_2O_2 + H \rightleftharpoons HO_2 + H_2$	6.050e06	2.000	5200.00
23	$H_2O_2 + H \rightleftharpoons OH + H_2O$	2.410e13	0.000	3970.00
24	$H_2O_2 + O \rightleftharpoons OH + HO_2$	9.630e06	2.000	3970.00
25[*]	$H_2O_2 + OH \rightleftharpoons HO_2 + H_2O$	2.000e12	0.000	427.00
26[*]	$H_2O_2 + OH \rightleftharpoons HO_2 + H_2O$	2.670e41	−7.000	37600.00
27[a]	$CO + O \rightleftharpoons CO_2$	1.362e10	0.000	2384.00
28[*]	$CO + OH \rightleftharpoons CO_2 + H$	8.000e11	0.140	7352.00
29[*]	$CO + OH \rightleftharpoons CO_2 + H$	8.784e10	0.030	−16.00
30	$CO + O_2 \rightleftharpoons CO_2 + O$	1.119e12	0.000	47700.00
31	$CO + HO_2 \rightleftharpoons CO_2 + OH$	3.010e13	0.000	23000.00
32	$HCO + H \rightleftharpoons CO + H_2$	1.200e14	0.000	0.00
33	$HCO + O \rightleftharpoons CO + OH$	3.000e13	0.000	0.00
34	$HCO + O \rightleftharpoons CO_2 + H$	3.000e13	0.000	0.00
35	$HCO + OH \rightleftharpoons CO + H_2O$	3.020e13	0.000	0.00
36[a]	$HCO + M \rightleftharpoons CO + H + M$	1.870e17	−1.000	17000.00
37	$HCO + H_2O \rightleftharpoons CO + H + H_2O$	2.244e18	−1.000	17000.00
38	$HCO + O_2 \rightleftharpoons CO + HO_2$	1.204e10	0.807	−727.00
39	$N + NO \rightleftharpoons N_2 + O$	3.500e13	0.000	330.00
40	$N + O_2 \rightleftharpoons NO + O$	2.650e12	0.000	6400.00

[*] Duplicate reactions.
[a] Third-body efficiencies and pressure-dependent reaction rates are given in Table B.2.

Table B.1: Starting reaction mechanism; Reactions 1–38 from Davis et al. [30] and Reactions 39–116 from Bowman et al. [13]. Reaction rate coefficients in form $k_f = A_r T^{\beta_r} \exp(-E_r/R_u T)$ with units of mol, cm, s, cal. (continued).

No.	Reaction	A_r	β_r	E_r
41	$N + OH \rightleftharpoons NO + H$	7.333e13	0.000	1120.00
42	$N_2O + O \rightleftharpoons N_2 + O_2$	1.400e12	0.000	10810.00
43	$N_2O + O \rightleftharpoons 2\,NO$	2.900e13	0.000	23150.00
44	$N_2O + H \rightleftharpoons N_2 + OH$	4.400e14	0.000	18880.00
45	$N_2O + OH \rightleftharpoons N_2 + HO_2$	2.000e12	0.000	21060.00
46[a]	$N_2O \rightleftharpoons N_2 + O$	1.300e11	0.000	59620.00
47	$HO_2 + NO \rightleftharpoons NO_2 + OH$	2.110e12	0.000	−480.00
48[a]	$NO + O + M \rightleftharpoons NO_2 + M$	1.060e20	−1.410	0.00
49	$NO_2 + O \rightleftharpoons NO + O_2$	3.900e12	0.000	−240.00
50	$NO_2 + H \rightleftharpoons NO + OH$	1.320e14	0.000	360.00
51	$NH + O \rightleftharpoons NO + H$	5.000e13	0.000	0.00
52	$NH + H \rightleftharpoons N + H_2$	3.200e13	0.000	330.00
53	$NH + OH \rightleftharpoons HNO + H$	2.000e13	0.000	0.00
54	$NH + OH \rightleftharpoons N + H_2O$	2.000e09	1.200	0.00
55	$NH + O_2 \rightleftharpoons HNO + O$	4.610e05	2.000	6500.00
56	$NH + O_2 \rightleftharpoons NO + OH$	1.280e06	1.500	100.00
57	$NH + N \rightleftharpoons N_2 + H$	1.500e13	0.000	0.00
58	$NH + H_2O \rightleftharpoons HNO + H_2$	2.000e13	0.000	13850.00
59	$NH + NO \rightleftharpoons N_2 + OH$	2.160e13	−0.230	0.00
60	$NH + NO \rightleftharpoons N_2O + H$	4.160e14	−0.450	0.00
61	$NH_2 + O \rightleftharpoons OH + NH$	7.000e12	0.000	0.00
62	$NH_2 + O \rightleftharpoons H + HNO$	4.600e13	0.000	0.00
63	$NH_2 + H \rightleftharpoons NH + H_2$	4.000e13	0.000	3650.00
64	$NH_2 + OH \rightleftharpoons NH + H_2O$	9.000e07	1.500	−460.00
65	$NNH \rightleftharpoons N_2 + H$	3.300e08	0.000	0.00
66[a]	$NNH + M \rightleftharpoons N_2 + H + M$	1.300e14	−0.110	4980.00
67	$NNH + O_2 \rightleftharpoons HO_2 + N_2$	5.000e12	0.000	0.00
68	$NNH + O \rightleftharpoons OH + N_2$	2.500e13	0.000	0.00
69	$NNH + O \rightleftharpoons NH + NO$	7.000e13	0.000	0.00
70	$NNH + H \rightleftharpoons H_2 + N_2$	5.000e13	0.000	0.00
71	$NNH + OH \rightleftharpoons H_2O + N_2$	2.000e13	0.000	0.00
72[a]	$H + NO + M \rightleftharpoons HNO + M$	8.950e19	−1.320	740.00
73	$HNO + O \rightleftharpoons NO + OH$	2.500e13	0.000	0.00
74	$HNO + H \rightleftharpoons H_2 + NO$	4.500e11	0.720	660.00
75	$HNO + OH \rightleftharpoons NO + H_2O$	1.300e07	1.900	−950.00
76	$HNO + O_2 \rightleftharpoons HO_2 + NO$	1.000e13	0.000	13000.00
77	$CN + O \rightleftharpoons CO + N$	7.700e13	0.000	0.00
78	$CN + OH \rightleftharpoons NCO + H$	4.000e13	0.000	0.00
79	$CN + H_2O \rightleftharpoons HCN + OH$	8.000e12	0.000	7460.00
80	$CN + O_2 \rightleftharpoons NCO + O$	6.140e12	0.000	−440.00

[*] Duplicate reactions.
[a] Third-body efficiencies and pressure-dependent reaction rates are given in Table B.2.

Table B.1: Starting reaction mechanism; Reactions 1–38 from Davis et al. [30] and Reactions 39–116 from Bowman et al. [13]. Reaction rate coefficients in form $k_f = A_r T^{\beta_r} \exp(-E_r/R_u T)$ with units of mol, cm, s, cal. (continued).

No.	Reaction	A_r	β_r	E_r
81	$CN + H_2 \rightleftharpoons HCN + H$	2.100e13	0.000	4710.00
82	$NCO + O \rightleftharpoons NO + CO$	2.350e13	0.000	0.00
83	$NCO + H \rightleftharpoons NH + CO$	5.400e13	0.000	0.00
84	$NCO + OH \rightleftharpoons NO + H + CO$	2.500e12	0.000	0.00
85	$NCO + N \rightleftharpoons N_2 + CO$	2.000e13	0.000	0.00
86	$NCO + O_2 \rightleftharpoons NO + CO_2$	2.000e12	0.000	20000.00
87[a]	$NCO + M \rightleftharpoons N + CO + M$	8.800e16	–0.500	48000.00
88	$NCO + NO \rightleftharpoons N_2O + CO$	2.850e17	–1.520	740.00
89	$NCO + NO \rightleftharpoons N_2 + CO_2$	5.700e18	–2.000	800.00
90[a]	$HCN + M \rightleftharpoons H + CN + M$	1.040e29	–3.300	126600.00
91	$HCN + O \rightleftharpoons NCO + H$	1.107e04	2.640	4980.00
92	$HCN + O \rightleftharpoons NH + CO$	2.767e03	2.640	4980.00
93	$HCN + O \rightleftharpoons CN + OH$	2.134e09	1.580	26600.00
94	$HCN + OH \rightleftharpoons HOCN + H$	1.100e06	2.030	13370.00
95	$HCN + OH \rightleftharpoons HNCO + H$	4.400e03	2.260	6400.00
96	$HCN + OH \rightleftharpoons NH_2 + CO$	1.600e02	2.560	9000.00
97[a]	$H + HCN + M \rightleftharpoons H_2CN + M$	1.400e26	–3.400	1900.00
98	$HCNN + O \rightleftharpoons CO + H + N_2$	2.200e13	0.000	0.00
99	$HCNN + O \rightleftharpoons HCN + NO$	2.000e12	0.000	0.00
100	$HCNN + O_2 \rightleftharpoons O + HCO + N_2$	1.200e13	0.000	0.00
101	$HCNN + OH \rightleftharpoons H + HCO + N_2$	1.200e13	0.000	0.00
102	$HNCO + O \rightleftharpoons NH + CO_2$	9.800e07	1.410	8500.00
103	$HNCO + O \rightleftharpoons HNO + CO$	1.500e08	1.570	44000.00
104	$HNCO + O \rightleftharpoons NCO + OH$	2.200e06	2.110	11400.00
105	$HNCO + H \rightleftharpoons NH_2 + CO$	2.250e07	1.700	3800.00
106	$HNCO + H \rightleftharpoons H_2 + NCO$	1.050e05	2.500	13300.00
107	$HNCO + OH \rightleftharpoons NCO + H_2O$	4.650e12	0.000	6850.00
108	$HNCO + OH \rightleftharpoons NH_2 + CO_2$	1.550e12	0.000	6850.00
109[a]	$HNCO + M \rightleftharpoons NH + CO + M$	1.180e16	0.000	84720.00
110	$HCNO + H \rightleftharpoons H + HNCO$	2.100e15	–0.690	2850.00
111	$HCNO + H \rightleftharpoons OH + HCN$	2.700e11	0.180	2120.00
112	$HCNO + H \rightleftharpoons NH_2 + CO$	1.700e14	–0.750	2890.00
113	$HOCN + H \rightleftharpoons H + HNCO$	2.000e07	2.000	2000.00
114	$NH_3 + H \rightleftharpoons NH_2 + H_2$	5.400e05	2.400	9915.00
115	$NH_3 + OH \rightleftharpoons NH_2 + H_2O$	5.000e07	1.600	955.00
116	$NH_3 + O \rightleftharpoons NH_2 + OH$	9.400e06	1.940	6460.00

[*] Duplicate reactions.
[a] Third-body efficiencies and pressure-dependent reaction rates are given in Table B.2.

Table B.2: Third-body efficiencies and pressure-dependent reaction rates for the starting reaction mechanism, Table B.1.

No.	H_2	H_2O	CO	CO_2	O_2	Ar	He	A_o	n_o	E_o	α	T^{***}	T^*	T^{**}
		3rd Body Efficiencies, γ_α						Low Pressure Limit			Pressure-Dependent Rates[a]			
5	0.0	0.0		0.0		0.63	0.63							
9	2.0	6.3	1.75	3.6		0.38	0.38							
10	2.0	12.0	1.75	3.6		0.7	0.7							
11	2.4	15.4	1.75	3.6		0.83	0.83							
12	0.75	11.89	1.09	2.18	0.85	0.40	0.46	6.328e19	−1.40	0.0	0.5	1e-30	1e30	
14	2.0	6.0	1.75	3.6		0.7	0.7	2.010e17	−0.584	−2293	0.7346	94	1756	5182
27	2.0	12	1.75	3.6		0.7	0.7	1.173e24	−2.79	4191				
36	2.0	0.0	1.75	3.6										
46	2.0	6.0	1.5	2.0				6.200e14	0.0	56100				
48	2.0	6.0	1.5	2.0										
66	2.0	6.0	1.5	2.0										
72	2.0	6.0	1.5	2.0										
87	2.0	6.0	1.5	2.0										
90	2.0	6.0	1.5	2.0										
97	2.0	6.0	1.5	2.0										
109	2.0	6.0	1.5	2.0										

[a] Troe form with center broadening factor given by $F_c = (1-\alpha)\exp\left(-T/T^{***}\right) + \alpha\exp\left(-T/T^*\right) + \exp\left(-T/T^{**}\right)$.

B.2   Reduced Mechanism Details

The net reaction rates for the 6-step mechanism (Reactions I–VI), presented in Section 4.6.2, are given as summations of the net rates of the starting mechanism, numbered as in Table B.1. The net rate of production of species α in Equation (3.38) is calculated by

$$R_\alpha = W_\alpha \sum_{r=\text{I}}^{\text{VI}} \nu_{\alpha,r} w_r. \tag{B.1}$$

The global rates, w_r, are calculated using;

$$
\begin{aligned}
w_{\text{I}} = {}& + w_1 - w_{11} + w_{12} + w_{13} - w_{17} - w_{18} - w_{19} - w_{20} - w_{21} + w_{30} \\
& + w_{38} + w_{40} - w_{42} - w_{49} + w_{55} + w_{56} + w_{67} + w_{76} + w_{80} + w_{86} \\
& - w_{98} - w_{99} - w_{101},
\end{aligned} \tag{B.2}
$$

$$
\begin{aligned}
w_{\text{II}} = {}& + w_2 - w_4 + w_{10} + w_{11} + w_{12} + w_{13} - w_{15} - w_{18} - w_{19} - w_{20} \\
& - w_{21} + w_{24} - w_{28} - w_{29} - w_{30} - w_{31} + w_{33} + w_{38} - w_{46} - w_{47} \\
& + w_{49} + w_{50} + w_{51} + w_{56} + w_{57} + w_{59} + w_{60} + w_{61} + w_{62} + w_{67} \\
& + w_{68} + w_{73} + w_{76} + w_{77} + w_{79} + w_{81} + w_{82} + w_{85} + w_{88} - w_{90} \\
& - w_{95} - w_{96} + w_{98} + w_{99} + w_{103} + w_{104} - w_{108} - w_{110} - w_{112} \\
& - w_{113} + w_{116},
\end{aligned} \tag{B.3}
$$

$$
\begin{aligned}
w_{\text{III}} = {}& + w_3 + w_4 + w_9 + w_{14} + w_{15} + w_{18} + w_{19} + w_{20} + w_{21} - w_{22} \\
& - w_{24} + w_{35} + w_{40} + w_{41} + w_{43} + w_{51} + w_{53} + w_{54} + w_{55} + w_{56} \\
& + w_{57} + w_{62} + w_{64} + w_{71} + w_{75} - w_{79} + w_{82} + w_{84} + w_{85} + w_{86} \\
& + w_{103} + w_{107} + w_{115},
\end{aligned} \tag{B.4}
$$

$$w_{\mathrm{IV}} = + w_5 + w_6 + w_7 + w_8 + w_9 + w_{10} + w_{11} + w_{12} + w_{14} - w_{28}$$

$$- w_{29} - w_{30} - w_{31} - w_{34} - w_{36} - w_{37} + w_{40} + w_{41} + w_{43} - w_{46}$$

$$- w_{47} + w_{49} + w_{50} + w_{51} + w_{56} + w_{57} + w_{61} + w_{62} + w_{63} + w_{64}$$

$$- w_{65} - w_{66} + w_{73} + w_{74} + w_{75} + w_{76} + w_{77} + 2w_{82} + w_{83} + w_{84}$$

$$+ 2w_{85} + w_{86} + w_{88} - w_{90} + w_{92} + w_{103} - w_{108}, \tag{B.5}$$

$$w_{\mathrm{V}} = + w_{27} + w_{28} + w_{29} + w_{30} + w_{31} + w_{34} + w_{86} + w_{89} + w_{102} + w_{108}, \tag{B.6}$$

$$w_{\mathrm{VI}} = + w_{39} - w_{43} + w_{57} + w_{59} + w_{60} - w_{69} + w_{85} + w_{88} + w_{89} - w_{99}. \tag{B.7}$$

The 7-step reduced mechanism uses the following additional net reaction rate;

$$w_{\mathrm{VII}} = + w_{47} + w_{48} - w_{49} - w_{50}. \tag{B.8}$$

and modified net reaction rates for Equations (B.3) and (B.5);

$$w_{\mathrm{II}} = + w_2 - w_4 + w_{10} + w_{11} + w_{12} + w_{13} - w_{15} - w_{18} - w_{19} - w_{20}$$

$$- w_{21} + w_{24} - w_{28} - w_{29} - w_{30} - w_{31} + w_{33} + w_{38} - w_{46} + w_{48}$$

$$+ w_{51} + w_{56} + w_{57} + w_{59} + w_{60} + w_{61} + w_{62} + w_{67}$$

$$+ w_{68} + w_{73} + w_{76} + w_{77} + w_{79} + w_{81} + w_{82} + w_{85} + w_{88} - w_{90}$$

$$- w_{95} - w_{96} + w_{98} + w_{99} + w_{103} + w_{104} - w_{108} - w_{110} - w_{112}$$

$$- w_{113} + w_{116},$$

$$w_{\text{IV}} = + w_5 + w_6 + w_7 + w_8 + w_9 + w_{10} + w_{11} + w_{12} + w_{14} - w_{28}$$

$$- w_{29} - w_{30} - w_{31} - w_{34} - w_{36} - w_{37} + w_{40} + w_{41} + w_{43} - w_{46}$$

$$+ w_{48} + w_{51} + w_{56} + w_{57} + w_{61} + w_{62} + w_{63} + w_{64}$$

$$- w_{65} - w_{66} + w_{73} + w_{74} + w_{75} + w_{76} + w_{77} + 2w_{82} + w_{83} + w_{84}$$

$$+ 2w_{85} + w_{86} + w_{88} - w_{90} + w_{92} + w_{103} - w_{108}.$$

Appendix C

Burner Details

In this appendix the inlet conditions for the off-gas burner simulations presented in Chapter 6 are detailed and the emissions indices are given. The conditions used for modelling are based on the experiments of Grimwood [50].

C.1   Burner Inlet Conditions

The experiments consisted of parametric studies of ϕ, v_{bulk} and $H_2 : CO$ for the ATP tests, given in Tables C.1, C.2 and C.3. For the HT tests ϕ and v_{bulk} were studied given in Table C.4.

Condition			20	21	22	23	24	25	26	27	28	A	B	C
ϕ			0.337	0.357	0.389	0.405	0.422	0.463	0.505	0.537	0.570	0.610	0.650	0.689
H_2 : CO			1.482	1.466	1.481	1.488	1.471	1.484	1.483	1.482	1.478	1.440	1.408	1.380
Fuel to Air Velocity			0.988	0.994	0.996	0.998	1.000	1.000	1.003	0.999	1.000	1.000	1.000	1.000
Flow Mass Fractions	Fuel	H_2	0.024	0.026	0.029	0.031	0.032	0.037	0.042	0.047	0.051	0.056	0.062	0.068
		CO	0.228	0.245	0.272	0.287	0.304	0.347	0.394	0.437	0.482	0.544	0.612	0.685
		N_2	0.748	0.729	0.698	0.682	0.664	0.615	0.564	0.517	0.467	0.399	0.326	0.247
	Air	O_2	0.233	0.233	0.233	0.233	0.233	0.233	0.233	0.233	0.233	0.233	0.233	0.233
		N_2	0.767	0.767	0.767	0.767	0.767	0.767	0.767	0.767	0.767	0.767	0.767	0.767
Exit Velocity at 298 K [m/s]		Fuel	0.831	0.836	0.839	0.840	0.842	0.842	0.844	0.841	0.842	0.842	0.842	0.842
		Air	0.842	0.842	0.842	0.842	0.842	0.842	0.842	0.842	0.842	0.842	0.842	0.842
		Bulk	0.839	0.840	0.841	0.841	0.842	0.842	0.842	0.841	0.842	0.842	0.842	0.842
Slot Fuel Mass Flow [kg/s]			7.15e-04	7.09e-04	6.89e-04	6.80e-04	6.72e-04	6.43e-04	6.18e-04	5.94e-04	5.73e-04	5.51e-04	5.29e-04	5.06e-04
Slot Air Mass Flow [kg/s]			9.80e-04	9.80e-04	9.80e-04	9.80e-04	9.80e-04	9.80e-04	9.80e-04	9.80e-04	9.80e-04	9.80e-04	9.80e-04	9.80e-04

Table C.2: Off-gas burner input conditions for v_{bulk} sweep. Adapted from Grimwood [50].

Condition			1	2	3	4	4^*	5	5^*
ϕ			0.502	0.503	0.505	0.344	0.341	0.345	0.339
H_2 : CO			1.482	1.477	1.481	1.489	1.496	1.476	1.474
Fuel to Air Velocity			1.001	0.999	1.002	1.001	0.997	1.001	0.998
Flow Mass Fractions	Fuel	H_2	0.042	0.042	0.042	0.025	0.024	0.025	0.024
		CO	0.392	0.395	0.395	0.229	0.227	0.231	0.227
		N_2	0.566	0.563	0.563	0.747	0.749	0.745	0.749
	Air	O_2	0.233	0.233	0.233	0.233	0.233	0.233	0.233
		N_2	0.767	0.767	0.767	0.767	0.767	0.767	0.767
Exit Velocity at 298 K [m/s]		Fuel	0.421	0.631	0.843	0.632	0.285	0.842	0.693
		Air	0.421	0.631	0.842	0.631	0.286	0.842	0.694
		Bulk	0.421	0.631	0.842	0.631	0.286	0.842	0.694
Slot Fuel Mass Flow [kg/s]			3.09e-04	4.62e-04	6.18e-04	5.42e-04	2.45e-04	7.23e-04	5.98e-04
Slot Oxidizer Mass Flow [kg/s]			4.90e-04	7.35e-04	9.80e-04	7.35e-04	3.33e-04	9.80e-04	8.08e-04

Table C.2: Off-gas burner input conditions for ν_{bulk} sweep. Adapted from Grimwood [50] (continued).

Condition			11b	11c	11d	11e	26[*]	26a	26b	26c
ϕ			0.37	0.369	0.373	0.369	0.442	0.442	0.442	0.440
H_2 : CO			1.47	1.467	1.474	1.465	1.478	1.466	1.478	1.467
Fuel to Air Velocity			1.000	1.001	1.045	1.064	1.000	0.997	1.000	0.988
Flow Mass Fractions	Fuel	H_2	0.027	0.027	0.026	0.025	0.035	0.035	0.035	0.035
		CO	0.254	0.253	0.242	0.234	0.325	0.328	0.325	0.329
		N_2	0.719	0.72	0.732	0.741	0.64	0.637	0.64	0.636
	Air	O_2	0.233	0.233	0.233	0.233	0.233	0.233	0.233	0.233
		N_2	0.767	0.767	0.767	0.767	0.767	0.767	0.767	0.767
Exit Velocity at 298 K [m/s]		Fuel	1.116	0.885	0.66	0.421	0.842	0.629	0.421	0.212
		Air	1.115	0.884	0.631	0.396	0.842	0.631	0.421	0.215
		Bulk	1.116	0.884	0.638	0.402	0.842	0.631	0.421	0.214
Slot Fuel Mass Flow [kg/s]			9.37e-04	7.43e-04	5.60e-04	3.61e-04	6.58e-04	4.92e-04	3.29e-04	1.65e-04
Slot Oxidizer Mass Flow [kg/s]			1.30e-03	1.03e-03	7.35e-04	4.61e-04	9.80e-04	7.35e-04	4.90e-04	2.50e-04

Table C.3: Off-gas burner input conditions for H_2 : CO ratio sweep. Adapted from Grimwood [50].

Condition			7	13	14	15
ϕ			0.422	0.421	0.421	0.423
H_2 : CO			1.471	1.944	1.280	0.972
Fuel to Air Velocity			1.000	0.999	0.999	1.001
Flow Mass Fractions	Fuel	H_2	0.032	0.037	0.030	0.025
		CO	0.304	0.267	0.322	0.356
		N_2	0.663	0.696	0.649	0.619
	Air	O_2	0.233	0.233	0.233	0.233
		N_2	0.767	0.767	0.767	0.767
Exit Velocity at 298 K [m/s]		Fuel	0.842	0.841	0.841	0.843
		Air	0.842	0.842	0.842	0.842
		Bulk	0.842	0.841	0.841	0.842
Slot Fuel Mass Flow [kg/s]			6.72e-04	6.41e-04	6.87e-04	7.21e-04
Slot Oxidizer Mass Flow [kg/s]			9.80e-04	9.80e-04	9.80e-04	9.80e-04

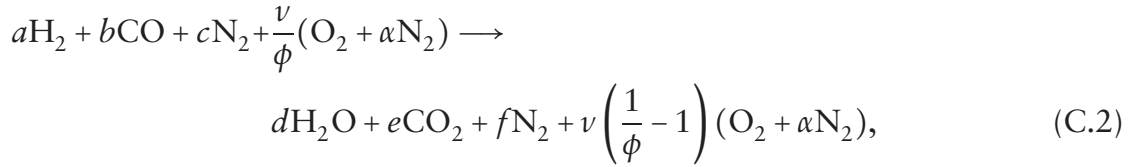**Table C.4:** High temperature off-gas burner input conditions. Adapted from Grimwood [50].

Condition		DATUM	1	2	3	4	8	9	10	11
ϕ		0.069	0.014	0.041	0.104	0.139	0.069	0.069	0.07	0.07
$H_2 : CO$		0.68	0.652	0.676	0.692	0.69	0.676	0.672	0.684	0.714
Fuel to air velocity at 298 K		0.182	0.039	0.114	0.263	0.337	0.183	0.183	0.184	0.183
Inlet Temperature [K]	Fuel	1111	1209	1166	1082	1042	1124	1130	1124	1122
	Oxidizer	1126	1125	1125	1116	1117	1121	1120	1121	1131
Flow Mass Fractions	CO_2	0.635	0.634	0.637	0.638	0.637	0.636	0.635	0.636	0.638
(Fuel)	H_2	0.008	0.007	0.007	0.008	0.008	0.007	0.007	0.008	0.008
	H_2O	0.204	0.203	0.203	0.202	0.202	0.203	0.204	0.203	0.202
	CO	0.154	0.155	0.153	0.153	0.153	0.154	0.154	0.154	0.152
(Oxidizer)	N_2	0.626	0.698	0.661	0.589	0.555	0.626	0.626	0.626	0.626
	O_2	0.127	0.142	0.135	0.12	0.113	0.128	0.128	0.128	0.127
	Ar	0.011	0.012	0.011	0.01	0.009	0.011	0.011	0.011	0.011
	CO_2	0.163	0.067	0.117	0.213	0.259	0.163	0.163	0.164	0.164
	H_2O	0.072	0.081	0.076	0.068	0.064	0.072	0.072	0.072	0.073
Exit Velocity at 298 K [m/s]	Fuel	0.826	0.166	0.498	1.242	1.659	1.243	0.935	0.417	0.208
	Oxidizer	4.54	4.23	4.383	4.731	4.926	6.801	5.102	2.267	1.135
	Bulk	3.611	3.214	3.412	3.859	4.109	5.412	4.06	1.805	0.903
Exit Velocity at 1123 K [m/s]	Bulk	13.03	11.97	12.69	14.32	14.83	19.53	14.65	6.51	3.26
Slot Fuel Mass Flow [kg/s]		7.65e-04	1.55e-04	4.63e-04	1.15e-03	1.54e-03	1.15e-03	8.68e-04	3.86e-04	1.93e-04
Slot Oxidizer Mass Flow [kg/s]		4.96e-03	4.41e-03	4.68e-03	5.30e-03	5.65e-03	7.44e-03	5.58e-03	2.48e-03	1.24e-03

C.2   Emission Indices

For comparison with industrial burners, it is usual to give the NO_x levels in the form of emissions indices, EI_{NO}, where the mass of NO_x formed is calculated per unit of fuel input [113]. The emissions index for NO, EI_{NO} [g/kJ], is calculated using

$$EI_{NO} = \frac{\text{Mass of NO}}{\text{Fuel energy input}} = \frac{\dot{m}_{NO}}{\dot{m}_{\text{fuel}} \Delta h_{\text{fuel}}}. \tag{C.1}$$

To convert the concentrations predicted using the model to EI_{NO}, a general equation for $H_2/CO/N_2$ combustion is used;

$$a H_2 + b CO + c N_2 + \frac{\nu}{\phi}(O_2 + \alpha N_2) \longrightarrow$$
$$d H_2O + e CO_2 + f N_2 + \nu\left(\frac{1}{\phi} - 1\right)(O_2 + \alpha N_2), \tag{C.2}$$

where the coefficients for each reactant or product are given by

$$a = d = X_{H_2},$$
$$b = e = X_{CO},$$
$$c = f = X_{N_2}.$$

α is 3.76 for air. The stoichiometric coefficient is calculated using

$$\nu = \frac{1}{2}\left(X_{H_2} + X_{CO}\right). \tag{C.3}$$

The equivalence ratio, ϕ, is known for each inlet condition. Assuming complete combustion, the concentration of products can be calculated. The molar enthalpy of formation

Table C.5: CO and NO emissions for equivalence ratio sweep. Conditions given in Table C.1, taken from Grimwood [50].

Condition	ϕ	X_{NO} [ppm]	EI_{NO} [g/kJ]	X_{CO} [ppm]
20	0.337	4.4	3.73e-06	679.4
21	0.357	5.2	4.11e-06	382.3
22	0.389	6.6	4.61e-06	159.5
23	0.405	7.3	4.88e-06	103.7
24	0.422	8.1	5.09e-06	74.0
25	0.463	10.1	5.53e-06	44.0
26	0.505	12.7	6.05e-06	46.5
27	0.537	15.2	6.56e-06	62.8
28	0.570	18.5	7.18e-06	98.2
A	0.610	23.9	8.24e-06	183.8
B	0.650	31.6	9.68e-06	356.6
C	0.689	43.3	1.18e-05	695.7

of the fuel stream is calculated using

$$\Delta \bar{h}_{\text{fuel}} = X_{H_2} \Delta \bar{h}_{H_2} + X_{CO} \Delta \bar{h}_{CO}. \tag{C.4}$$

The molar enthalpies of formation of H_2 and CO are calculated using

$$\Delta \bar{h}_{H_2} = \bar{h}_{H_2O} - \bar{h}_{H_2}, \tag{C.5}$$

$$\Delta \bar{h}_{CO_2} = \bar{h}_{CO_2} - \bar{h}_{CO}. \tag{C.6}$$

For each ATP inlet condition the emission index is calculated based on the predictions made using the 6-step mechanism. These are given in Tables C.5, C.6 and C.7 for the ϕ, ν_{bulk} and H_2 : CO ratio sweeps, respectively.

Table C.6: CO and NO emissions for bulk velocity sweep. Conditions given in Table C.2, taken from Grimwood [50].

Condition	ϕ	v_{bulk}	X_{NO} [ppm]	EI_{NO} [g/kJ]	X_{CO} [ppm]
4*	0.34	0.286	3.0	2.54e-06	205.6
4	0.34	0.631	4.2	3.51e-06	367.3
5*	0.34	0.694	4.1	3.49e-06	501.8
5	0.34	0.842	4.4	3.65e-06	582.0
11e	0.37	0.402	4.2	3.26e-06	93.0
11d	0.37	0.638	5.0	3.80e-06	173.3
11c	0.37	0.884	5.4	4.11e-06	309.8
11b	0.37	1.116	5.4	4.04e-06	518.9
26c	0.44	0.214	4.2	2.44e-06	0.5
26b	0.44	0.421	6.6	3.84e-06	16.2
26a	0.44	0.631	7.9	4.62e-06	32.4
26*	0.44	0.842	8.7	5.06e-06	50.5
1	0.50	0.421	8.6	4.15e-06	10.4
2	0.50	0.631	10.6	5.08e-06	25.3
3	0.50	0.842	11.8	5.65e-06	45.6

Table C.7: CO and NO emissions for H_2 : CO ratio sweep. Conditions given in Table C.3, taken from Grimwood [50].

Condition	H_2:CO	X_{NO} [ppm]	EI_{NO} [g/kJ]	X_{CO} [ppm]
15	0.97	8.4	5.31e-06	96.0
14	1.28	7.8	4.94e-06	83.0
7	1.47	7.7	4.83e-06	72.2
13	1.94	7.2	4.51e-06	64.6

List of References

[1] A. F. Al-Shaikhly, G. E. Andrews, and C. O. Aniagolu. Jet shear layer turbulent diffusion flames for ultralow NO_x emissions. *Journal of Engineering for Gas Turbines and Power*, 114:55–62, 1992.

[2] J. Baker, M. E. Calvert, and D. W. Murphy. Structure and dynamics of laminar jet micro-slot diffusion flames. *Journal of Heat Transfer*, 124:783–790, 2002.

[3] R. S. Barlow. Personal communication, October 2007.

[4] R. S. Barlow, G. J. Fiechtner, C. D. Carter, and J.-Y. Chen. Experiments of the scalar structure of turbulent $CO/H_2/N_2$ jet flames. *Combustion and Flame*, 120: 549–569, 2000.

[5] R. S. Barlow, A. N. Karpetis, J. H. Frank, and J. Chen. Scalar profiles and NO formation in laminar opposed-flow partially premixed methane/air flames. *Combustion and Flame*, 127:2102–2118, 2001.

[6] R. S. Barlow, G. J. Fiechtner, C. D. Carter, and M. Flury. Sandia/ETH-Zurich $CO/H_2/N_2$ flame data – release 1.1. Technical report, Sandia National Laboratories, 2002. URL http://www.ca.sandia.gov/TNF.

[7] R. W. Bilger. A note on Favre averaging in variable density flows. *Combustion Science and Technology*, 11:215–217, 1975.

[8] R. W. Bilger. The structure of diffusion flames. *Combustion Science and Technology*, 13:155–170, 1976.

[9] R. W. Bilger. The structure of turbulent nonpremixed flames. *Proceedings of the Combustion Institute*, 22:475–488, 1988.

[10] R. W. Bilger, S. H. Stårner, and R. J. Kee. On reduced mechanisms for methane-air combustion in nonpremixed flames. *Combustion and Flame*, 80:135–149, 1990.

[11] R. B. Bird, W. E. Stewart, and E. N. Lightfoot. *Transport Phenomena*. John Wiley & Sons, New York, 1960.

[12] C. T. Bowman. Control of combustion-generated nitrogen oxide emissions: Tech-

nology driven by regulation. *Proceedings of the Combustion Institute*, 24:859–878, 1992.

[13] C. T. Bowman, R. K. Hanson, D. F. Davidson, W. C. Gardiner, Jr., V. V. Lissianski, G. P. Smith, D. M. Golden, M. Frenklach, and M. Goldenberg. `GRI-Mech 2.11`, 1995. URL `http://www.me.berkeley.edu/gri_mech/`.

[14] R. S. Cant and E. Mastorakos. *An Introduction to Turbulent Reacting Flows*. Imperial College Press, London, 2008.

[15] R. R. Cao and S. B. Pope. The influence of chemical mechanisms on PDF calculations of nonpremixed piloted jet flames. *Combustion and Flame*, 143:450–470, 2005.

[16] R. R. Cao, H. Wang, and S. B. Pope. The effect of mixing models in PDF calculations of piloted jet flames. *Proceedings of the Combustion Institute*, 31:1543–1550, 2007.

[17] K. H. Casleton, R. W. Breault, and G. A. Richards. System issues and tradeoffs associated with syngas production and combustion. *Combustion Science and Technology*, 180:1013–1052, 2008.

[18] M. Chaos and F. L. Dryer. Syngas combustion kinetics and applications. *Combustion Science and Technology*, 180:1053–1096, 2008.

[19] J.-Y. Chen. A general procedure for constructing reduced reaction mechanisms with given independent relations. Technical Report SAND87-8782, Sandia National Laboratories, 1987.

[20] J.-Y. Chen. A general procedure for constructing reduced reaction mechanisms with given independent relations. *Combustion Science and Technology*, 57:89–94, 1988.

[21] J.-Y. Chen. Development of reduced mechanisms for numerical modelling of turbulent combustion. Workshop on "Numerical Aspects of Reduction in Chemical Kinetics" CERMICS-ENPC Cite Descartes - Champs sur Marne, France, September 1997.

[22] J.-Y. Chen. TNF workshop 6-step reduced mechanism, 2002. URL `http://public.ca.sandia.gov/TNF/chemistry.html`.

[23] J.-Y. Chen, R. W. Dibble, and R. W. Bilger. PDF modeling of turbulent non-premixed $CO/H_2/N_2$ jet flames with reduced mechanisms. *Proceedings of the Combustion Institute*, 23:775–780, 1990.

[24] J.-Y. Chen, Y. Liu, and B. Rogg. CO-H_2-N_2/air diffusion flames: Thermal radi-

ation and transient effects. In N. Peters and B. Rogg, editors, *Reduced Kinetic Mechanisms for Applications in Combustion Systems*, chapter 12, pages 196–223. Springer-Verlag, 1993.

[25] P. J. Coelho. Detailed numerical simulation of radiative transfer in a nonluminous turbulent jet diffusion flame. *Combustion and Flame*, 136:481–492, 2004.

[26] P. J. Coelho and N. Peters. Numerical simulation of a mild combustion burner. *Combustion and Flame*, 124:503–518, 2001.

[27] W. T. Collins, S. Hochgreb, N. Swaminathan, and J.-Y. Chen. Simulation of NO_x formation in dilute $H_2/CO/N_2$–air diffusion flames using full and reduced kinetics. In *Proceedings of the European Combustion Meeting*. The Combustion Institute, 2007.

[28] S. M. Correa and A. Gulati. Measurements and modeling of a bluff body stabilized flame. *Combustion and Flame*, 89:195–213, 1992.

[29] S. M. Correa and S. B. Pope. Comparison of a Monte Carlo PDF/finite-volume mean flow model with bluff-body Raman data. *Proceedings of the Combustion Institute*, 24:279–285, 1992.

[30] S. G. Davis, A. V. Joshi, H. Wang, and F. Egolfopoulos. An optimized kinetic model of H_2/CO combustion. *Proceedings of the Combustion Institute*, 30:1283–1292, 2005.

[31] A. M. Dean and J. W. Bozzelli. Combustion chemistry of nitrogen. In W. C. Gardiner, editor, *Gas-Phase Combustion Chemistry*, chapter 2, pages 125–341. Springer, 2000.

[32] G. Dixon-Lewis. Flame structure and flame reaction kinetics. II. Transport phenomena in multicomponent systems. *Proceedings of the Royal Society A*, 307:111–135, 1968.

[33] Y. Dong, A. T. Holley, M. G. Andac, F. N. Egolfopoulos, S. G. Davis, P. Middha, and H. Wang. Extinction of premixed H_2/air flames: Chemical kinetics and molecular diffusion effects. *Combustion and Flame*, 142:374–387, 2005.

[34] M. C. Drake and R. J. Blint. Thermal NO_x in stretched laminar opposed-flow diffusion flames with $CO/H_2/N_2$ fuel. *Combustion and Flame*, 76:151–167, 1989.

[35] M. C. Drake and R. J. Blint. Relative importance of nitric oxide formation mechanisms in laminar opposed-flow diffusion flames. *Combustion and Flame*, 85:185–203, 1991.

[36] F. L. Dryer and M. Chaos. Ignition of syngas/air and hydrogen/air mixtures at low

temperatures and high pressures: Experimental data interpretation and kinetic modeling implications. *Combustion and Flame*, 152:293–299, 2008.

[37] E. Effelsberg and N. Peters. Scalar dissipation rates in turbulent jets and jet diffusion flames. *Proceedings of the Combustion Institute*, 22:693–700, 1988.

[38] I. S. Ertesvåg and B. F. Magnussen. The eddy dissipation turbulence energy cascade model. *Combustion Science and Technology*, 159:213–235, 2000.

[39] Fluent Inc. *Fluent 6.3 User's Guide*, 2006.

[40] A. Frassoldati, S. Frigerio, E. Colombo, F. Inzoli, and T. Faravelli. Determination of NO_x emissions from strong swirling confined flames with an integrated CFD-based procedure. *Chemical Engineering Science*, 60:2851–2869, 2005.

[41] E. Giacomazzi, F. R. Picchia, and N. Arcidiacono. Unsteady and axisymmetric simulation of the SANDIA syngas/air turbulent non-premixed flame "A". In *Third European Combustion Meeting*. The Combustion Institute, 2007.

[42] D. E. Giles, S. Som, and S. K. Aggarwal. NO_x emission characteristics of counterflow syngas diffusion flames with airstream dilution. *Fuel*, 85:1729–1742, 2006.

[43] P. Glarborg, R. J. Kee, J. F. Grear, and J. A. Miller. PSR: A Fortran program for modeling well-stirred reactors. Technical Report SAND86-8209, Sandia National Laboratories, 1986.

[44] I. Glassman. *Combustion*. Academic Press, New York, 1977.

[45] G. Goldin. Personal communication, May 2007.

[46] I. R. Gran. *Mathematical Modeling and Numerical Simulation of Chemical Kinetics in Turbulent Combustion*. PhD thesis, University of Trondheim, 1994.

[47] I. R. Gran and B. F. Magnussen. A numerical study of a bluff-body stabilized diffusion flame. Part 1. Influence of turbulence modeling and boundary conditions. *Combustion Science and Technology*, 119:147–190, 1996.

[48] I. R. Gran and B. F. Magnussen. A numerical study of a bluff-body stabilized diffusion flame. Part 2. Influence of combustion modeling and finite-rate chemistry. *Combustion Science and Technology*, 119:191–217, 1996.

[49] I. R. Gran, I. S. Ertesvåg, and B. F. Magnussen. Influence of turbulence modeling on predictions of turbulent combustion. *AIAA Journal*, 35(1):106–110, January 1997.

[50] C. Grimwood. *Development of a Low Pressure Drop, Low Emission Burner*. PhD thesis, University of Cambridge, Cambridge, April 2007.

[51] R. K. Hanson and S. Salimian. Survey of rate constants in the N/H/O system.

In W. C. Gardiner, editor, *Combustion Chemistry*, chapter 6, pages 361–421. Springer-Verlag, 1984.

[52] M. İlbas, I. Yilmaz, and Y. Kaplan. Investigation of hydrogen and hydrogen-hydrocarbon composite fuel combustion and NO_x emission characteristics in a model combustor. *International Journal of Hydrogen Energy*, 2004.

[53] L.-Y. Jiang and I. Campbell. A critical evaluation of NO_x modeling in a model combustor. *Journal of Engineering for Gas Turbines and Power*, 127(3):483–491, July 2005.

[54] C. Jiménez, B. Cuenot, T. Poinsot, and D. Haworth. Numerical simulation and modeling for lean stratified propane-air flames. *Combustion and Flame*, 128: 1–21, 2002.

[55] W. P. Jones and J. H. Whitelaw. Calculation methods for reacting turbulent flows: A review. *Combustion and Flame*, 48:1–26, 1982.

[56] A. V. Joshi and H. Wang. Master equation modeling of wide range temperature and pressure dependence of $CO + OH \rightarrow$ Products. *International Journal of Chemical Kinetics*, 38:57–73, 2006.

[57] R. J. Kee, F. M. Rupley, and J. A. Miller. CHEMKIN II: A Fortran chemical kinetics package for the analysis of gas phase chemical kinetics. Technical Report SAND89-8009, Sandia National Laboratories, 1991.

[58] R. J. Kee, F. M. Rupley, J. A. Miller, M. E. Coltrin, J. F. Grcar, E. Meeks, H. K. Moffat, A. E. Lutz, G. Dixon-Lewis, M. D. Smooke, J. Warnatz, G. H. Evans, R. S. Larson, R. E. Mitchell, L. R. Petzold, W. C. Reynolds, M. Caracotsios, W. E. Stewart, P. Glarborg, C. Wang, C. L. McLellan, O. Adigun, W. G. Houf, C. P. Chou, S. F. Miller, P. Ho, P. Young, and D. J. Young. *CHEMKIN Release 4.0*. Reaction Design, San Diego, CA, 2004.

[59] R. J. Kee, H. Zhu, A. M. Sukushini, and G. S. Jackson. Solid oxide fuel cells: Operating principles, current challenges, and the role of syngas. *Combustion Science and Technology*, 180:1207–1244, 2008.

[60] G. Kim, S. Kang, Y. Kim, R. W. Bilger, and M. J. Cleary. Conditional moment closure and transient flamelet modelling for detailed structure and NO_x formation characteristics of turbulent nonpremixed jet and recirculating flames. *Combustion Theory and Modelling*, 11(4):527–552, August 2007.

[61] I. S. Kim and E. Mastorakos. Simulations of turbulent lifted jet flames with two-

dimensional conditional moment closure. *Proceedings of the Combustion Institute*, 30:911–918, 2005.

[62] S.-K. Kim, S.-M. Kang, and Y.-M. Kim. Flamelet modeling for combustion processes and NO_x formation in the turbulent nonpremixed $CO/H_2/N_2$ jet flames. *Combustion Science and Technology*, 168:47–83, 2001.

[63] A. Y. Klimenko and R. W. Bilger. Conditional moment closure for turbulent combustion. *Progress in Energy and Combustion Science*, 25:595–687, 1999.

[64] K. K. Kuo. *Principles of Combustion*. John Wiley & Sons, Inc., New York, 1st edition, 1986.

[65] B. E. Launder, G. J. Reece, and W. Rodi. Progress in the development of a Reynolds-stress turbulence closure. *Journal of Fluid Mechanics*, 68:537–566, 1975.

[66] C. K. Law. *Combustion Physics*. Cambridge University Press, 2006.

[67] C. E. Lee, C. B. Oh, and J. H. Kim. Numerical and experimental investigations of the NO_x emission characteristics of CH_4-air coflow jet flames. *Fuel*, 83:2323–2334, 2004.

[68] C.-W. Lee and E. Mastorakos. Numerical simulations of HCCI engines with high levels of residual gas. *International Journal of Engine Research*, 8(1):63–78, 2007.

[69] T. Lieuwen, V. McDonell, D. Santavicca, and T. Sattelmayer. Burner development and operability issues associated with steady flowing syngas fired combustors. *Combustion Science and Technology*, 180:1169–1192, 2008.

[70] B. J. D. Liu and S. B. Pope. The performance of *in situ* adaptive tabulation in computations of turbulent flames. *Combustion Theory and Modelling*, 9(4):549–568, November 2005.

[71] A. E. Lutz, R. J. Kee, J. F. Grcar, and F. M. Rupley. OPPDIF: A FORTRAN program for computing opposed-flow diffusion flames. Technical Report SAND96-8243, Sandia National Laboratories, 1997.

[72] U. Maas and J. Warnatz. Ignition processes in carbon-monoxide-hydrogen-oxygen mixtures. *Proceedings of the Combustion Institute*, 22:1695–1704, 1988.

[73] B. F. Magnussen. On the structure of turbulence and a generalized eddy dissipation concept for chemical reaction in turbulent flow. *19th AIAA Aerospace Science Meeting*, pages 1–6, 1981.

[74] B. F. Magnussen and B. H. Hjertager. On mathematical modeling of turbulent

combustion with special emphasis on soot formation and combustion. *Proceedings of the Combustion Institute*, 16:719–729, 1976.

[75] B. F. Magnussen, B. H. Hjertager, J. G. Olsen, and D. Bhaduri. Effects of turbulent structure and local concentrations on soot formation and combustion in C_2H_2 diffusion flames. *Proceedings of the Combustion Institute*, 17:1383–1393, 1978.

[76] A. R. Masri, R. Cao, S. B. Pope, and G. M. Goldin. PDF calculations of turbulent lifted flames of H_2/N_2 fuel issuing into a vitiated co-flow. *Combustion Theory and Modelling*, 8:1–22, 2004.

[77] S. Mathur, P. K. Tondon, and S. C. Saxena. Thermal conductivity of binary, ternary and quaternary mixtures of rare gases. *Molecular Physics*, 12(6):569–579, 1967.

[78] F. Mauss and N. Peters. Reduced kinetic mechanisms for premixed methane-air flames. In N. Peters and B. Rogg, editors, *Reduced Kinetic Mechanisms for Applications in Combustion Systems*, volume m 15 of *Lecture Notes in Physics*, chapter 5, pages 58–75. Springer-Verlag, Heidelberg, 1993.

[79] B. Merci, E. Dick, and C. D. Langhe. Application of an improved ϵ-equation to a piloted jet diffusion flame. *Combustion and Flame*, 131:465–468, 2002.

[80] P. Middha, B. Yang, and H. Wang. A first-principle calculation of the binary diffusion coefficients pertinent to kinetic modeling of hydrogen/oxygen/helium flames. *Proceedings of the Combustion Institute*, 29:1361–1369, 2002.

[81] J. A. Miller and C. T. Bowman. Mechanism and modeling of nitrogen chemistry in combustion. *Progress in Energy and Combustion Science*, 15:287–338, 1989.

[82] B. R. Munson, D. F. Young, and T. H. Okiishi. *Fundamentals of Fluid Mechanics*. John Wiley & Sons, New York, third edition, 1998.

[83] T. Myhrvold, I. S. Ertesvåg, I. R. Gran, R. Cabra, and J.-Y. Chen. A numerical investigation of a lifted H_2/N_2 turbulent jet flame in a vitiated coflow. *Combustion Science and Technology*, 178:1001–1030, 2006.

[84] S. Naha and S. K. Aggarwal. Fuel effects of NO_x emissions in partially premixed flames. *Combustion and Flame*, 139:90–105, 2004.

[85] J. Natarajan, T. Lieuwen, and J. Seitzman. Laminar flame speeds of H_2/CO mixtures: Effect of CO_2 dilution, preheat temperature, and pressure. *Combustion and Flame*, 151:104–119, 2007.

[86] C. Nicoli, P. Haldenwang, and B. Denet. Combustion of gaseous coflow jets. *Combustion Science and Technology*, 175:1143–1163, 2003.

[87] S. V. Patankar. *Numerical Heat Transfer and Fluid Flow*. Taylor & Francis, New York, 1980.

[88] S. V. Patankar and D. B. Spalding. A calculation procedure for heat, mass and momentum transfer in three-dimensional parabolic flows. *International Journal of Heat and Mass Transfer*, 15:1787–1806, 1972.

[89] N. Peters. *Turbulent Combustion*. Cambridge University Press, 2000.

[90] N. Peters. Laminar diffusion flamelet models in non-premixed turbulent combustion. *Progress in Energy and Combustion Science*, 10:319–339, 1984.

[91] N. Peters and R. J. Kee. The computation of stretched laminar methane-air diffusion flames using a reduced four-step mechanism. *Combustion and Flame*, 68: 17–29, 1987.

[92] E. L. Petersen, D. M. Kalitan, A. B. Barrett, S. C. Reehal, J. D. Mertens, D. J. Beerer, R. L. Hack, and V. G. McDonell. New syngas/air ignition data at lower temperature and elevated pressure and comparison to current kinetics models. *Combustion and Flame*, 149:244–247, 2007.

[93] H. Pitsch. Unsteady flamelet modeling of differential diffusion in turbulent jet diffusion flames. *Combustion and Flame*, 123:358–374, 2000.

[94] H. Pitsch. Improved pollutant predictions in large-eddy simulations of turbulent non-premixed combustion by considering scalar dissipation rate fluctuations. *Proceedings of the Combustion Institute*, 29:1971–1978, 2002.

[95] H. Pitsch and N. Peters. A consistent flamelet formulation for non-premixed combustion considering differential diffusion effects. *Combustion and Flame*, 114:26–40, 1998.

[96] T. Poinsot and D. Veynante. *Theoretical and Numerical Combustion*. R. T. Edwards, Inc., Philadelphia, PA, 2nd edition, 2005.

[97] S. B. Pope. *Turbulent Flows*. Cambridge University Press, Cambridge, 2000.

[98] S. B. Pope. An explanation of the turbulent round-jet/plane-jet anomaly. *AIAA Journal*, 16(3):278–281, March 1978.

[99] S. B. Pope. PDF methods for turbulent reactive flows. *Progress in Energy and Combustion Science*, 11:119–192, 1985.

[100] S. B. Pope. Computationally efficient implementation of combustion chemistry using *in situ* adaptive tabulation. *Combustion Theory and Modelling*, 1:41–63, 1997.

[101] R. V. Ravikrishna and N. M. Laurendeau. Laser-induced fluorescence measure-

ments and modeling of nitric oxide in counterflow partially premixed flames. *Combustion and Flame*, 122:474–482, 2000.

[102] B. Rogg and F. A. Williams. Structures of wet CO flames with full and reduced kinetic mechanisms. *Proceedings of the Combustion Institute*, 22:1441–1451, 1989.

[103] U. Schumann. Realizability of Reynolds-stress turbulence models. *Physics of Fluids*, 20(5), May 1977.

[104] T.-H. Shih, J. Zhu, and J. L. Lumley. A new reynolds stress algebraic equation model. Technical Report 106644, NASA, 1994.

[105] T.-H. Shih, W. W. Liou, A. Shabbir, Z. Yang, and J. Zhu. A new k-ϵ eddy viscosity model for high Reynolds number turbulent flows. *Computers & Fluids*, 24(3): 227–238, 1995.

[106] R. Sivaramakrishnan, A. Comandini, R. S. Tranter, K. Brezinsky, S. G. Davis, and H. Wang. Combustion of CO/H_2 mixtures at elevated pressures. *Proceedings of the Combustion Institute*, 31:429–437, 2007.

[107] E. J. Smith, J. Mi, G. J. Nathan, and B. B. Dally. Preliminary examination of a "round jet initial condition anomaly" for the k-ϵ turbulence model. In *15th Australasian Fluid Mechanics Conference*, Sydney, Australia, December 2004. The University of Sydney.

[108] G. P. Smith, D. M. Golden, M. Frenklach, N. W. Moriarty, B. Eiteneer, M. Goldenberg, C. T. Bowman, R. K. Hanson, S. Song, W. C. Gardiner, Jr., V. V. Lissianski, and Z. Qin. GRI-Mech 3.0, 1999. URL http://www.me.berkeley.edu/gri_mech/.

[109] H. Steiner and W. K. Bushe. Large eddy simulation of a turbulent reacting jet with conditional source-term estimation. *Physics of Fluids*, 13(3):754–769, March 2001.

[110] C.-J. Sung and C. K. Law. Fundamental combustion properties of H_2/CO mixtures: Ignition and flame propagation at elevated pressures. *Combustion Science and Technology*, 180:1097–1116, 2008.

[111] C. J. Sung, C. K. Law, and J.-Y. Chen. Augmented reduced mechanisms for NO emission in methane oxidation. *Combustion and Flame*, 125:906–919, 2001.

[112] S. R. Turns. Understanding NO_x formation in nonpremixed flames: Experiments and modeling. *Progress in Energy and Combustion Science*, 21:361–385, 1995.

[113] S. R. Turns. *An Introduction to Combustion: Concepts and Applications*. McGraw-Hill, New York, 1996.

[114] J. Warnatz, U. Maas, and R. W. Dibble. *Combustion*. Springer-Verlag, Berlin, 3rd edition, 2001.

[115] C. K. Westbrook and F. L. Dryer. Chemical kinetic modeling of hydrocarbon combustion. *Progress in Energy and Combustion Science*, 10:1–57, 1984.

[116] A. A. Westenberg. Kinetics of NO and CO in lean, premixed hydrocarbon-air flames. *Combustion Science and Technology*, 4:59–64, 1971.

[117] K. J. Whitty, H. R. Zhang, and E. G. Eddings. Emissions from syngas combustion. *Combustion Science and Technology*, 180:1117–1136, 2008.

[118] C. R. Wilke. A viscosity equation for gas mixtures. *Journal of Chemical Physics*, 18(4):517–519, April 1950.

[119] R. A. Yetter, F. L. Dryer, and H. Rabitz. A comprehensive reaction mechanism for carbon monoxide/hydrogen/oxygen kinetics. *Combustion Science and Technology*, 79:97–128, 1991.

[120] J. Zhu and T.-H. Shih. Computation of confined coflow jets with three turbulence models. *International Journal for Numerical Methods in Fluids*, 19:939–956, 1994.

Author Index

Colophon

This thesis is typeset in Sabon using LaTeX 2_ε with the hepthesis[a] class with modifications made by the author. All graphs are generated using Gnuplot[b] and figures are prepared in Xfig[c].

[a]http://www.ctan.org/tex-archive/help/Catalogue/entries/hepthesis.html
[b]http://www.gnuplot.info/
[c]http://www.xfig.org/